Volume 51, Number 3, 2025.

Mobility & Vehicle Mechanics

International Journal for Vehicle Mechanics, Engines and Transportation Systems

ISSN 1450 - 5304

UDC 621 + 629(05)=802.0

UNIVERSITY OF KRAGUJEVAC, FACULTY OF ENGINEERING September, 2025.

M V M **M**obility **V**ehicle **M**echanics

*Editor: Prof. dr **Jovanka Lukić***

MVM *Editorial Board*
University of Kragujevac
Faculty of Engineering
Sestre Janjić 6, 34000 Kragujevac, Serbia
Tel.: +381/34/335990; Fax: + 381/34/333192

For Publisher: Prof. dr Slobodan Savić, dean, University of Kragujevac, Faculty of Engineering

Publishing of this Journal is financially supported from:
Ministry of Education, Science and Technological Development, Republic Serbia

Mobility & **V**ehicle **M**echanics

Motorna **V**ozila i **M**otori

Volume 51
Number 3
2025.

Mobility & **V**ehicle **M**echanics

Motorna **V**ozila i **M**otori

Volume 51
Number 3
2025.

MOBILITY & VEHICLE MECHANICS

https://doi.org/10.24874/mvm.2025.51.03.01
UDC: 621.436:621.892:620.3

NANOSCALE TRIBOLOGICAL INFLUENCE OF NBA ADDED IN ENGINE OIL FOR FRICTION AND WEAR BEHAVIOUR IN DIESEL ENGINE CYLINDER LINER SURFACE RUBBED UNDER 1ST AND 2ND PISTON RINGS

E. Hakan Kaleli [1], Selman Demirtaş[2], Veli Uysal[3]*

Received in August 2024 *Accepted in October 2024*

RESEARCH ARTICLE

ABSTRACT: Nanoparticles are particles between 1 and 100 nanometres (nm) in size with a surrounding interfacial layer. One of these famous nanoparticles is nanoboric acid (nBA) additive added in engine oil that drastically lowered friction and wear. This scientifical and experimental work presents the developped new suspended nanoboric acid (nBA) additive added in engine oil and lowered friction and wear in Diesel engine specimens tested in reciprocating tribometer.

Proving nBA particles that were in colloidal form in engine oil with Turbiscan Tower Stability Analyzer, the engine oil is tested between piston ring and cylinder liner system in order to investigate their effect on friction and wear under boundary lubricated conditions. Simulation and measurement of friction and wear were conducted using a reciprocating tribometer. Surface analysis was performed using 3D digital optical microscope, Field Emission Scanning Electron Microscope (FESEM)/X-Ray, X-ray photoelectron spectroscopy (XPS) and Atomic Force Microscopy (AFM) from macro to nanoscale. Boron (B) from BA is well detected and mixed with other elements of additives protecting the surface under boundary lubrication conditions. It has found that the friction coefficient is reduced with nBA suspended engine oil and protected the surface mostly on cylinder liner mixing with other additives.

KEY WORDS: *Nano boric acid, Diesel Engine, Friction, Wear, Surface Analysis*

[1]*E. Hakan Kaleli, Yıldız Technical University, Faculty of Mechanical Engineering, Mechanical Engineering Department 34349 İstanbul / Turkey, kaleli@yildiz.edu.tr, https://orcid.org/0000-0001-7586-918X, (*Corresponding author)*
[2] *Selman Demirtaş , Yıldız Technical University, Faculty of Mechanical Engineering, Mechanical Engineering Department 34349 İstanbul / Turkey, demirtasselman@gmail.com, https://orcid.org/-*
[3] *Veli Uysal, Yıldız Technical University, Faculty of Mechanical Engineering, Mechanical Engineering Department 34349 İstanbul / Turkey, v_uysal@hotmail.com, https://orcid.org/-*

TRIBOLOŠKI UTICAJ DODATOG NBA U MOTORNO ULJE NA PONAŠANJE TRENJA I HABANJA NA POVRŠINI KOŠULJICE CILINDRA DIZEL MOTORA KOJA SE TRLJA ISPOD PRVOG I DRUGOG KLIPNOG PRSTENA U NANO RAZMERI

REZIME: Nanočestice su čestice veličine između 1 i 100 nanometara (nm) sa okolnim međupovršinskim slojem. Jedna od ovih poznatih nanočestica je aditiv nanoborne kiseline (nBA) dodat u motorno ulje koji drastično smanjuje trenje i habanje. Ovaj naučni i eksperimentalni rad predstavlja razvijeni novi suspendovani aditiv nanoborne kiseline (nBA) dodat u motorno ulje i smanjuje trenje i habanje u uzorcima dizel motora testiranim u klipnom tribometru.

Ispitivan je uticaj čestica nBA, u koloidnom obliku u motornom ulju, na trenje i habanje u uslovima graničnog podmazivanja između sistema klipnog prstena i obloge cilindra, pomoću Turbiscan Tower Stability Analyzer-a. Simulacija i merenje trenja i habanja sprovedeni su pomoću klipnog tribometra. Analiza površine je izvršena pomoću 3D digitalnog optičkog mikroskopa, skenirajućeg elektronskog mikroskopa sa emisijom polja (FESEM)/X-zraka, rendgenske fotoelektronske spektroskopije (XPS) i atomske sile mikroskopije (AFM) od makro do nano razmere. Bor (B) iz BA je dobro detektovan i pomešan sa drugim elementima aditiva koji štite površinu pod uslovima graničnog podmazivanja. Utvrđeno je da se koeficijent trenja smanjuje sa suspendovanim nBA u motornom uljeu i štiti površinu uglavnom na košuljici cilindra mešanjem sa drugim aditivima.

KLJUČNE REČI: *Nano borna kiselina, dizel motor, trenje, habanje, analiza površine*

NANOSCALE TRIBOLOGICAL INFLUENCE OF NBA ADDED IN ENGINE OIL FOR FRICTION AND WEAR BEHAVIOUR IN DIESEL ENGINE CYLINDER LINER SURFACE RUBBED UNDER 1ST AND 2ND PISTON RINGS

E. Hakan Kaleli, Selman Demirtaş, Veli Uysal

INTRODUCTION

More effective or enhanced lubrication is needed to meet the increasingly more stringent operational conditions of future engine systems and drivetrain components. The fuel economy, durability, and environmental soundness of all engines are closely related to the effectiveness of the lubricants being used. Poor or inefficient lubrication may result in high friction and wear losses, which can in turn adversely affect the fuel economy and durability of these engines [1, 2, 3, 4].

Automotive engine oils demand superior tribological properties to prolong the lifespan of mechanical components. Engine lubrication is critical for saving energy, reducing material losses, and enhancing both engine durability and fuel economy in automobiles. From an energy-saving standpoint, the transportation sector alone consumes almost 30% of the total energy produced today. Unfortunately, approximately one-third of this energy is still wasted due to friction and wear in various moving components of cars, trucks, and buses, which are integral to our mobility (Lubrication mechanism analysis). Only 21% of the fuel used in automobiles is actually used for driving; the remaining 79% is lost to energy loss. Frictional losses cause an estimated 11.5% reduction in the engine's overall power output. Consequently, enhancing the tribological properties of mechanical components and reducing engine friction losses becomes imperative in order to raise brake engine power and enhance engine durability. Therefore, the exploration of engine oil additives has become a central area of research and development in the automotive industry, with the goal of enhancing the efficiency, durability, and reliability of engine oils, as well as fuel economy [5, 6].

One of the major losses occurring in the engine of an automobile is due to friction between its moving parts. This loss is significant and approximately 15% of the total loss of energy and has a direct impact on the efficiency and durability of the engine. Different mechanical systems require a variety of functional lubricants to reduce the friction and wear of contacting surfaces as well as a significant reduction in the total energy consumed by mechanical systems [7].

Engine oil is an efficient means of minimizing friction, dissipation of frictional heat, and controlling wear by creating a lubricating layer with low-shear strength between rubbing surfaces that rub against each other in mechanical systems [8, 9].

Recent research papers have reported that the addition of nanoparticles to lubricant is effective for the reduction of wear and friction in mechanical systems. Because of the remarkable tribological properties of nanoparticles, nanotechnology is regarded as the most revolutionary technology of this century [10].

Numerous nanoparticles have recently been investigated for use as oil additives. Nano-powders of some metals and their compounds exert an especially effective influence on the characteristics of lubricants. The use of nanoparticles that include Cu, CuO, Fe, Ni, TiO2 and other metallic nanoparticle additives in lubricating oils provides good friction reduction and anti-wear behavior. Among these additives, nano boric acid (BA) nanoparticles have

received significant attention because they deposit on the friction surface, improve the tribological properties of the base oil and display good anti-friction and wear reduction characteristics [11].

Boric acid owes its self-lubricating nature to a lamellar crystalline structure. When present between sliding surfaces, it can shear easily to provide low friction. Boron Carbide (B4C) on which the boric acid film was formed is a well-developed and adapted hard coating for sliding engine and bearing applications mainly because of its excellent resistance to wear and scuffing [1, 12].

Research specifically aimed at the use of boric acid in engineering systems has also been undertaken in 2000s [13, 12]. These studies have indicated that boric acid's unique layered inter-crystalline structure (see figure 1) makes it a very promising solid lubricant material because of its relatively high load carrying capacity and low steady-state friction coefficient [14].

Boric acid has been identified as a potential solid lubricant due to its lamellar molecular structure. Further, it is abundant and environmentally benign, with no known health risks to humans. These experiments clearly indicate that powder delivery of boric acid is a viable technique for providing in situ lubrication for concentrated metal contacts [15]. In the early 1990s, the lubricity of boric acid, an overlooked but extremely available and environmentally benign lamellar solid, was demonstrated by Erdemir, et al. [12, 16, 17].

1 EXPERIMENTAL DETAILS

In this study, the tribological performance of nano boric acid suspended in 5W-40 fully synthetic commercial engine oil was characterized by turbidimetry method and investigated under pin (piston ring)-on-plate (cylinder liner) line contact set-up using a custom-made reciprocating tribological test rig.

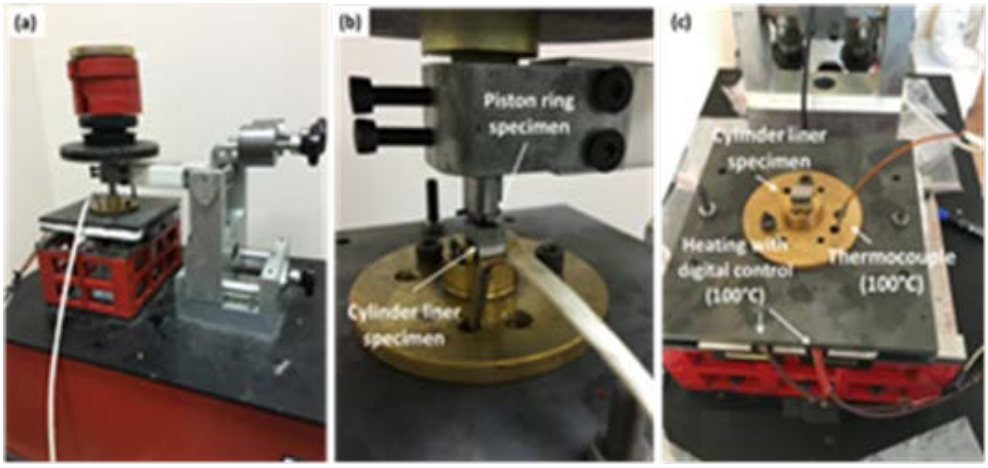

Figure 1 Reciprocating tribotest rig General view of the test rig, (b) Specimens mounted in the test rig, (c) Heating control and temperature measurements.

Table 1 Experimental parameters in tribometer

Load (N)	60.5
Frequency (Hz)	2
Stroke (mm)	8
Oil Temperature °C	99
Test Duration (min)	21

The work consists of tribometer experiments. Friction tests were conducted through a reciprocating tribotest machine (see Fig. 1). The parameters of tribological test are summarized in Table 1. Tests were conducted with a one drop of suspended 5W-40 oil and 5W-40+BA oil on the wear track of cylinder liner.

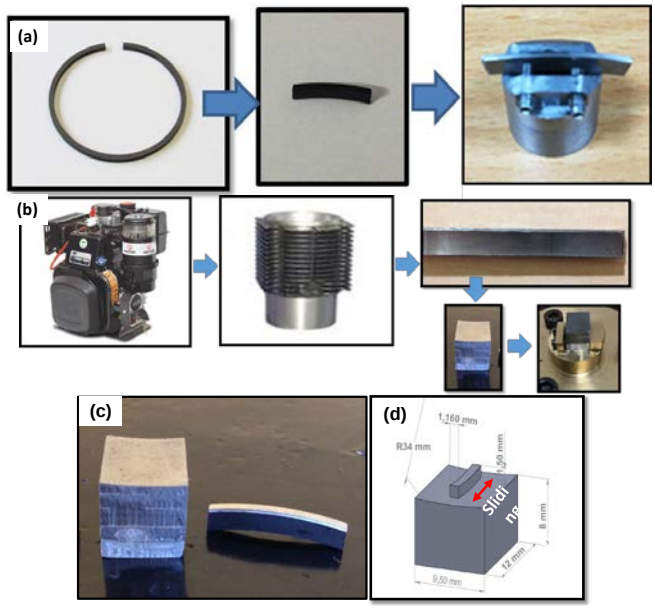

Figure 2 Preparation of piston ring and cylinder specimens (a) Piston ring, (b) liner cut from a new Antor Diesel engine,(c) and (d) specimens with contact position and sliding direction

Figure 2 shows the preparation of piston ring and cylinder specimens; (a) and (b) are piston ring and liner cut precisely from a new Anadolu Motor Antor 6 LD 400 Diesel engine for Tribometer tests. (c) and (d) present the ready specimens with contact position in reciprocating sliding direction. At the end of the tribometer tests, optical, scanning electron microscopy (SEM) with EDS and atomic force microscopy (AFM) have been applied to determine the surface morphology and chemical structure of the piston rings and cylinder liners tested in tribometer. For time/line 1.5 s, for points/line 256 have been used at AFM . Setpoint has been chosen as 20 nN during the AFM tests.

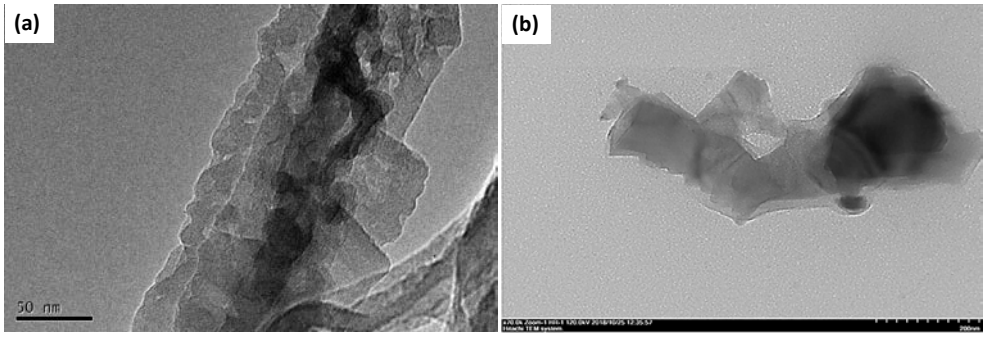

Figure 3 TEM of nBA prepared with Hexane

Figure 3 presents TEM of BA (black patches). The size of BA which varies between 50nm to the 200nm. This size is well acceptable and appropriate passing nanoparticles from engine oil filter. It is added 0.2 % in the oil.

2 DISCUSSIONS AND RESULTS

The primary function of a lubricant is to keep two metal surfaces apart thus reducing friction and preventing wear. Modern machinery with its constantly increasing speed and size has put demands upon lubricants which cannot be met by unfortified petroleum products [18].

Frictional losses in a typical automobile accounts significantly for the reduction of useful power otherwise available for the motion. Almost 15 % of the total energy loss comes from the friction generated between the sliding parts. Lubricants are supplied to reduce such frictional losses. Frictional losses arise mainly at the piston rings, bearings and transmission parts which undergo boundary lubrication or starved lubrication at certain periods during operation. Additives in lubricants come into effect under such conditions. Nano particulate suspended additives in the base oil are of some interest to address the boundary lubrication issues [19].

Hwang et al. (2011) investigated the effect of size and morphology of nanoparticles suspended in lubricating oils on the lubrication performance. The effect of the size of dispersed particles on the lubrication performance was examined by varying the primary size of the spherical-like graphite particles: 55 nm, 450 nm and 5μm. The lubrication performance clearly improved with decreasing size of the particles suspended in the mineral oil. This suggests that nano-sized particles effectively play the role of ball bearings and reduce contact between frictional surfaces [20].

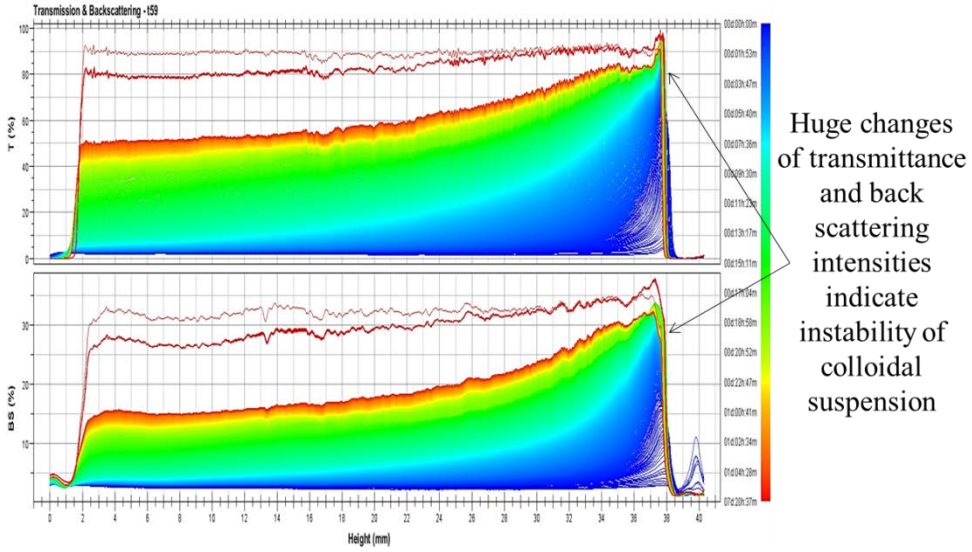

Figure 4 Transmitance and back scattering profiles of non-marketed (non-commercialized) additive showing the (sediment) in 5W-40 engine oil

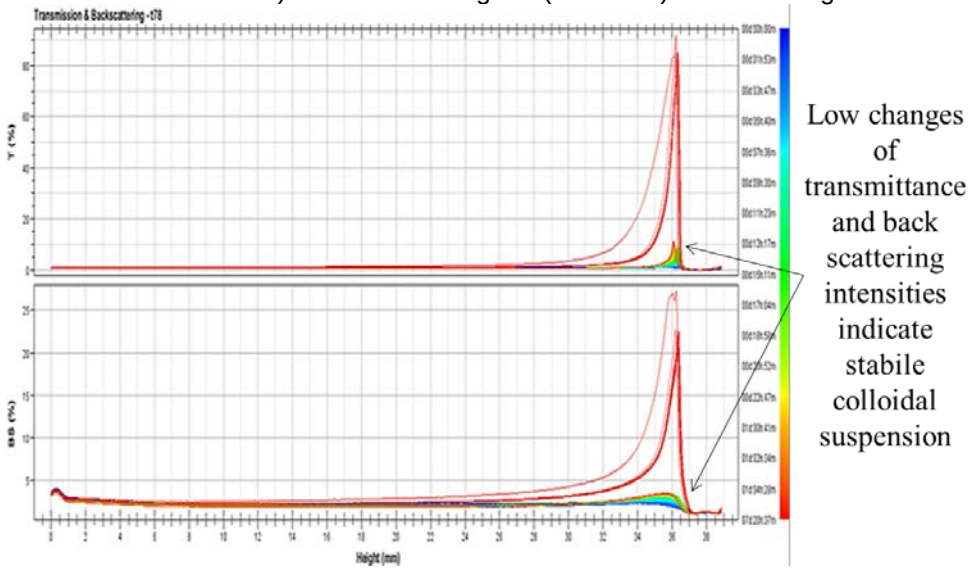

Figure 5 Transmitance and back scattering profiles of BA showing stable suspension in 5W-40 engine oil

Turbidimetry of the samples were observed by turbiscan tower, both the back scattering and transmittance curves changes were analyzed. Backscattering and transmittance signals recorded through 24 h at 20°C. Figure 4 presents transmittance and back scattering profiles of non-marketed (non-commercialized) additive showing the (sediment) in 5W-40 engine oil. Change of transmittance and back scattering intensity is very high in case of non-commercialized additive as seen in Fig.4 that indicate instability of colloidal suspension. The new invention of stable colloidal suspension of nano boric acid (BA) additive added into 5W-40 fully synthetic commercial lubricating oil is well demonstrated in Fig. 5. This

invention is supplied by Tribor ARGE Co. in Teknopark of YILDIZ Technical University in Istanbul-TURKEY. They invented new method of synthesis of nano boric acid.

In this study, real 1st and 2nd piston rings-cylinder liner specimens of Anadolu Motor Antor 6 LD 400 Diesel engine were tested and compared with reciprocating tribometer under boundary lubrication conditions, 100°C, 60.5N using fully formulated engine oil and BA particles suspended in engine oil to investigate their wear and friction behavior. Test were repeated twice.

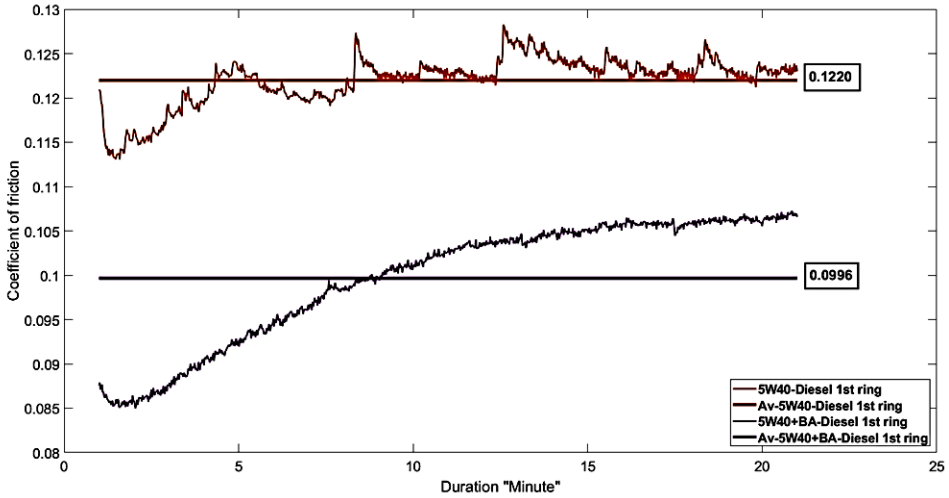

Figure 6 Friction coefficient of 5W-40 engine oil with suspended BA additive via 5W-40 engine oil for the 1st ring test

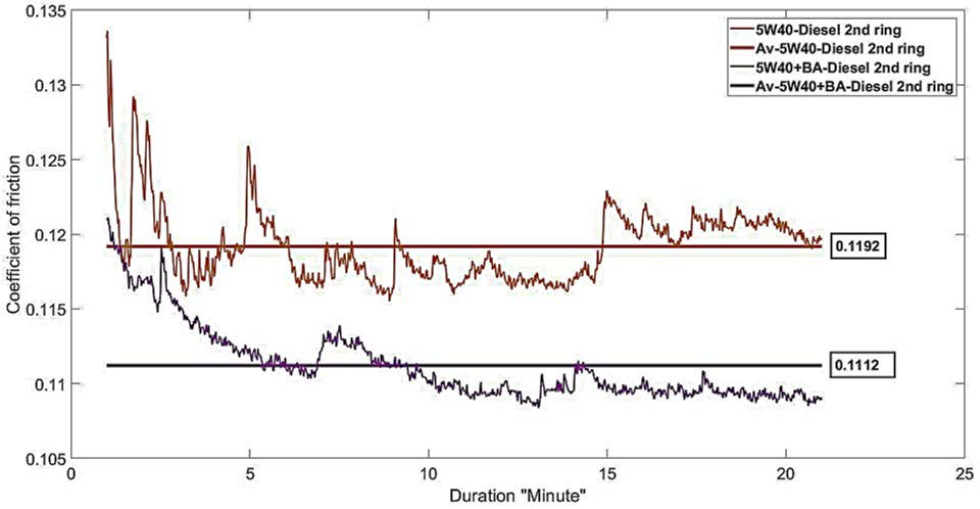

Figure 7 Friction coefficient of 5W-40 engine oil with suspended BA additive via 5W-40 engine oil for the 2nd ring test

According to the results, it has been found that engine oil with BA showed almost similar friction results with the tests of 1st piston ring (0.0996 with BA-0.1220 non BA) (See Fig.6) and obtained less friction, better lubrication and protective performance then oil without

containing BA with the tests of 2nd ring (0.1112 with BA-0.1192 non BA) (See Fig 7) against cylinder liner.

Table 1 Comparison of COF results

Test No	5W40	5W40+BA
1st ring	0.1220	0.0996
2nd ring	0.1192	0.1112

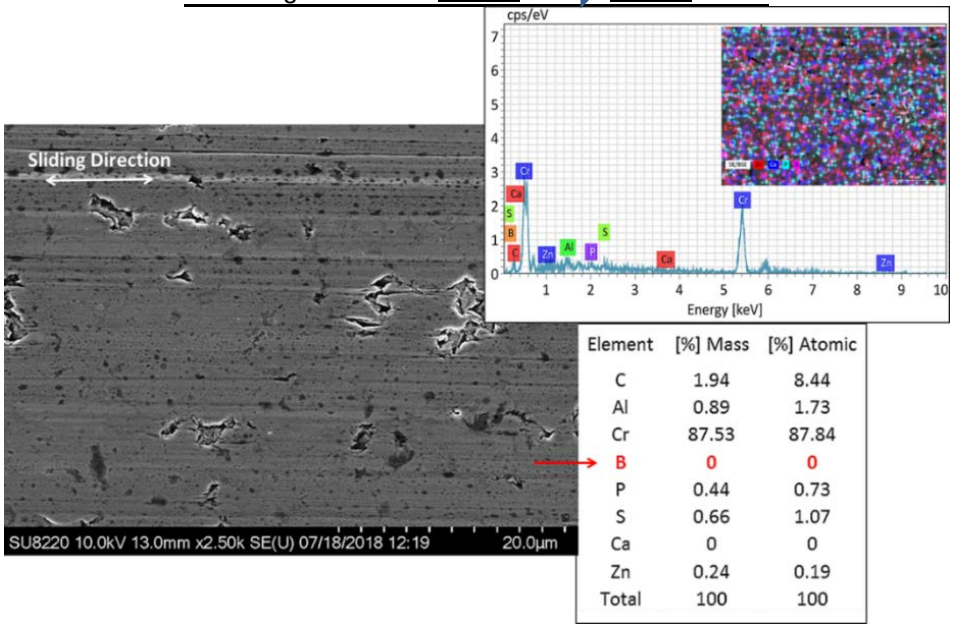

Figure 8 FESEM, X-Ray, mapping and elemental analysis of the rubbed 1st piston ring surface tested with 5W-40 engine oil

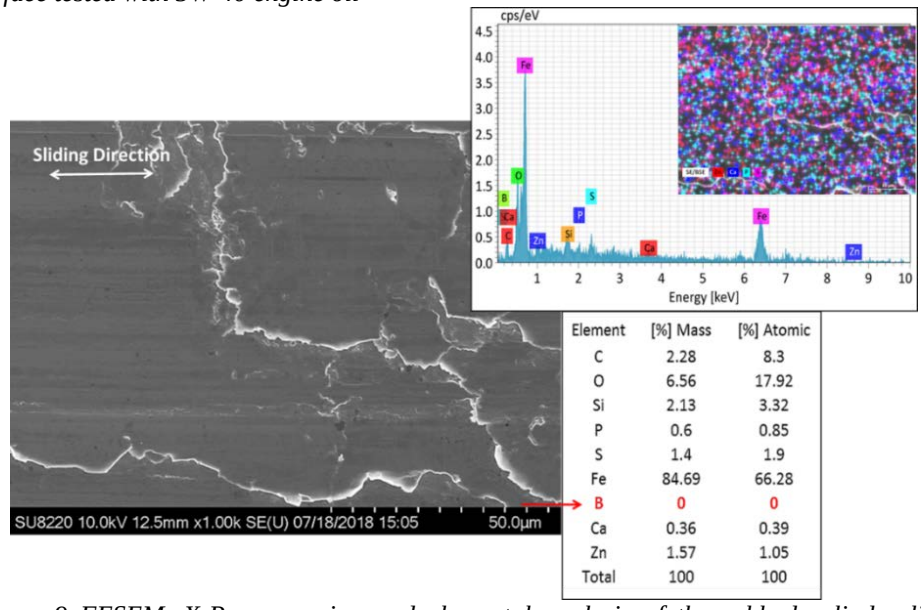

Figure 9 FESEM, X-Ray, mapping and elemental analysis of the rubbed cylinder liner surface under 1st piston ring tested with 5W-40 engine oil.

Figures 8 and 9 are FESEM, X-Ray, mapping and elemental analysis of the rubbed 1st piston ring and cylinder liner tested with 5W-40 engine oil. Any B is detected on the rubbed surface. Elements such as Zn, Ca, P and S were formed layer on the surface, as usual. 5W-40 engine oil does not contain BA.

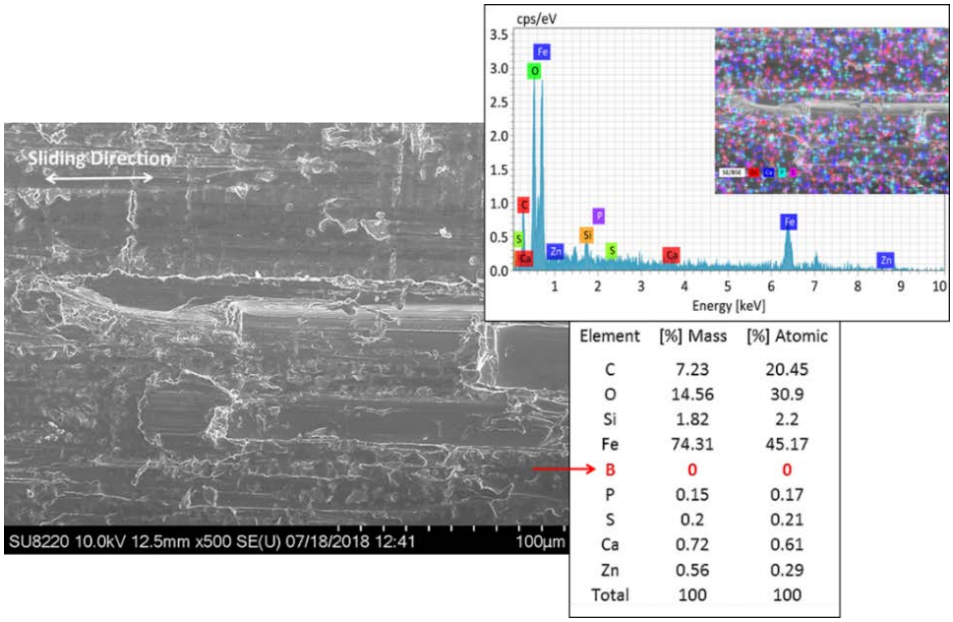

Figure 10 FESEM, X-Ray, mapping and elemental analysis of the rubbed 2nd piston ring surface tested with 5W-40 engine oil.

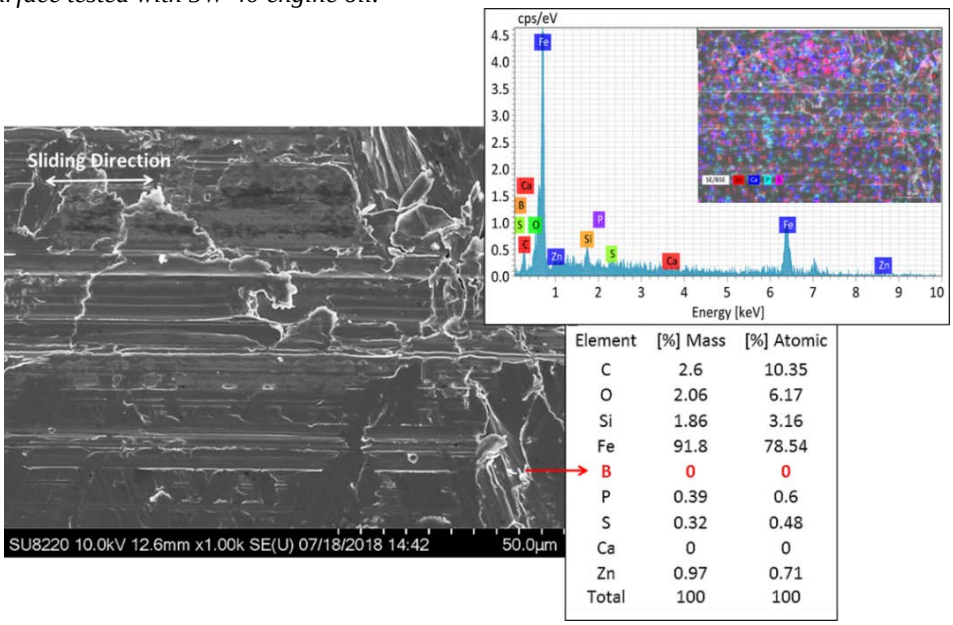

Figure 11 FESEM, X-Ray, mapping and elemental analysis of the rubbed cylinder liner surface under 2nd piston ring tested with 5W-40 engine oil

Figures 10 and 11 are FESEM, X-Ray, mapping and elemental analysis of the rubbed 2nd piston ring and cylinder liner tested with 5W-40 engine oil. Any B is detected on the rubbed surface. Elements such as Zn, Ca, P and S were formed layer on the surface, as usual. 5W-40 engine oil does not contain BA.

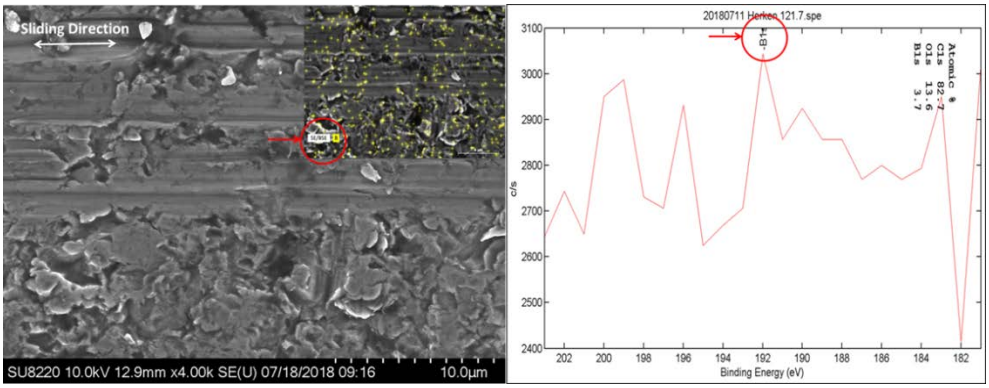

Figure 12 FESEM of the 1st piston ring surface rubbed with 5W-40 engine oil+B where B is detected with X-Ray mapping and XPS

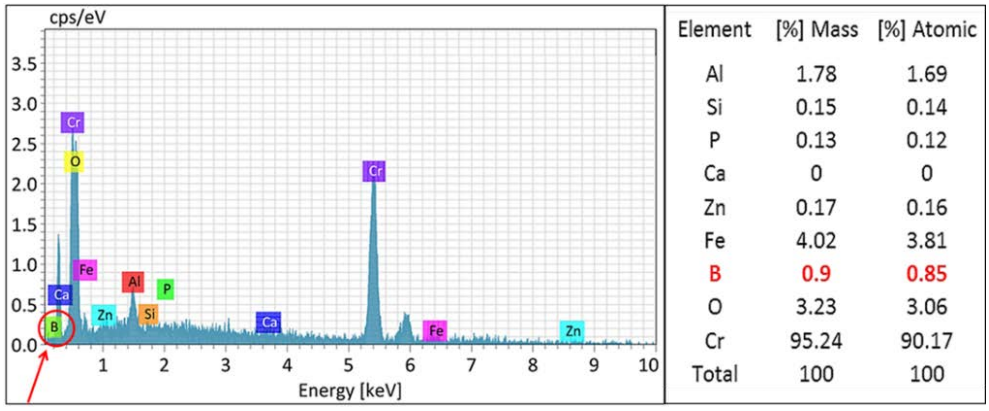

Element	[%] Mass	[%] Atomic
Al	1.78	1.69
Si	0.15	0.14
P	0.13	0.12
Ca	0	0
Zn	0.17	0.16
Fe	4.02	3.81
B	0.9	0.85
O	3.23	3.06
Cr	95.24	90.17
Total	100	100

Figure 13 X-Ray and elemental analysis of the 1st piston ring surface tested with 5W-40 engine oil+B where B is detected from the Fig. 12.

Figures 12 and 13 are FESEM, mapping, XPS, X-Ray and elemental analysis of the 1st piston ring surface rubbed with 5W-40 engine oil+B against cylinder liner where B is well detected showing with red circles. B from NBA (nano boric acid) is mixed with other additives such as Zn, Ca, P and S that formed protective layer on the wear track.

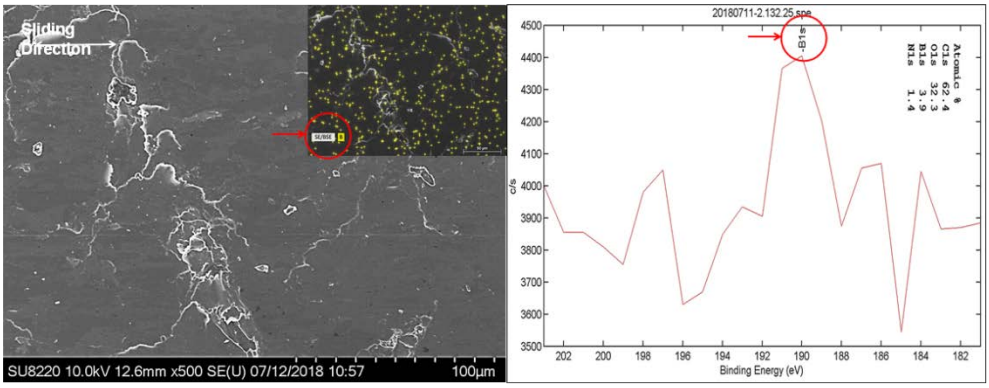

Figure 14 FESEM of the rubbed cylinder liner under 1st piston ring tested with 5W-40 engine oil+B where B is detected with X-Ray mapping and XPS.

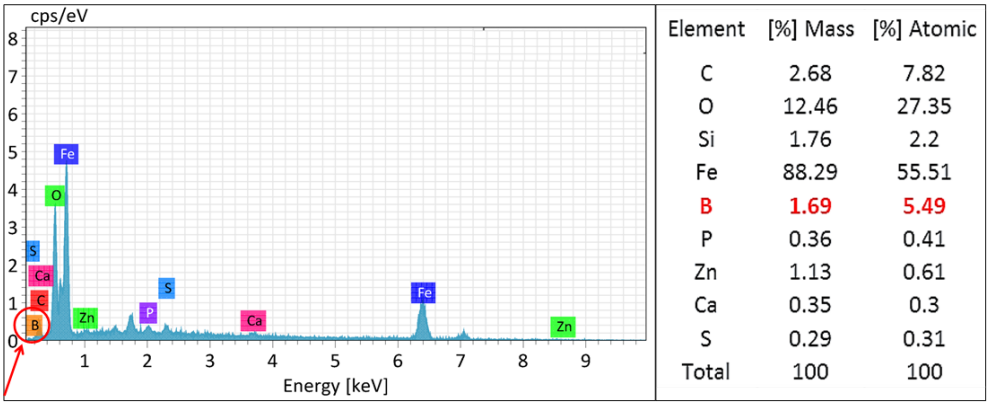

Element	[%] Mass	[%] Atomic
C	2.68	7.82
O	12.46	27.35
Si	1.76	2.2
Fe	88.29	55.51
B	**1.69**	**5.49**
P	0.36	0.41
Zn	1.13	0.61
Ca	0.35	0.3
S	0.29	0.31
Total	100	100

Figure 15 X-Ray and elemental analysis of the rubbed cylinder liner under 1st piston ring tested with 5W-40 engine oil+B where B is detected from the Fig. 14.

Figures 14 and 15 are FESEM, mapping, XPS, X-Ray and elemental analysis of the cylinder liner rubbed under 1st piston ring tested with 5W-40 engine oil+B where B is well detected showing with red circles. B from NBA (nano boric acid) is well mixed with other additives such as Zn, Ca, P and S, so that formed protective layer on the wear track and it is higher as mass and atomic percent on the surface of cylinder liner rather than piston ring.

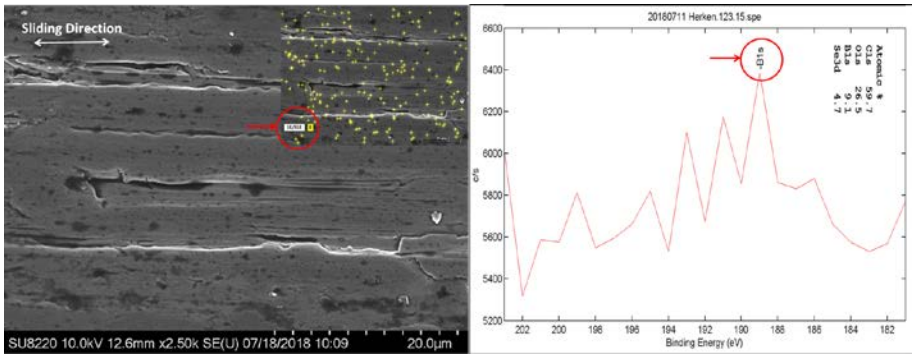

Figure 16 FESEM of the 2nd piston ring surface rubbed with 5W-40 engine oil+B where B is detected with X-Ray mapping and XPS

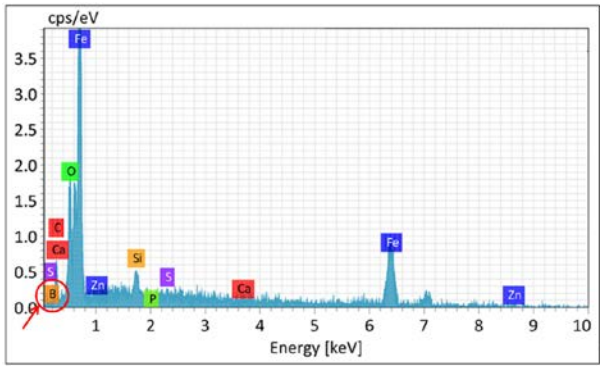

Element	[%] Mass	[%] Atomic
O	6.19	16.68
Si	1.42	2.19
Fe	81.6	63.02
B	1.36	5.41
S	0.19	0.25
P	0	0
Ca	0.05	0.06
Zn	0.21	0.14
C	3.42	12.27
Total	100	100

Figure 17 X-Ray and elemental analysis of the 2nd piston ring surface tested with 5W-40 engine oil+B where B is detected from the Fig. 16

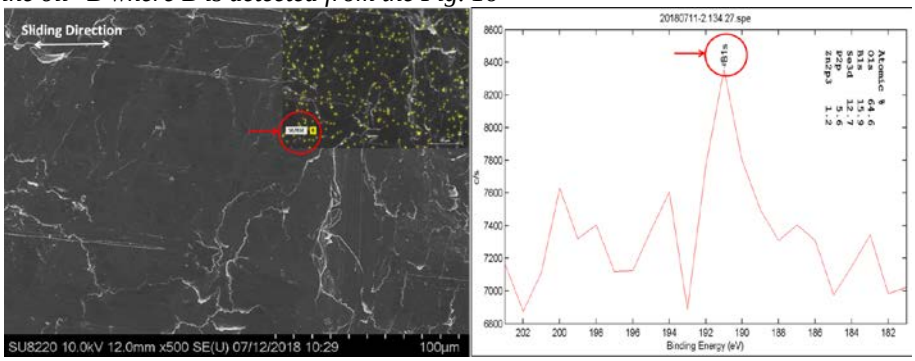

Figure 18 FESEM of the rubbed cylinder liner under 2nd piston ring tested with 5W-40 engine oil+B where B is detected with X-Ray mapping and XPS.

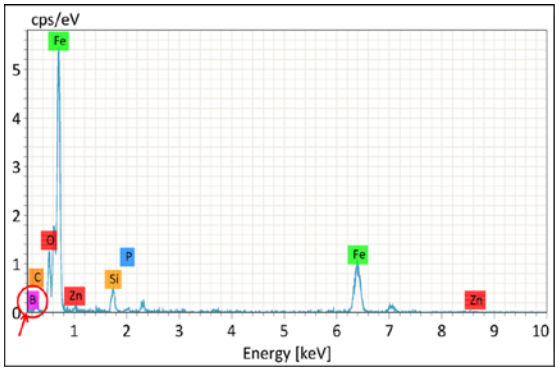

Element	[%] Mass	[%] Atomic
O	4.61	12.81
Si	2.21	3.5
Fe	83.75	66.68
B	1.83	7.52
Zn	1.19	0.81
C	2.23	8.27
P	0.29	0.41
Total	100	100

Figure 19 X-Ray and elemental analysis of the rubbed cylinder liner under 2nd piston ring tested with 5W-40 engine oil+B where B is detected from the Fig. 18

Figures 16 and 17 are FESEM, mapping, XPS, X-Ray and elemental analysis of the 2nd piston ring surface rubbed with 5W-40 engine oil+B against cylinder liner where B is well detected showing with red circles. B from NBA (nano boric acid) is mixed with other additives such as Zn, Ca, P and S that formed protective layer on the wear track. Figures 18 and 19 are FESEM, mapping, XPS, X-Ray and elemental analysis of the cylinder liner rubbed under 2nd piston ring tested with 5W-40 engine oil+B where B is well detected

showing with red circles. B from NBA (nano boric acid) is well mixed with other additives such as Zn, Ca, P and S, so that formed protective layer on the wear track and it is higher as mass and atomic percent on the surface of cylinder liner rather than piston ring.

Table 2 2D-Ra and-3D Sa AFM roughness value.

AFM Roughness measurements	Sa (nm)	Ra (nm)
(b) Tested 1st piston ring with 5W40	101,019 ↑	92.013 ↑
(c) Tested 1st piston ring with nBA	178,37	198.06
(e) Tested liner under 1st piston ring with 5W40	251,39 ↓	260,84 ↓
(f) Tested liner under 1st piston ring with nBA	68,238	52,496
(b) Tested 2nd piston ring with 5W40	228,08 ↓	237.61 ↑
(c) Tested 2nd piston ring with nBA	65,119	51.713
(e) Tested liner under 2nd piston ring with 5W40	602,55 ↓	363,19 ↓
(f) Tested liner under 2nd piston ring with nBA	503,57	342,12

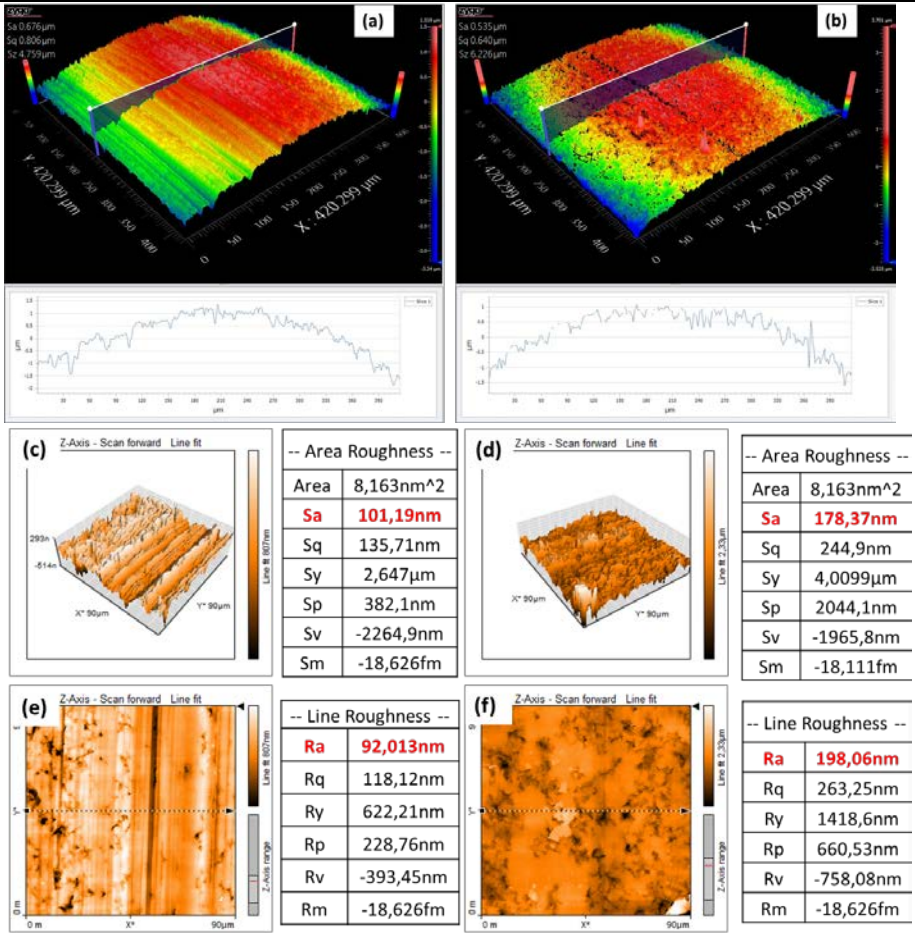

Figure 20 Optical 3D, 3D and Sa of AFM, 2D and Ra of AFM of the 1st piston ring surface tested with 5W-40 engine oil (a, c, e) and 5W-40 engine oil+B (b, d, f)

Figure 20 shows 3D digital optical microscopy, 3D and (surface average) Sa of AFM, 2D and (roughness average) Ra of AFM of the 1st piston ring surface tested with 5W-40 engine oil (a, c, e), and 1st piston ring surface tested with 5W-40 engine oil+B (b, d, f), respectively. Sa (178.37nm) and Ra (198.06nm) of the surface tested with 5W-40 engine oil+B were found higher than the test Sa (101.19nm) and Ra (92.013nm) with 5W-40 engine oil as presented in Table 2.

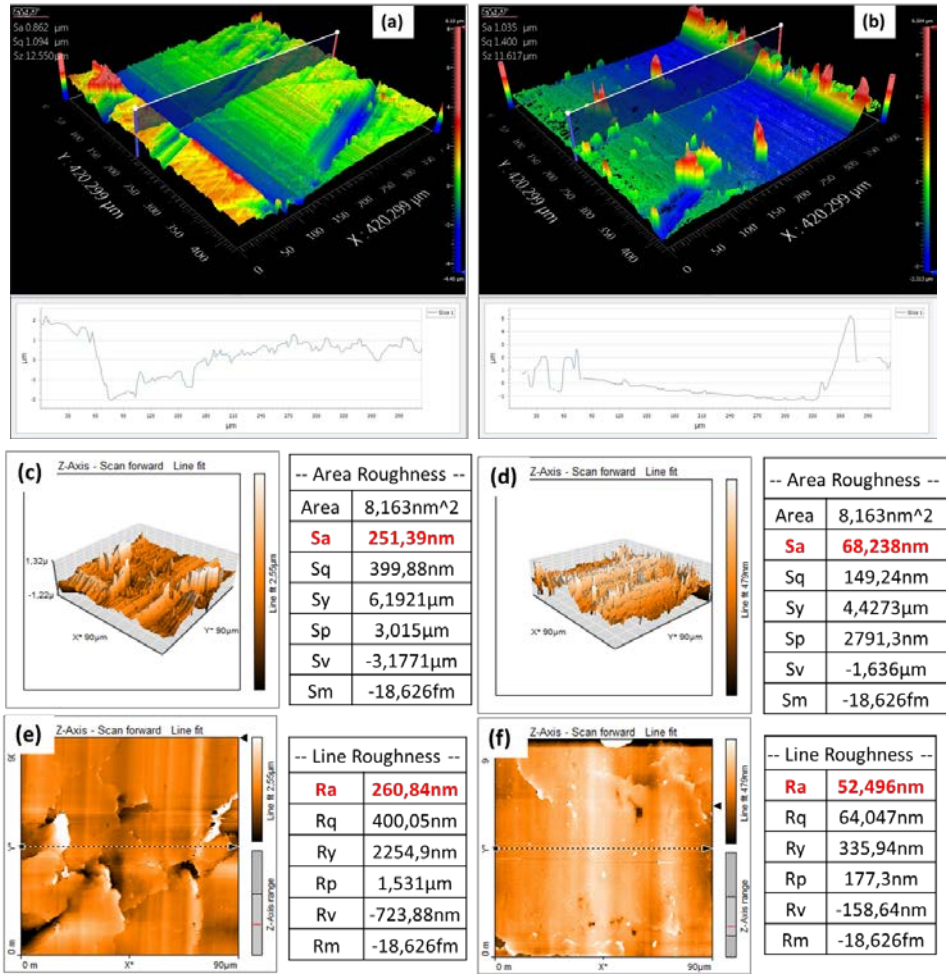

-- Area Roughness --	
Area	8,163nm^2
Sa	**251,39nm**
Sq	399,88nm
Sy	6,1921µm
Sp	3,015µm
Sv	-3,1771µm
Sm	-18,626fm

-- Area Roughness --	
Area	8,163nm^2
Sa	**68,238nm**
Sq	149,24nm
Sy	4,4273µm
Sp	2791,3nm
Sv	-1,636µm
Sm	-18,626fm

-- Line Roughness --	
Ra	**260,84nm**
Rq	400,05nm
Ry	2254,9nm
Rp	1,531µm
Rv	-723,88nm
Rm	-18,626fm

-- Line Roughness --	
Ra	**52,496nm**
Rq	64,047nm
Ry	335,94nm
Rp	177,3nm
Rv	-158,64nm
Rm	-18,626fm

Figure 21 Optical 3D, 3D and Sa of AFM, 2D and Ra of AFM of the cylinder liner surface rubbed under 1st piston ring with 5W-40 engine oil (a, c, e) and 5W-40 engine oil+B (b, d, f).

Figure 21 shows 3D digital optical microscopy, 3D and (surface average) Sa of AFM, 2D and (roughness average) Ra of AFM of the cylinder liner surface rubbed under 1st piston ring with 5W-40 engine oil (a, c, e), and 1st piston ring surface tested with 5W-40 engine oil+B (b, d, f), respectively. Sa (68.238nm) and Ra (52.196nm) of the surface tested with 5W-40 engine oil+B were found lower than the test Sa (251.39nm) and Ra (260.84nm) with 5W-40 engine oil as presented in Table 2.

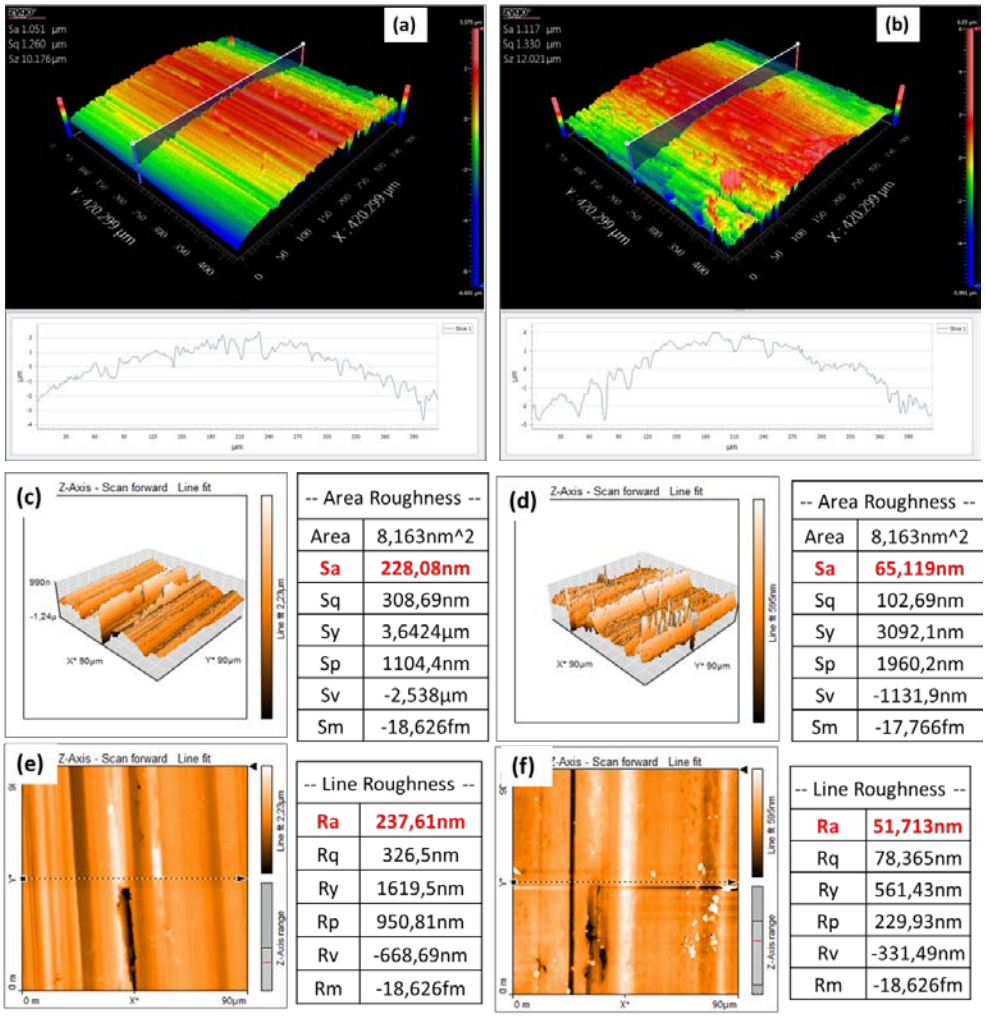

-- Area Roughness --	
Area	8,163nm^2
Sa	**228,08nm**
Sq	308,69nm
Sy	3,6424µm
Sp	1104,4nm
Sv	-2,538µm
Sm	-18,626fm

-- Area Roughness --	
Area	8,163nm^2
Sa	**65,119nm**
Sq	102,69nm
Sy	3092,1nm
Sp	1960,2nm
Sv	-1131,9nm
Sm	-17,766fm

-- Line Roughness --	
Ra	**237,61nm**
Rq	326,5nm
Ry	1619,5nm
Rp	950,81nm
Rv	-668,69nm
Rm	-18,626fm

-- Line Roughness --	
Ra	**51,713nm**
Rq	78,365nm
Ry	561,43nm
Rp	229,93nm
Rv	-331,49nm
Rm	-18,626fm

Figure 22 Optical 3D, 3D and Sa of AFM, 2D and Ra of AFM of the 2nd piston ring surface tested with 5W-40 engine oil (a, c, e) and 5W-40 engine oil+B (b, d, f).

Figure 22 shows 3D digital optical microscopy, 3D and (surface average) Sa of AFM, 2D and (roughness average) Ra of AFM of the 2nd piston ring surface tested with 5W-40 engine oil (a, c, e), and 1st piston ring surface tested with 5W-40 engine oil+B (b, d, f), respectively. Sa (65.119nm) and Ra (51.713nm) of the surface tested with 5W-40 engine oil+B were found lower than the test Sa (228.08nm) and Ra (237.61nm) with 5W-40 engine oil as presented in Table 2.

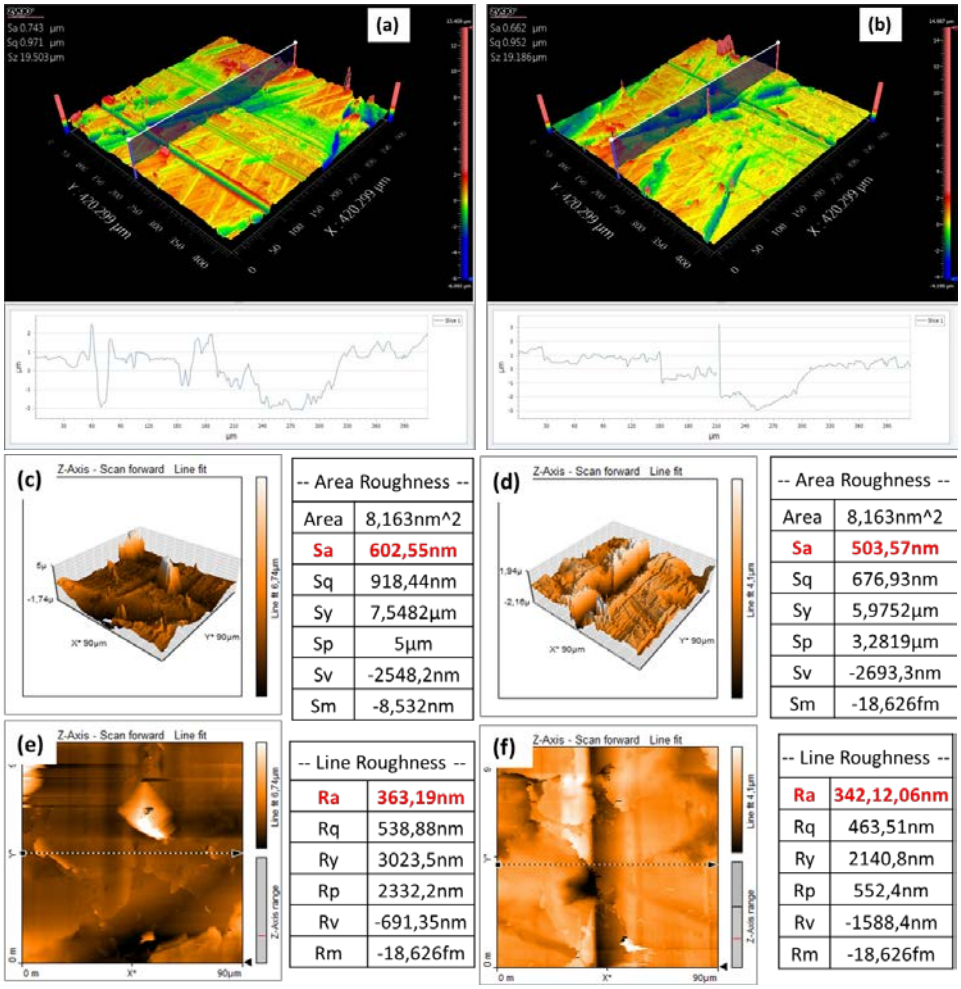

-- Area Roughness --	
Area	8,163nm^2
Sa	602,55nm
Sq	918,44nm
Sy	7,5482µm
Sp	5µm
Sv	-2548,2nm
Sm	-8,532nm

-- Area Roughness --	
Area	8,163nm^2
Sa	503,57nm
Sq	676,93nm
Sy	5,9752µm
Sp	3,2819µm
Sv	-2693,3nm
Sm	-18,626fm

-- Line Roughness --	
Ra	363,19nm
Rq	538,88nm
Ry	3023,5nm
Rp	2332,2nm
Rv	-691,35nm
Rm	-18,626fm

-- Line Roughness --	
Ra	342,12,06nm
Rq	463,51nm
Ry	2140,8nm
Rp	552,4nm
Rv	-1588,4nm
Rm	-18,626fm

Figure 23 Optical 3D, 3D and Sa of AFM, 2D and Ra of AFM of the cylinder liner surface rubbed under 2nd piston ring with 5W-40 engine oil (a, c, e) and 5W-40 engine oil+B (b, d, f).

Figure 23 shows 3D digital optical microscopy, 3D and (surface average) Sa of AFM, 2D and (roughness average) Ra of AFM of the cylinder liner surface rubbed under 2nd piston ring with 5W-40 engine oil (a, c, e), and 1st piston ring surface tested with 5W-40 engine oil+B (b, d, f), respectively. Sa (503.57nm) and Ra (342.12nm) of the surface tested with 5W-40 engine oil+B were found lower than the test Sa (602.55nm) and Ra (363.19nm) with 5W-40 engine oil as presented in Table 2.

These results determine that BA was more effective to protect the surface on cylinder liner than piston ring. Thus, the amount of B has been found higher in elemental analysis of the rubbed cylinder liner according to the piston ring. The main reason is the degree of the surface degradation. Not only chemical mechanism, but also mechanical mechanism is also the main factor which play an important role in the activation of NBA and additives to form the protective layers on the wear track. In micro experiments, the formal tests conditions were determined and they concluded that the surface degradation is a mechanical action and

favours chemical reaction; so that satisfactory degradation or sufficiently smoothed surface where the additives act with respect to the intensity of degradation (so that having perfect activated surface) allow higher amount of additive layer protection on the wear track.

To prove this results; Friction force and COF of **cylinder liner surface** rubbed under ***1st and 2nd piston ring*** with 5W-40 and 5W-40 engine oil+B engine oil were measured also in Nanoscale. Friction Force is obtained in V. It is calibrated and obtained in nN. Then COF is calculated in Nanoscale form. Figures 24, 25, 26, 27 show ***COF of friction force in Nanoscale of cylinder liner surface rubbed under 1st piston ring with 5W-40 engine oil.***

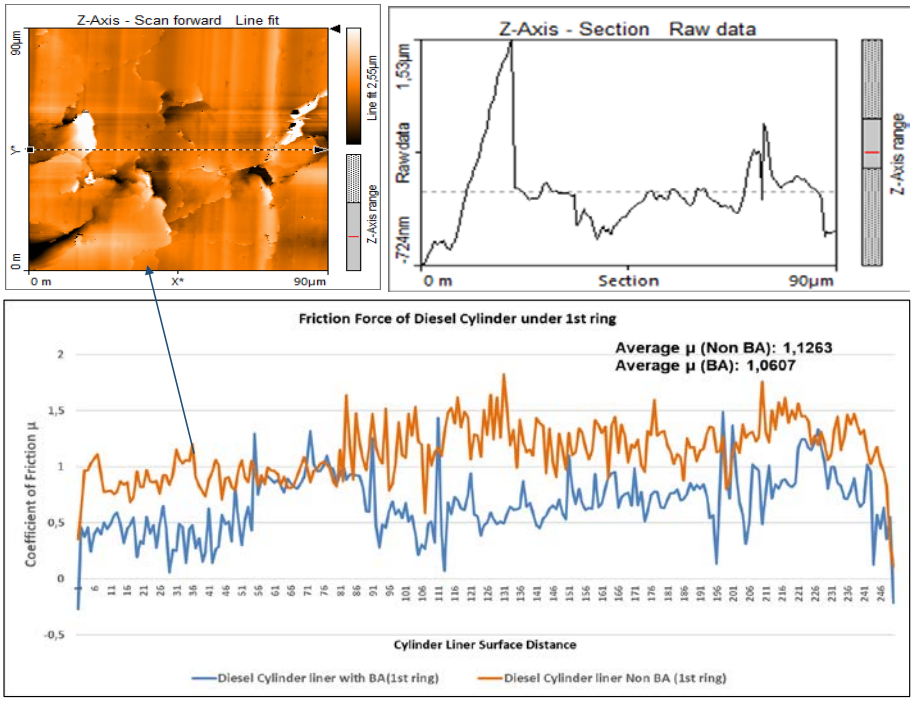

Figure 24. COF in Nanoscale of cylinder liner surface rubbed under 1st piston ring with 5W-40 engine oil

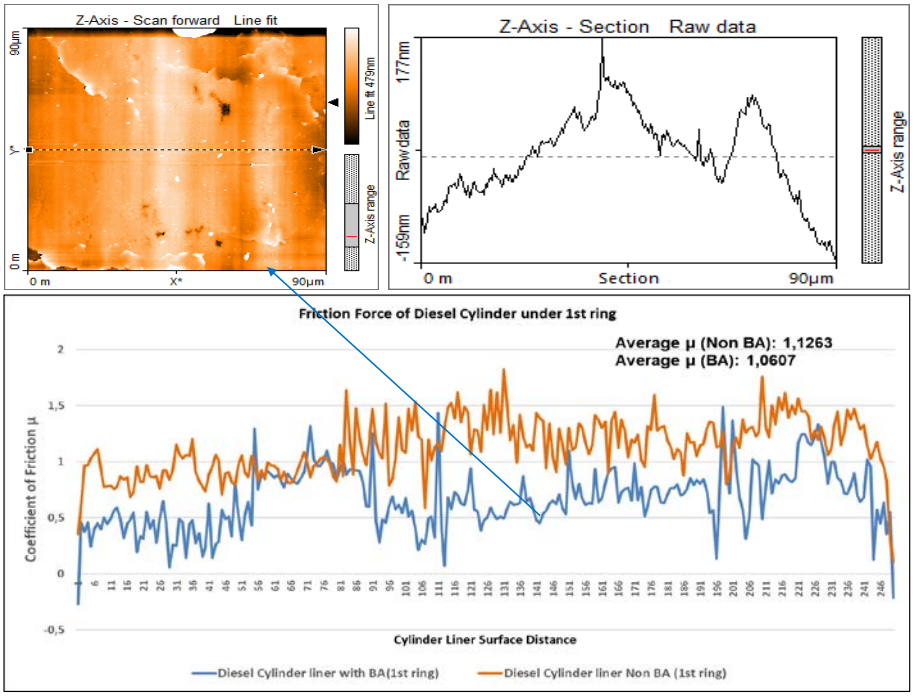

Figure 25. COF in Nanoscale of cylinder liner surface rubbed under 1st piston ring with 5W-40 engine oil+B

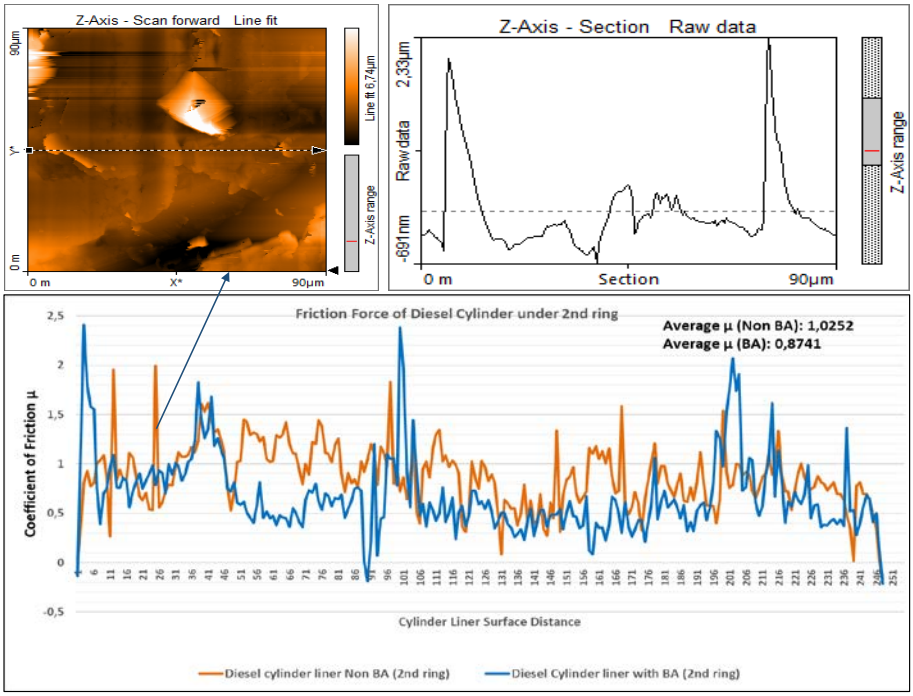

Figure 26. COF in Nanoscale of cylinder liner surface rubbed under 2nd piston ring with 5W-40 engine oil

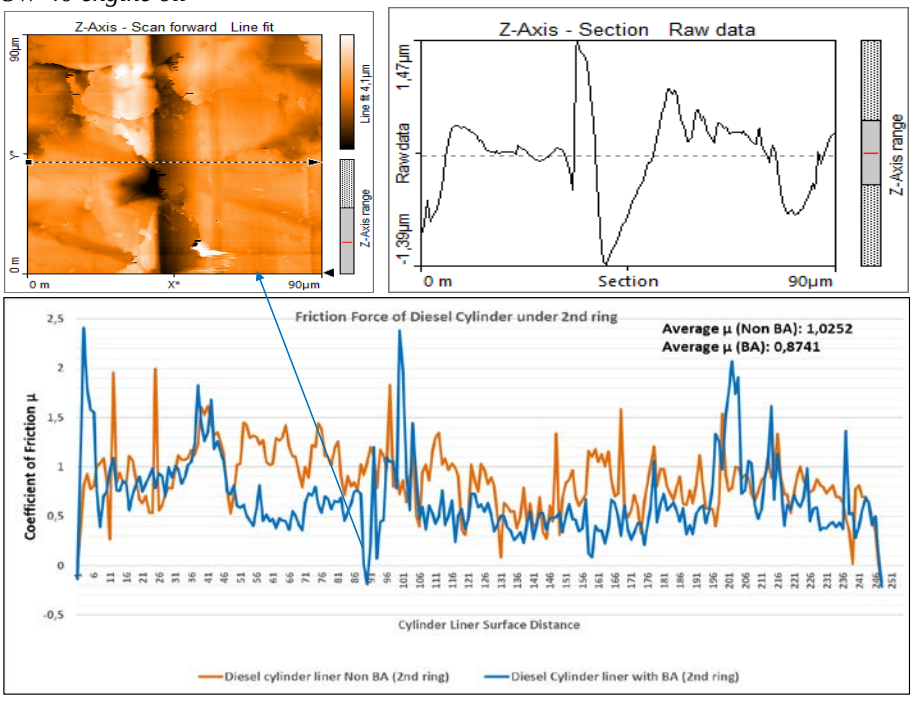

Figure 27. COF in Nanoscale of cylinder liner surface rubbed under 2nd piston ring with 5W-40 engine oil 5W-40 engine oil+B

3 CONCLUSIONS

New invention came out with the successful suspension of nano boric acid (BA) additive added into 5W-40 fully synthetic commercial lubricating oil. This invention is well proved with Turbiscan analyze.

Lubricant with BA additive showed almost similar friction results with the tests of 1st piston ring against cylinder liner and obtained less friction, better lubrication and protective performance then oil without containing BA with the tests of 2nd ring against cylinder liner.

COF of friction force in Nanoscale of cylinder liner surface rubbed under 1st and 2nd piston ring presented less friction, better lubrication and protective performance then oil without containing BA.

Protective layer of suspended nano boric acid is well determined with B element on the surface examination with TEM, Turbiscan, FESEM, X-Ray, mapping, AFM for the 1st and 2nd piston rings and cylinder liners, respectively. 3D surface and roughness average (Sa) and (Ra) showed lower values with 5W-40 engine oil containing BA then 5W-40 engine oil on the wear track of cylinder liners. It should be imphasized that 5W-40 engine oil is well known fully formulated oil marketed in the world.

ACKNOWLEDGMENTS

The authors would like to thank to Mr. Murat ÖZAYMAN, Head of Tribor ARGE Co. in Technology Transfer Office-Technopark of YILDIZ Technical University in Istanbul-TURKEY.

REFERENCES

[1] Erdemir A.:"Review of engineered tribological interfaces for improved boundary lubrication", Tribology International 38 (2005) 249–256.

[2] Richardson D. E. :"Review of Power Cylinder Friction for Diesel Engines". J. Eng. Gas Turbines Power. Oct 2000, 122(4): 506-519.

[3] Priest M, Taylor CM. :"Automobile engine tribology—approaching the surface", Wear 2000;241:193–203.

[4] Taylor CM. "Automobile engine tribology—design considerations for efficiency and durability", Wear 1998;221:1–8.

[5] Mohamed Kamal Ahmed A. Xianjun H. and Jiang H. :"Lubrication mechanism analysis of nickel-carbon-based tribological layer on sliding interfaces in automotive engines", Tribology International, 2024:195- 109595.

[6] Mohamed Kamal Ahmed A. Xianjun H. Mai L. Qingping C. Turkson R. F. and Bicheng C. :"Improving the tribological characteristics of piston ring assembly in automotive engines using Al2O3 and TiO2 nanomaterials as nano-lubricant additives", Tribology International, 2016:103-540-554.

[7] Laad M. Kumar V. Jatti S. :"Titanium oxide nanoparticles as additives in engine Oil" Journal of King Saud University - Engineering Sciences, 2018:30-2 116-122.

[8] Mohamed Kamal Ahmed A. and Xianjun H. :"Exploring the lubrication mechanism of CeO2 nanoparticles dispersed in ngine oil by bis(2-ethylhexyl) phosphate as a novel antiwear additive". Tribology International 165 (2022) 107321.

[9] Qifan Y., Xianjun H., Longxiang Z., Hua J., Yuxin M, Mohamed Kamal Ahmed A., :"Elaboration of thermophysical performance enhancement mechanism of functionalized boron nitride/graphite hybrid nanofluid", Advanced Powder Technology 34 (2023) 104047.

[10] Wu Y.Y., Tsui W.C,. Liu T.C., :"Experimental analysis of tribological properties of lubricatingoils with nanoparticle additives", Wear 262 (2007) 819–825.

[11] Padgurskas J., Rukuiza R., Prosyc˘evas I., Kreivaitis R. :"Tribological properties of lubricant additives of Fe, Cu and Co nanoparticles", Tribology International, 60, 2013, 224-232.

[12] Erdemlr A., Fenske G.R., Erck R.A. Nichols F.A., Busch D.: "Tribological Properties of Boric Acid and Boric-Acid-Forming Surfaces: Paet II: Formation and Self-Lubrication Mechanisms of Boric Acid CFilms On Boron and Boric- Oxid Containing Surfaces", Conference: 45. annual meeting of the Society of Tribologists and Lubrication Engineers, Denver, CO (USA), 7-10 May 1990.

[13] Erdemlr A., Halter M., Fenske G.R.: "Preparation of ultralow-friction surface films on vanadium diboride", Wear 205 (1997) 236-239.

[14] Lovell M. R., Kabir M. A., Menezes P. L. C. Higgs F.: "Influence of boric acid additive size on green lubricant performance", Phil. Trans. R. Soc. A (2010) 368, 4851-4868.

[15] Gregory Sawyer W., Ziegert J. C., Schmitz T. L., Barton T.: “In Situ Lubrication with Boric Acid: Powder Delivery of an Environmentally Benign Solid Lubricant”, Tribology Transactions, 49: 284-290, 2006.

[16] Erdemlr A., Erck R. A.: “Relationship of hertzian contact pressure to friction behavior of self-lubricating boric acid films “, Surface and coatings Technology, 49(1991) 435-438.

[17] Erdemlr A., Fenske G.R. Erck R. A.:” A study of the formation and self-lubrication mechanisms of boric acid films on boric oxide coatings”, Surface and Coatings Technology, 43/44 (1990) 588—596.

[18] Calhoun S. F.:”Antiwear and Extreme Pressure Additives for Greases”, A S L E Transactions Volume 3, 1960 - Issue 2, 208-214.

[19] Vadiraj A., Manivasagam G., Kamani K., Sreenivasan V.S.: “Effect of Nano Oil Additive Proportions on Friction

[20] and Wear Performance of Automotive Materials”, Tribology in Industry, Vol. 34, No 1 (2012) 3-10.

[21] Hwang Y., Lee C., Choi Y., Cheong S., Kim D., Lee K., Lee J., Kim S. H.: “Effect of the size and morphology of particles dispersed in nano-oil on friction performance between rotating discs”, Journal of Mechanical Science and Technology 25 (11) (2011) 2853~2857.

MOBILITY & VEHICLE MECHANICS

https://doi.org/10.24874/mvm.2025.51.03.02
UDC:
621.434:621.43.032.26:621.43.018.7:621.43.019.2

GASOLINE DIRECT INJECTION STRATEGY ANALYSIS FOR IMPROVED COMBUSTION STABILITY DURING SIDI ENGINE WARM-UP OPERATION

Nemanja Bukušić[1], Predrag Mrđa[2], Marko Kitanović[3], Nenad Miljić[4], Slobodan Popović[5]*

Received in August 2024 *Accepted in October 2024*

RESEARCH ARTICLE

ABSTRACT: Energy efficiency drives the ICE development for more than a century, while ever-increasing ecology awareness in the last decades and requests for the reduction of toxic and CO2 emissions, lead to complex and demanding driving cycles and put severe challenges in the optimization of critical operation regimes to secure ICE application. The Spark Ignition Direct Injection Engine (SIDIE) featuring high boost and high compression ratio, Variable Valve Timing (VVT), complex injection strategies and combustion systems (HCCI/SACI), seems to be an effective response to high demands. Cold start/warm-up, regardless of combustion system applied, is a critical part of emission certification procedure in all standard driving cycles. Catalyst efficiency depends on temperature and engine capability to produce the exhaust gas heat flux necessary for its warm-up. A specific test procedure was designed and performed on Spark Ignition Single Cylinder Research Engine (SI-SCRE) to investigate and evaluate the influence of DI strategy set-up on the capability to provide fast catalyst warm-up during low-temperature/low-load operation. Double injection strategies in terms off Start of Injection (SOI), Split Factor (SF) and Rail Pressure (RP) were tested and analysed against combustion dynamics and combustion stability parameters obtained from in-cylinder pressure indication and complex thermodynamic post-processing.

KEY WORDS: *Spark ignition direct injection, warm-up operation, split injection, combustion dynamics, combustion stability*

[1]*Nemanja Bukušić, University of Belgrade, Faculty of Mechanical Engineering, Kraljice Marije 16 11000 Belgrade Serbia, nbukusic@mas.bg.ac.rs, https://orcid.org/0000-0002-1137-3481, (*Corresponding author)*
[2] *Predrag Mrđa, University of Belgrade, Faculty of Mechanical Engineering, Kraljice Marije 16 11000 Belgrade Serbia, pmrdja@mas.bg.ac.rs, https://orcid.org/0000-0001-5534-6322*
[3] *Marko Kitanović, University of Belgrade Faculty of Mechanical Engineering, Kraljice Marije 16 11000 Belgrade Serbia, mkitanovic@mas.bg.ac.rs, https://orcid.org/0000-0002-3931-802X*
[4] *Nenad Miljić, University of Belgrade, Faculty of Mechanical Engineering , Kraljice Marije 16 11000 Belgrade Serbia, nmiljic@mas.bg.ac.rs, https://orcid.org/0000-0003-3564-0203*
[5] *Slobodan Popović, University of Belgrade, Faculty of Mechanical Engineering, Kraljice Marije 16 11000 Belgrade Serbia, spopovic@mas.bg.ac.rs, https://orcid.org/0000-0002-6332-9589*

ANALIZA STRATEGIJE DIREKTNOG UBRIŽANJA BENZINA ZA POBOLJŠANU STABILNOST SAGOREVANJA TOKOM ZAGREVANJA SIDI MOTORA

REZIME: Energetska efikasnost pokreće razvoj motora sa unutrašnjim sagorevanjem više od jednog veka, dok sve veća ekološka svest u poslednjim decenijama i zahtevi za smanjenjem emisije toksičnih materija i CO_2 dovode do složenih i zahtevnih ciklusa vožnje i postavljaju ozbiljne izazove u optimizaciji kritičnih režima rada kako bi se osigurala primena motora sa unutrašnjim sagorevanjem. Motor sa direktnim ubrizgavanjem (SIDIE), koji se odlikuje visokim pritiskom i visokim stepenom kompresije, promenljivim vremenom rada ventila (VVT), složenim strategijama ubrizgavanja i sistemima sagorevanja (HCCI/SACI), čini se da je efikasan odgovor na visoke zahteve. Hladni start/zagrevanje, bez obzira na primenjeni sistem sagorevanja, ključni je deo postupka sertifikacije emisija u svim standardnim ciklusima vožnje. Efikasnost katalizatora zavisi od temperature i sposobnosti motora da proizvede toplotni fluks izduvnih gasova neophodan za njegovo zagrevanje. Specifična procedura ispitivanja je dizajnirana i izvršena na jednom cilindričnom istraživačkom motoru sa unutrašnjim sagorevanjem (SI-SCRE) kako bi se istražio i procenio uticaj podešavanja DI strategije na sposobnost brzog zagrevanja katalizatora tokom rada na niskoj temperaturi/niskom opterećenju. Strategije dvostrukog ubrizgavanja u smislu početka ubrizgavanja (SOI), faktora podele (SF) i pritiska u šini (RP) testirane su i analizirane u odnosu na dinamiku sagorevanja i parametre stabilnosti sagorevanja dobijene iz indikacije pritiska u cilindru i složene termodinamičke postprocesne obrade.

KLJUČNE REČI: *Direktno ubrizgavanje sa paljenjem svećicom, rad zagrevanja, podeljeno ubrizgavanje, dinamika sagorevanja, stabilnost sagorevanja*

GASOLINE DIRECT INJECTION STRATEGY ANALYSIS FOR IMPROVED COMBUSTION STABILITY DURING SIDI ENGINE WARM-UP OPERATION

Nemanja Bukušić, Predrag Mrđa, Marko Kitanović, Nenad Miljić, Slobodan Popović

INTRODUCTION

The low fuel consumption, and corresponding CO_2 emission, are two of the main objectives of the optimization during testing on reference driving cycles. European emissions regulations are not only about limiting CO_2 emissions, but also about limiting emissions of toxic exhaust gas components, such as carbon monoxide (CO), unburned hydrocarbons (HC) and nitrogen oxides (NOx), which are the consequence of combustion reactions dynamics and complexity. These harmful components of the exhaust gases can be eliminated to a considerable extent, but unfortunately not completely by subsequent exhaust gas treatment. One way to achieve this, in engines operating with a stoichiometric mixture, is to use a three-component catalyst.

Three-component catalytic converters (TWC or 3WC) have proven to successfully cope with the ever more stringent emission limits, being able to convert more than 95% of the relevant raw engine-out emissions under nominal operating conditions. However, as long as the temperature of the TWC is below the "light-off temperature" of around 250 °C, its conversion rate is significantly reduced. Consequently, a large portion of the raw engine-out emissions emitted into the atmosphere remains untreated [1].

Therefore, one of the main tasks, in addition to reducing fuel consumption, is to reach the catalytic converter optimal efficiency as soon as possible after the cold start. Strategies for the catalyst heating phase can be categorized as follows:

Strategies with additional hardware components enabling fast catalyst heating-up process, such as secondary air pumps [5–7] or electric heaters [8,9].

Strategies without any additional hardware components, based on dedicated combustion control techniques that in turn generate hot exhaust gas.

In this paper, special attention is paid to the second strategy, more specifically to the double injection strategy as a part of the entire engine control strategy. After an introductory analysis of the combustion problem in gasoline engines and a comparative review of the reference driving cycles, a detailed analysis of the engine injection control parameters that affect the enthalpy of exhaust gases was performed.

1 DRIVING CYCLES

Vehicle exhaust emissions tests incorporate specific test procedures based on driving cycles which in turn can be performed on test benches or in real road driving conditions, such as:

- NEDC (New European Driving Cycle), designed in the 1980s and became outdated today due to continuous evolutions in automotive technology, changes in driving conditions and driving styles.
- WLTC (Worldwide harmonized Light vehicle Test Cycle)
- RDE (Real Driving Emission test) step 1 (with a NOx conformity factor of 2.1) is applied since September 2017 to new car types, and It from September 2019 for all types.

- RDE step 2 (with a NOx conformity factor of 1.0 plus an error margin of 0.5) is applied from January 2020 for new types and from January 2021 for all types.

Quite opposite to the technology used for the WLTC, which is based on real-driving data, the old NEDC test was based on a theoretical driving profile. Driving conditions have also changed since the 1980s with increased traffic congestion, resulting in more inefficient driving. Additionally, driving styles have also changed. In some countries the new car sales are driven by the companies whose drivers use a company fuel card usually not considering the fuel economy as the highest priority. Therefore, NEDC isn't as representative of today's driving profiles as it was to be in the past.

Figure 1 depicts direct comparison of the vehicle speed profile and simulated engine coolant temperature during the NEDC and WLTC [2]. In Table 1 the main descriptive parameters of these two cycles are given. Operating cold engine increases harmful exhaust emissions and CO_2, due to higher mechanical friction (higher lubricant viscosity, parts tolerances), and mostly due to inefficient combustion process during warm-up (fuel atomization/evaporation, mixture strength, heal losses). The absolute contribution of a cold start to emissions is almost the same across all standardized driving cycles, but its impact on the total emissions during the reference cycles decreases with increased distance travelled by the vehicle during testing. Considering the simple correction for the test distance, which is shown by the expression (1), the effect of the warm-up sequence in the WLTC can be roughly approximated to roughly 50% lower values than in case of NEDC.

$$\Delta CO_{2wltc} = \Delta CO_{2nedc} \cdot \frac{11{,}03}{23{,}27}, \tag{1}$$

The tested vehicle is conditioned before being tested at a constant ambient temperature, being specific to test procedure. For the NEDC, the temperature range during the start is between 20 °C and 30 °C, while for the WLTC the range is 23 ± 5 °C. As an example, the engine starting coolant temperature impact on CO_2 emissions (gCO_2/km) in NEDC, relative to standard starting condition is presented in Figure 2 [3]. Carbon dioxide emissions can be increased by up to 19% when starting from -7°C and decreased by roughly 12% when the engine is fully warmed.

Table 1 Comparative specification of NEDC and WLTC

	Units	NEDC	WLTC
Start conditions		cold	cold
Duration	s	1180	1800
Distance	km	11,03	23,27
Mean velocity	km/h	33,6	46,5
Max. velocity	km/h	120	131,3
Stop phases		14	9
Duration of stops	s	280	226
Duration of constant speed	s	475	66
Duration of acceleration	s	247	789
Duration of deceleration	s	178	719
Percentage of stops	%	23,7	12,6

Percentage of constant speed	%	40,3	3,7
Percentage of accelerations	%	20,9	43,8
Percentage of deceleration	%	15,1	39,9

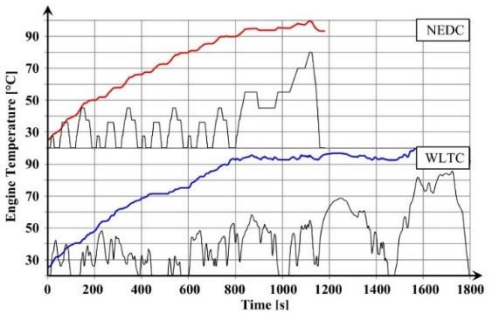

Figure 1 Simulated engine temperature along NEDC and WLTC for DISI-ICE powered vehicles [2]

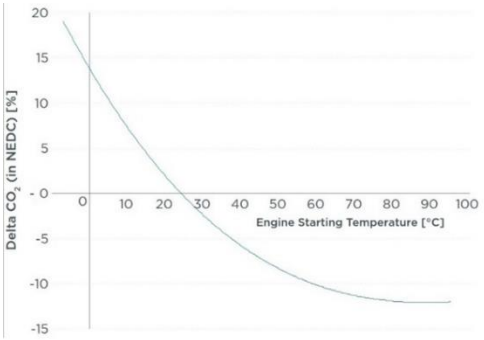

Figure 2 Engine starting temperature impact on CO2 emissions in NEDC (11.03 km) [3]

1.1 Combustion process stability in forced heating regimes of a 3WC

Emission test procedures usually incorporate specific phase during which the engine idles shortly before take-off. This stage is further divided into two parts with completely different requirements. The first one, lasting a few seconds, is the starting of the engine, which should enable reliable starting of the engine to idling. The next one is the TWC heating phase during which the catalyst is supposed to reach the temperature at which it may operate, taking few tens of seconds. The initial idle phase during the cold start period takes roughly 11 s in test procedures based both on both NEDC and WLTC. For example, even in the case of standard pre-conditioned ambient temperature of roughly 25 °C, this is far from sufficient to heat the TWC over 250 °C at which it can operate at efficiency of as low as 50%. Therefore, most of the emissions during the test cycle come from the initial critical part of the cycle.

Generally, forced TWC warm-up strategies through dedicated combustion control algorithms, rely on the combustion phase-out from optimal advanced to suboptimal (inefficient) retarded ignition (aTDC), yielding higher exhaust temperatures and enthalpy due to late combustion process that can even extend into the exhaust stroke.

The main issue in terms of control the combustion in the expansion stroke is that the mixture pressure and the temperature are continuously decreasing during the combustion delay phase which is critical and adversely affects the formation of the flame kernel and stable flame propagation in subsequent combustion stages. The heat losses are also critical due to continuously increasing combustion chamber surface during expansion superimposed to already low combustion chamber walls temperatures. Therefore, misfire represented statistically by largely increased deviation of all combustion dynamics parameters, is ever present, but certainly inadmissible from the aspect of exhaust emissions.

This strategy may benefit from Split Direct Injection (SDI) and produce larger combustion phase-out. Provided the optimized SDI combined with mixture turbulence, rich and ignitable mixture around the spark electrodes may be produced, enabling more stable combustion

process even at retarded ignition. Balance between the late ignition and late combustion based on SDI from which TWC warm-up time surely benefits and affected efficiency and emission will depend to specific boundary conditions (specific application and test requirements) [4].

2 TESTBED SETUP AND PRODUCERS

The tests which are to simulate catalyst heating was performed on a Direct Injection Spark Ignition Single Cylinder Research Engine (DISI-SCRE). Test bed configuration with engine auxiliaries is presented in Figure 3. The engine is of modular type allowing engine components change according to the test specification (piston, cam shafts, injectors etc.). Engine systems are external (cooling, lubricating, charging, etc.), independent of the engine itself and independent and flexible in terms of control and adjustments according to the test specification. Charging is realized by a separate compressor, while the exhaust back-pressure (flow resistance and pressure drop over charger turbine) is controlled using external turbocharger turbine simulator. The engine technical specification is given in Table 2.

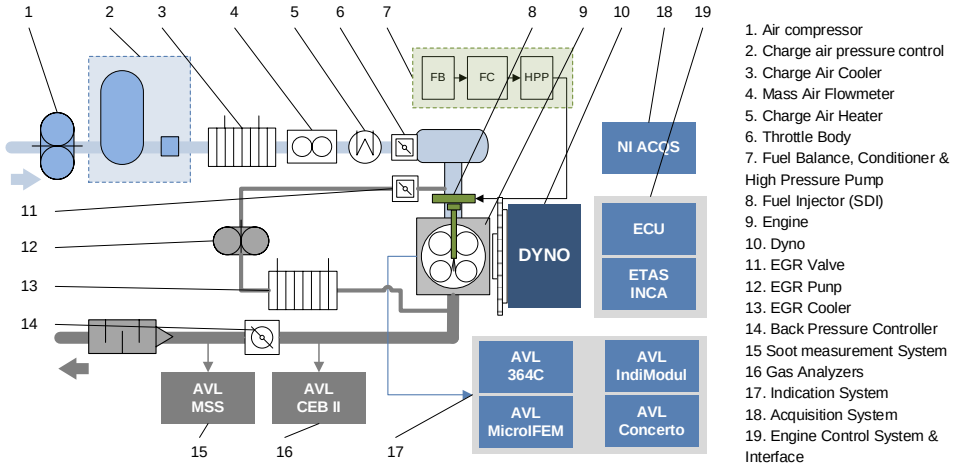

Figure 3 Schematic diagram of the test bench

Table 2 SCRE technical specification

Parameter	Nomenclature	Value	Unit
Bore	D	82	mm
Stroke	S	90	mm
Working displacement	V_h	475	cm^3
Conrod length	L	144	mm
Pin offset	b	-0.5	mm
Compression ratio	ε	11.5	-
Inlet valve opening	IVO	30	^oCA aTDC
Inlet valve closing	IVC	40	^oCA aBDC
Exhaust valve opening	EVO	44	^oCA bBDC
Exhaust valve closing	EVC	13	^oCA bTDC

3 TEST PROCEDURES

A specific catalyst heating test procedure – CatHeat – was designed as to investigate and evaluate the influence of injection and ignition strategy on the capability to provide higher exhaust temperature and in turn faster catalyst warm-up during the low-temperature/low-load operation specific to the starting sequence of a reference driving cycle. In this work, double injection strategies were tested and analyzed against combustion dynamics and combustion stability parameters obtained from in-cylinder pressure indication and thermodynamic post-processing. Setup parameters covered within separate group of variation tests are as follows:

- The start of the first injection sweep (SOI1);
- The start of the second injection sweep (SOI2);
- The ratio of the fuel mass injected during the first and second injection - Split Factor sweep (SF);
- Fuel injection pressure or fuel rail pressure sweep (RP).

Engine warm-up, under conditions in which the engine parts, coolant and lubricating oil temperatures are close to the ambient temperature is a critical part of the standard driving cycle. Therefore, the oil and coolant temperatures were maintained at 35 °C during the test. The engine crankshaft speed (n) and indicated mean effective pressure (IMEP) were set to the expected average values at engine idle. Maintaining the IMEP at a given level is achieved by means of the throttle position. Mixture strength was maintained stoichiometric during test campaign by controlling the injection timings (Δt_{INJ1}, Δt_{INJ2}). Being focused on injection strategies exclusively, spark advance was set constant at and shifted after TDC, as to enable the combustion shift further into expansion stroke and so increase the exhaust temperature. Each of the 4 tests yielded one optimal setup for the varied parameter, which was then adopted as a constant in subsequent tests. The initial values and ranges for given parameters in the tests are given in Table 3.

Table 3 The initial engine setup

Description	Designation	Unit	Initial Value	Variation range
Engine speed	n	min^{-1}	1200	-
Indicated Mean Effective Pressure	IMEP	bar	2	-
Spark angle	SA	°CA aTDC	10	-
Excess air coefficient	λ	-	1.00	-
Start of the first injection	SOI1	°CA bTDC	330	-330…(5)…-245
Start of the second injection	SOI2	°CA bTDC	235	-250…(5)…-70
Fuel rail pressure	p_RAIL	bar	100	50…(25)…200
Fuel mass split factor	SF	$\%m_{F,INJ1}$ vs. $\%m_{F,INJ2}$	[70_30]	[80_20]…[40_60]

3.1 Measurements and data analysis

Usual representation of combustion dynamics based on identification of angular positions where predefined fraction of the fuel/mixture is burned is used. Burn rates are derived and analyzed upon thermodynamic analysis of the in-cylinder indicated pressure traces, as follows:

Burn rate angles – the CA at which burn rate percentages of 5, 10, 50 and 90% are determined (MBF 05, MBF 10, MBF 50, MBF 90);

Combustion Duration (CD);

Statistical representation of combustion stability in form of coefficient of variance (CoV_05, CoV_10, CoV_50, CoV_90).

To eliminate the ever-present sudden changes and noise in indicated pressure measurements, fast data smoothing is applied using moving average on interval of ±2°CA. Considering low engine speed and stationary operation, the pressure transducer output was referenced to readings from intake manifold pressure transducer at BDC [10].

The analysis was performed using the AVL Concerto software package. Simplified method for the evaluation of the heat release rate is based on Rassweiler and Withrow method and improved lately by Hohenberg and Killman [11-13]. Assuming thermodynamic state change split in two quasi-stationary equilibrium steps – adiabatic compression (expansion) and isochoric heat supply:

$$p_{i+1,s} = p_i \cdot \left(\frac{V_i}{V_{i+1}}\right)^{\kappa_i}, \tag{2}$$

$$\Delta Q_i = m \cdot c_{v,i} \cdot \left(T_{i+1} - T_{i+1,s}\right). \tag{3}$$

This yields, upon simple transformation, expression for finite heat change:

$$\Delta Q_i = \frac{1}{\kappa_i - 1} \cdot V_{i+1} \cdot \left[p_{i+1} - p_i \cdot \left(\frac{V_i}{V_{i+1}}\right)^{\kappa_i}\right]. \tag{4}$$

Isentropic exponent depends on temperature and can be determined starting from the basic thermodynamic relation for specific heat capacities while specific heat capacity is approximated using empirical relation [12,13] and discrete adjustment for SI-ICE and homogenous charge (A=0,1):

$$\kappa_i = \frac{c_{pi}}{c_{vi}} = \frac{R + c_{vi}}{c_{vi}} \approx \frac{0{,}2888}{c_{vi}} + 1 \approx \frac{0{,}2888}{0{,}7 + \frac{p_i \cdot V_i}{m \cdot R} \cdot (0{,}155 + A) \cdot 10^{-3}} + 1. \tag{5}$$

This evaluation method is not featured by particularly high absolute accuracy, having in mind originally neglected heat transfer in combustion chamber. Short computing time and only a few external data required for processing make this method first choice for fast evaluation, on-line monitoring, and purposes of relative comparison. Accuracy of burn rate parameters determined in this way, however, is sufficient for comparative analysis [12,13].

The start and the end of combustion, based exclusively on theoretical approach are to be determined as the crankshaft positions where derivate of heat flux dQ/dα changes from zero to positive and positive to zero, respectively. In discrete methods, ignition delay will be usually represented by 1, 2 or 5% MFB. Combustion duration is calculated as the crank angle between the end of the ignition delay and typically 90, 95 or 99% MFB. Determining small or large percentages such as 1 or 99% can be difficult and insufficiently accurate due to the susceptibility of the calculation to the effects of noise with small pressure changes.

Considering constant spark advance for all tests, the start and the end of combustion are arbitrarily defined as MBF05 and MBF90, and consequently, the combustion duration is calculated as the difference of two:

$$CD = MFB90 - MFB05. \tag{6}$$

Considering combustion cycle during warm-up critical in terms of stability, statistical evaluation of variation of each parameter of interest (x) is performed based on the coefficient of variation (CoV) defined as the root-mean-square deviation (σ_x) normalized to mean value (μ_x):

$$CoV_x = \frac{\sigma_x}{\mu_x} = \frac{\sqrt{\frac{1}{n-1}(\sum x^2 - n \cdot {\mu_x}^2)}}{\mu_x} = \frac{\sqrt{\frac{1}{n-1}(\sum x^2 - (\sum x)^2)}}{\frac{1}{n}\sum x}. \tag{7}$$

4 RESULTS AND DISCUSSION

4.1 Start of injection – SOI1 test

The SOI1 sweep was performed in the range of -330…-245 °CA (ΔSOI1=5 °CA), while the other relevant parameters were set according to the starting values given in the Table 3. Figure 5 depicts the indicated mean effective pressure (IMEP) and the combustion duration (CD) vs. start of the first injection (SOI1), and additionally corresponding coefficients of variation for both parameters (CoV_IMEP and CoV_CD, respectively).

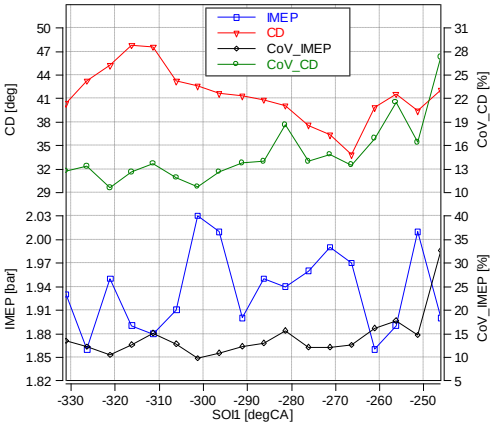

Figure 5 Indicated mean effective pressure (IMEP, CoV_IMEP), and combustion duration (CD, CoV_CD) vs. SOI1

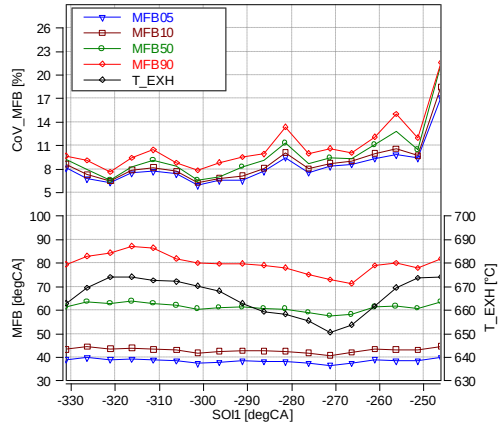

Figure 6 Mass fraction of burned fuel (MBF, CoV_MFB) and exhaust temp. vs. SOI1

The CoV_IMEP is considerably high ranging from 10 to 32% (15% for initial setup) which is up to 20 times higher value than usual for combustion process of the fully warmed-up SI engine. Significant change is observed for the case of the latest SOI1 (-245 °CA), indicating instable combustion due to compromised mixture formation caused by interaction of the fuel spray and intake valve. This correlates well with increased combustion duration covariance (CoV_CD). Combustion duration peak is observed in the range -320…-310 °CA, while the

minimum is found around -265 °CA. Figure 6 provides information on combustion dynamics. The MFB angles remain unchanged in observed SOI1 interval, but slightly better combustion stability is documented around SOI1=300 °CA. The CoV traces are fairly similar to each other but indicate the most stable operation in the SOI1 range of -320 and -300 °CA. Also, instable operation and misfire indicated by CoV_CD at the end of the SOI1 interval is confirmed by increased CoV values for all four values of MFB. The highest exhaust temperature (~675 °C), if neglected the local maximum observed at the end of the SOI1 range featured by most instable combustion, is also spotted in the SOI1 range of -320…-300 °CA. Considering slightly improved overall combustion stability around SOI1=300 °CA, this setup was adopted for the next test step.

4.2 Start of injection – SOI2 test

Based on the results of the previous analysis, with fixed SOI1=300 °CA, SOI2 sweep was performed within the range of -250...-70 °CA (ΔSOI2=5 °CA), keeping constant split factor (SF), spark advance (SA) and fuel rail pressure (p_RAIL) as defined in Table 3.

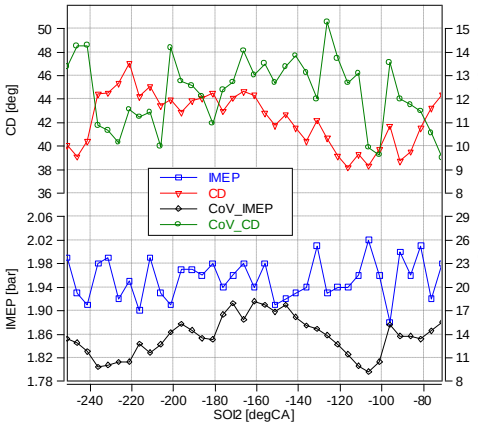

Figure 7 Indicated mean effective pressure (IMEP, CoV_IMEP), and combustion duration (CD, CoV_CD) vs. SOI2

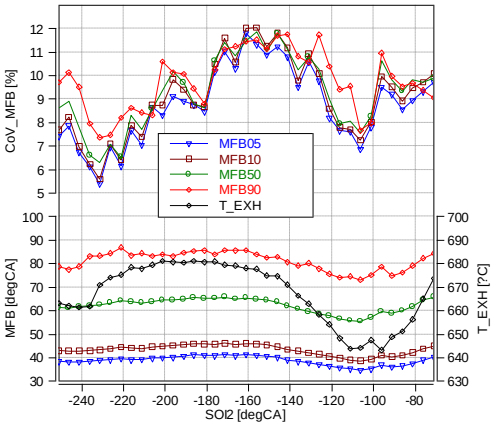

Figure 8 Mass fraction of burned fuel (MBF, CoV_MFB) and exhaust temp. vs. SOI2

In Figure 7, indicated mean effective pressure (IMEP), combustion duration (CD) and coefficients of variation for both parameters (CoV_IMEP and CoV_CD, respectively) are presented vs. start of the second injection (SOI2). The combustion stability indicated by the covariance of indicated pressure proved to be less prone to the influence of SOI2 change than it was in the case of SOI1 variation test. The CoV_IMEP was determined in the range of 10…18%. Considering split factor 70%-30%, results may point to the conclusion that variation of the SOI2 for 30% of injected fuel doesn't affect significantly the overall quality of mixture formation. The local minimums of the combustion duration (CD) were determined at the very start of the SOI2 range (-250…-245 °CA) and just before the piston reaches the mid-stroke (-110…-100 °CA) indicating most probably best results in mixture homogenization. Best results for combustion duration covariance are found close to the first minimum of combustion duration (-235…-200 °CA), but also at the very end of the SOI 2 range. Results of the combustion dynamics analysis presented in Figure 8 also indicate two narrow ranges in which MFB angles get local minimum corresponding well to the results for combustion duration. However, covariance traces point clearly at the start of the SOI2 range where covariances of all four MFB angles reach absolute minimums without exception. By

analyzing the exhaust temperature measurements, it appears that this range doesn't provide the highest results (~660 °C), but reasonably close to the absolute maximum (~680 °C), while maintaining overall better combustion stability. Considering that, SOI2=-235 °CA was determined setup for further test step.

4.3 Split factor test

The split factor (SF) sweep was performed by retaining unchanged spark advance and fuel rail pressure as defined in Table 3 and applying SOI1 and SOI2 optimums from previous tests (-300 and -235 °CA). Eight discrete fuel split factors (%mF,INJ1 vs. %mF,INJ2) were tested, namely 80-20, 70-30, 65-35, 60-40, 50-50, 40-60, 30-70 and 20-80.

In Figure 9, indicated mean effective pressure (IMEP), combustion duration (CD) and coefficients of variation for both parameters (CoV_IMEP and CoV_CD, respectively) are presented vs. injected fuel split factor. Combustion stability was determined in the range of 11 to 22%, reaching two local maximums – one at the very start of the of the range (80-20, 18%) and the second at the very end (20-80, 22%). Combustion duration shows strong dependance on split factor, being determined in the range of 36…42 °CA, while covariance was found in the range of 12,5% to 21%. By increasing the fraction of the second injection, the combustion duration decreases which indicates that fuel concentration in the upper parts of the combustion chamber, close to the spark plug, was evidently higher. Increased covariances of both parameters indicate compromised homogenization. Also, increased covariances at the start of the SF range points to almost equally poor mixture homogenization, most probably caused by fuel spray collision with piston crown since SOI1 is close to TDC.

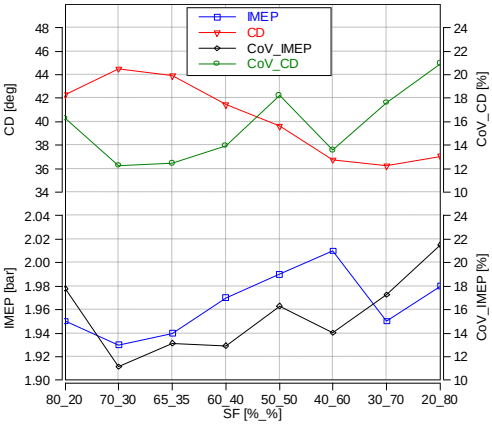

Figure 9 Indicated mean effective pressure (IMEP, CoV_IMEP), and combustion duration (CD, CoV_CD) vs. split factor (SF)

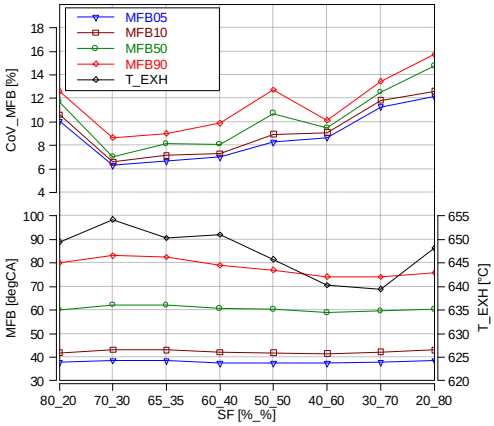

Figure 10 Mass fraction of burned fuel (MBF, CoV_MFB) and exhaust temp. vs. split factor (SF)

Heat release rate analysis presented in Figure 10 yields results similar to those gathered in previous SOI sweeps – MFB05 and MFB10 show no particular dependency to split factor, while MFB90 decreases with increased fraction of the second injection (local minimum MFB90=72 °CA at SF=40-60). Covariance traces follow the same dependence to SF reaching best values at SF=70-30 (7-8,5%) and indicating poor homogenization for increased portions of second injection (SF=40-60…20-80). The best covariance results for heat release rate parameters, expectedly correspond well to the highest exhaust temperature

measured in this test (~654 °C). For final fuel rail pressure variation test, SF=70-30 setup was adopted.

4.4 Fuel rail pressure (p_RAIL) test

Introducing the direct fuel injection in SI-ICE range opened wide range of problems previously exclusively related to mixture formation in CI-ICE, namely jet cone development, jet penetration, primary and secondary break-up, droplet break-up, collision and coalescence, flash boiling and evaporation. All named phenomena are highly dependent on changing thermodynamic conditions during intake and compression strokes and even more on injection pressure [14,15].

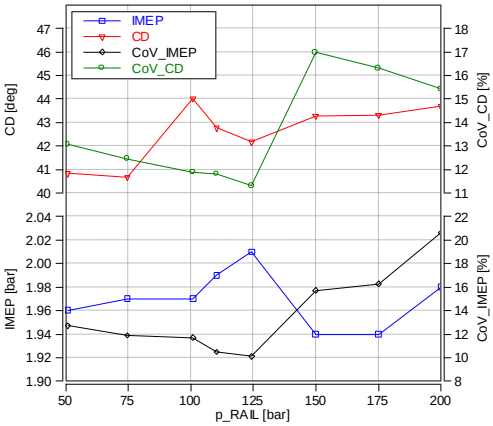

Figure 11 IMEP, IMEP_CoV, BDUR and BDUR_CoV vs. rail pressure(p_RAIL)

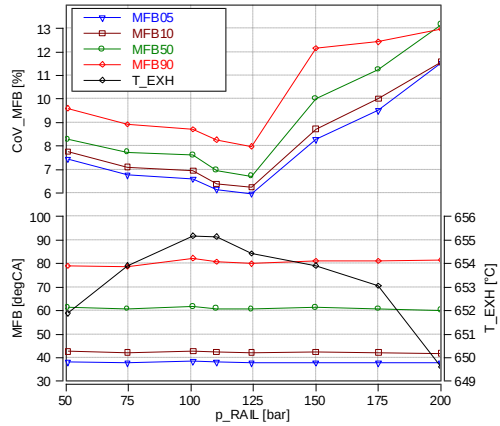

Figure 12 MBF, MBF covariance and exhaust temperature vs. rail pressure(p_RAIL)

Fuel rail pressure sweep was performed in the range of 50…200 bar (Δp_RAIL=25 bar). The low-to-mid pressure range is obviously favorable due to more energy efficient fuel injection process but also are more suitable for injection strategies performed during intake stroke and/or during the low-pressure range of the compression stroke. Setups gathered from previous tests meet these conditions and final setup for p_RAIL is expected to be found in the same pressure range.

In Figure 11, indicated mean effective pressure (IMEP), combustion duration (CD) and coefficients of variation for both parameters (CoV_IMEP and CoV_CD, respectively) are presented vs. rail pressure. The best overall process stability was determined between 100 and 125 bar. Combustion duration covariance minimum was also localized in that range. As for combustion heat release rate all MFB values proved to be less dependent to rail pressure variation, but covariances shown improvement in the range of 100…125 bar. Optimal rail pressure setup was identified by introducing additional test point at 110 bar giving further improvement in combustion stability. Covariances for MFB parameters were all found in the range of 6-8%, IMEP covariance was decreased to 10,5%, while retaining exhaust temperature at the same initial level (655 °C, compared to 660 °C).

5 CONCLUSIONS

Double injection strategies in terms of injection control parameters were tested and analysed against combustion dynamics and stability in idle operating conditions during the starting phase of the standardized driving cycle. Stationary test designed around the constant low engine thermal load was used to analyse possibilities to improve stability in conditions of late combustion used to increase exhaust temperature during engine and catalyst warm-up.

The research results and analysis were limited to gain information on capabilities of double injection strategies to improve combustion stability in idling warm-up conditions. The influence of valve timings, spark advance and emission results were not considered at this early stage and are part of the further optimization.

The sequence of variation tests was performed on the research single cylinder direct injection spark ignition engine on a constant engine load and speed corresponding to the idle operation. Full sweeps of four basic injection control parameters – start of injection (1^{st} and 2^{nd}), injected fuel mass split factor and fuel rail pressure were performed while maintaining constant engine load, speed, mixture strength, valve timings and spark advance. Combustion heat release rate was analysed using fast, simplified evaluation method based on Hohenberg approach. Combustion stability was evaluated upon covariance of indicated mean effective pressure, combustion duration and fuel mass fraction burned values (5,10,50 and 90%).

Significant improvement in terms of IMEP covariance was seen in case of SOI1 sweep. Shifting injection from -330 to -300 °CA improved homogenization and gave CoV_IMEP decrease from 15 to 10%, and a bit smaller decrease was also seen in case of CoV_MFB parameters. The exhaust temperature increased from 662 to 670 °C. Variation test of SOI2 provided small step in setup from initial -250 to optimal -235 °CA. The heat release rate hasn't changed significantly (MFB05-MFB50 remained unchanged), but combustion stability gained some improvement, particularly at the very start of combustion process (Cov_MFB05 and CoV_MFB10). Small decrease in exhaust gas flux was reported.

Fuel mass split factor variation test gained no particular improvement compared to initial setup (70-30). Increasing the fuel mass fraction of the second injection proved to be inefficient mainly due to compromised homogenization. Like the SOI2 sweep results, this is partially caused by the fact that spark advance remained constant throughout all tests and evaporation time was decreased gradually for each step-up in fuel mass introduced in second injection.

Fuel rail pressure sweep provided new setup which was expected upon theory of mixture formation. Compared to initial pressure of 50 bar, new setup at 110 bar gained improvement in terms of CoV_MFB parameters, again particularly for MFB05 and MFB10 while keeping exhaust temperature and CoV_IMEP unchanged.

REFERENCES

[1] Shelef, M. and Mccabe, R. W.: "Twenty-five years after introduction of automotive catalysts: what next?" Catal. Today 2000, 62, 35–50; doi:10.1016/S0920-5861(00)00407-7.

[2] Morra, E.P., Ellinger, R., Jones, S., Huss, A., Albrecht, R.: "Tank-To-Wheel CO2 Emissions Of Future C- Segment Vehicles." In: Liebl, J. (eds) Der Antrieb von morgen 2014. Proceedings. Springer Vieweg, Wiesbaden. https://doi.org/10.1007/978-3-658-23785-1_8

[3] Mock, P., Kühlwein, J., Tietge, U., Franco, V., Bandivadekar, A. and German, J.: "The WLTP: How a new test procedure for cars will affect fuel consumption values in the EU," 2014, doi: 10.1016/j.enpol.2013.12.013i.

[4] Hedinger, R., Elbert, P. and Onder, C.: "Optimal cold-start control of a gasoline engine," Oct. 01, 2017, MDPI. doi: 10.3390/en10101548.

[5] Lee, D.: "Effects of Secondary Air Injection During Cold Start of SI Engines", Ph.D. Thesis, Massachusetts Institute of Technology, Cambridge, MA, USA, 2010.

[6] Hallgren, B.E.: "Impact of Retarded Spark Timing on Engine Combustion, Hydrocarbon Emissions, and Fast Catalyst Light-Off", Ph.D. Thesis, Massachusetts Institute of Technology, Cambridge, MA, USA, 2005.

[7] Koehlen, C., Holder, E., Vent, G.: "Investigation of Post Oxidation and Its Dependency on Engine Combustion and Exhaust Manifold Design", SAE Tech. Pap. 2002, 7, 1–14.

[8] Schatz, A., Knorr, T., Ellmer, D.: "Elektrischer Heizkatalysator zur Optimierung der Emissionen von Mildhybridsystemen". MTZ-Motortech. Z. 2016, 77, 146–153.

[9] Pfahl, U., Schatz, A., Konieczny, R.: !Advanced Exhaust Gas Thermal Management for Lowest Tailpipe Emissions-Combining Low Emission Engine and Electrically Heated Catalyst", SAE Tech. Pap. 2012, 24,2924–2931.

[10] Randolph, A. L.: "Methods of Processing Cylinder-Pressure Transducer Signals to Maximize Data Accuracy," SAE Paper 900170, 1990.

[11] Brunt, M. F. J., Pond, C. R.: "Evaluation of Techniques for Absolute Cylinder Pressure Correction," SAE Paper 970036, 1997

[12] Hohenberg, G., Killman, I.: "Basic Findings from Measurement of the Combustion Process", XIX Fisita Congress, Melbourne, Australia, 1982, paper 82126

[13] Tomić, M. V., Popović, S. J., Miljić, N. L., Petrović, S. V., Cvetić, M. R., Knežević, D. M., & Jovanović, Z. S.: "A quick, simplified approach to the evaluation of combustion rate from an internal combustion engine indicator diagram", Thermal Science, Vol. 12, No. 1, 2008, pp. 85-102, (ISSN 0354-9836), https://doi.org/10.2298/TSCI0801085T

[14] Baumgarten, C.: "Mixture Formation in Internal Combustion Engines" (Ed. Heat and Mass Transfer), Springer Verlag 2006, ISBN-10 3540308350

[15] Stiesch, G.: "Modeling Engine Spray and Combustion Processes" (Ed. Heat and Mass Transfer), Springer Verlag 2003, ISBN 978-3-642-05629-1

MOBILITY & VEHICLE MECHANICS

https://doi.org/10.24874/mvm.2025.51.03.03
UDC: 621.43-233.18

ANALYSIS OF CRANKSHAFT TORSIONAL OSCILLATION DUMPER FOR ENGINE V-46-6

Marko Nenadović[1], Dragan Knežević[2], Željko Bulatović[3]*

Received in August 2024 *Accepted in October 2024*

RESEARCH ARTICLE

ABSTRACT: he crankshaft of an internal combustion engine represents an elastic system that is susceptible to deformations due to the effects of external forces and moments. The forces and the resulting torsional moments that stress the crankshaft during engine operation are periodic in nature, which causes torsional oscillations of the crankshaft. As a result of torsional oscillations, the crankshaft undergoes additional stresses. In some cases, these stresses can far exceed permissible values, which is why they must be checked during the engine design phase. Exceptionally intense torsional oscillations are particularly common in long shafts, as well as those shafts that are subjected to periodically varying torsional moments of extremely large amplitude. This paper will analyze the process of torsional oscillation of the crankshaft of a special-purpose engine, characterized by both of the mentioned parameters, which, among others, negatively affect the additional stresses on the crankshaft due to torsional oscillations. Additionally, the paper will analyze the methods by which it is possible to reduce the amplitudes of oscillations if necessary.

KEY WORDS: *Crankshaft, torsional oscillations, torsional vibration dumper*

[1]*Marko Nenadović, Military Technical Institute, Ratka Resanovica 1, Belgrade, Serbia, mare.nenadovic92@gmail.com, https://orcid.org/0009-0004-0172-3216, (*Corresponding author)*
2 Dragan Knežević, University of Belgrade Faculty of Mechanical Engineering Department of Internal Combustion Engines, Kraljice Marije 16 11000 Belgrade, Serbia, dknezevic@mas.bg.ac.rs , https://orcid.org/0000-0003-0403-3101
3 Željko Bulatović, Military Technical Institute, Ratka Resanovica 1, Belgrade, Serbia, zetonbulat@gmail.com, https://orcid.org/0009-0009-2339-1933

ANALIZA TORZIONOG OSCILACIONOG PRIGUŠAČA KOLENASTOG VRATILA ZA MOTOR V-46-6

REZIME: Radilica motora sa unutrašnjim sagorevanjem predstavlja elastični sistem koji je podložan deformacijama usled delovanja spoljašnjih sila i momenata. Sile i rezultujući torzioni momenti koji opterećuju radilicu tokom rada motora su periodične prirode, što uzrokuje torzione oscilacije radilice. Kao rezultat torzionih oscilacija, radilica je podvrgnuta dodatnim naprezanjima. U nekim slučajevima, ova naprezanja mogu daleko premašiti dozvoljene vrednosti, zbog čega se moraju proveriti tokom faze projektovanja motora. Izuzetno intenzivne torzione oscilacije su posebno česte kod dugih vratila, kao i kod onih vratila koja su izložena periodično promenljivim torzionim momentima izuzetno velike amplitude. U ovom radu će se analizirati proces torzionog oscilovanja radilice motora specijalne namene, koji karakterišu oba pomenuta parametra, a koji, između ostalog, negativno utiču na dodatna naprezanja na radilici usled torzionih oscilacija. Pored toga, u radu će se analizirati metode kojima je moguće smanjiti amplitude oscilacija ako je potrebno.

KLJUČNE REČI: *Radilica, torzione oscilacije, prigušivač torzionih vibracija*

ANALYSIS OF CRANKSHAFT TORSIONAL OSCILLATION DUMPER FOR ENGINE V-46-6

Marko Nenadović, Dragan Knežević , Željko Bulatović

INTRODUCTION

The crankshaft is one of the most structurally complex, heavily loaded, critical, and expensive components of an internal combustion engine, which is why special attention is given to its design. During engine operation, in addition to other forces, the crankshaft is subjected to periodically varying torsional moments, which, due to their periodic nature, lead to torsional oscillations of the crankshaft, causing additional stresses.

The crankshaft, like any other elastic element, has its own natural frequencies of oscillation. On the other hand, the torsional excitation moments that load the crankshaft, being periodic in nature, have their own frequency, which represents the excitation frequency and depends on the crankshaft's rotational speed. Consequently, it is possible that at a certain rotational speed, the excitation frequency may coincide with one of the natural frequencies of the crankshaft's oscillations, leading to resonant oscillations. During resonant oscillations, the oscillation amplitudes can increase drastically (compared to non-resonant regimes), causing the crankshaft's stresses to exceed permissible values, potentially leading to the failure of the crankshaft itself. Additionally, crankshaft operation at resonant regimes is accompanied by increased noise and unpleasant vibrations of the entire engine [1,2].

If the calculation of torsional oscillations reveals that the crankshaft stresses exceed permissible limits, certain measures must be taken to reduce these stresses to within acceptable values. To reduce stresses due to torsional oscillations, the rotational speeds at which the stresses caused by torsional oscillations are excessive can be marked on the tachometer, and these rotational speeds must be avoided during engine operation. This method of protecting the crankshaft from resonant oscillations is limited to applications where the engine can operate at a certain rotational speed for a very short time (e.g., only during acceleration), which is the case with marine engines, and therefore cannot be applied in other engine applications (e.g., vehicle engines). Additionally, to reduce stresses caused by torsional oscillations, certain design modifications can be made to the crankshaft itself, such as changing the moments of inertia and torsional stiffness, which leads to a change in the natural frequency of oscillation, and consequently a change in the amplitudes during resonant oscillation. This method of stress reduction is rarely used due to its complexity and extremely high material costs. The most commonly used method for reducing additional stresses due to torsional oscillation is the installation of torsional vibration dampers on the crankshaft itself. Installing a damper does not require any structural modifications to the engine, making this procedure cost-effective.

1 EQUIVALENT TORSIONAL OSCILLATORY SYSTEM

In real torsional oscillatory systems that contain elements of complex shapes, such as the torsional oscillatory system of an internal combustion engine, it is particularly challenging to perform any calculations. To facilitate the calculation, certain simplifications are introduced. All simplifications are based on replacing the real shapes of the shafts, which perform rotational movements, with light shafts (of negligible mass) with specific torsional stiffness and concentrated masses with certain moments of inertia. The values of the torsional stiffness of the light shafts and the moments of inertia of the concentrated masses

are determined based on the condition of equality of the kinetic and potential energy of the real and simplified oscillatory system. From the condition of energy equality between the real and simplified system, it follows that the concentrated masses of the simplified system must have the same moments of inertia, while the light shafts must have the same torsional stiffness as the parts of the real system they represent. The simplified oscillatory system thus obtained is called an equivalent torsional oscillatory system [2,3,4].

When the internal combustion engine is considered as a torsional oscillatory system or part of a more complex oscillatory system (engine and transmission), practical reasons lead to focusing on the crankshaft, which, due to its specific geometry and constant excitation during operation, is the main source of torsional oscillations. The other subsystems of the engine are then reduced relative to the crankshaft, adhering to the aforementioned condition of energy equality between the real and equivalent torsional oscillatory system [2].

The moments of inertia of the concentrated masses, as well as the torsional stiffness of the sections (light shafts, ls at Figure 1) of the equivalent torsional oscillatory system engine-dynamometer, for the "V-46-6" engine, which is the subject of this study, are shown in Table 1. The procedure for determining these parameters is described in detail in reference [2]. The appearance of such an equivalent torsional oscillatory system can be seen in Figure 1, while the real torsional oscillatory system can be seen in Figure 2.

In addition to the moments of inertia of the concentrated masses and the torsional stiffness of individual sections, for the complete definition of the equivalent torsional oscillatory system, it is necessary to determine the damping (internal and external), as well as the excitation torsional moments that load the crankshaft.

Due to the small number of studies addressing the issue of damping in the torsional oscillatory system of an engine, determining the damping represents the most complex part of defining the equivalent torsional oscillatory system. Here, the damping was calculated according to recommendations found in literature from Eastern countries. The damping thus calculated is external by its nature, taking into account the influence of internal damping in the material.

Table 1. Parameters of the equivalent torsional oscillatory system [2]

	Moment of inertia **J** (kgm^2)	Torsional stiffness ***c*** (Nm/rad)	Dumping coefficient **k** (Nms/rad)
Mass 1	0.010441		0
Light shaft 1		2.074×10^6	
Mass 2	0.172104		8.1518
Light shaft 2		2.188×10^6	
Mass 3	0.171664		8.1518
Light shaft 3		2.188×10^6	
Mass 4	0.171664		8.1518
Light shaft 4		2.188×10^6	
Mass 5	0.171664		8.1518
Light shaft 5		2.188×10^6	

Mass 6	0.171664		8.1518
Light shaft 6		2.188 x 10^6	
Mass 7	0.171664		8.1518
Light shaft 7		8.885 x 10^6	
Mass 8	0.278054		0
Light shaft 8		90000	
Mass 9	1.755389		0

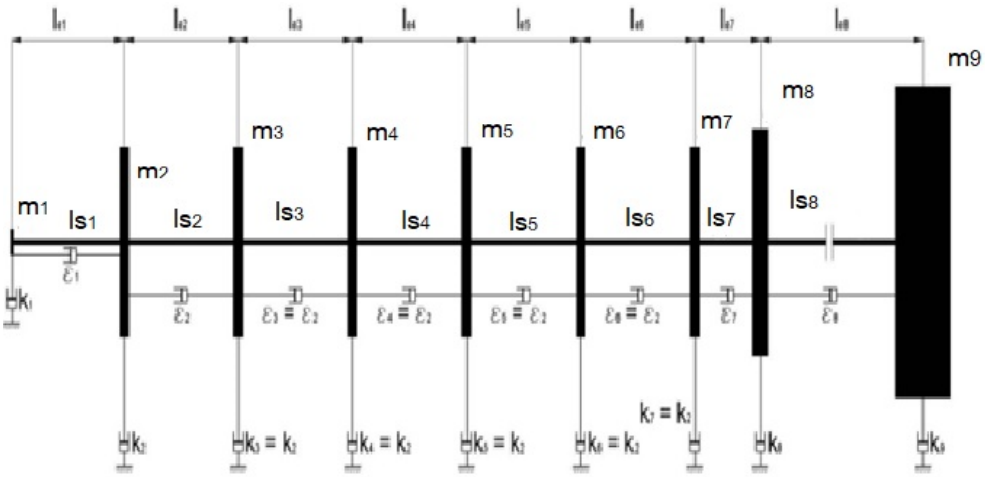

Figure 1 Equivalent torsional oscillatory system engine-dynamometer [2]

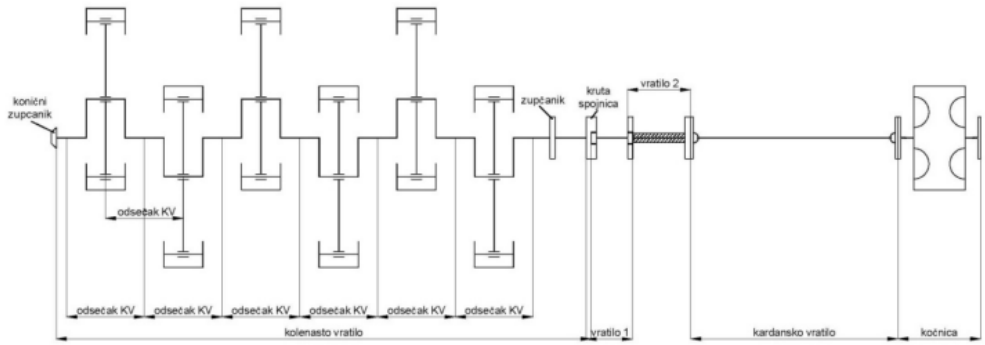

Figure 2 Real torsional oscillatory system [2]

The excitation moments that load the crankshaft are the result of the action of gas forces and the forces of inertia of the linearly oscillating masses. The inertia forces of the rotating masses do not affect torsional oscillations.

To determine the excitation moment, it is necessary to know the pressure curve in the engine cylinder as a function of the crankshaft angle [5]. By indicating the pressure in the first left and third right cylinders, for the regime of maximum torque, the pressure curves as a function of the rotation angle were obtained and are shown in Figure 3.

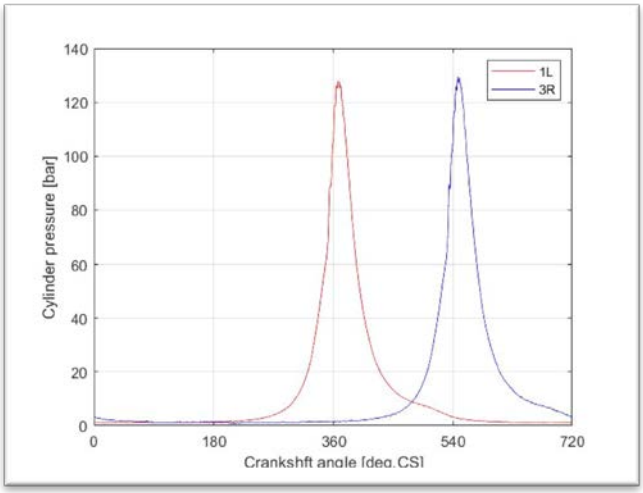

Figure 3 Pressure curve in the first left and third right cylinders as a function of the crankshaft rotation angle

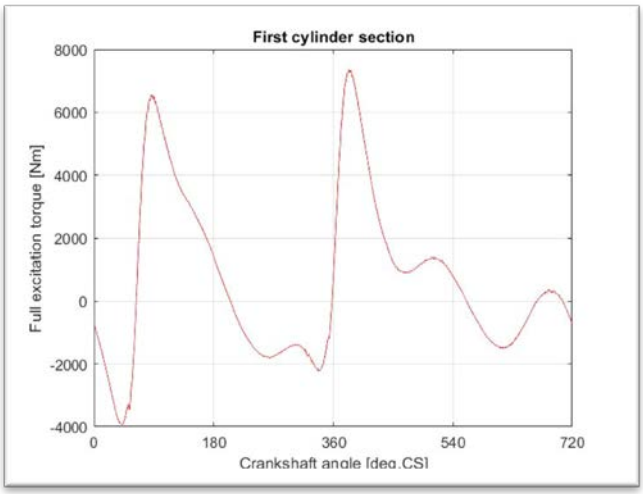

Figure 4 Total excitation moment curve as a function of the crankshaft angle, at 2000 rpm

When the pressure curves in the cylinder are known, along with the kinematic parameters and masses of the piston mechanism, the total excitation torsional moment (combined effect of the gas force moment and the inertial force moment of the linearly oscillating masses) can be easily obtained. It should be noted that the decomposition of forces in the piston mechanism, for the engine in question, cannot be performed in the same way for the cylinders in the left and right banks. This is because the piston mechanism of one section (opposite cylinders in different banks) of the cylinders is designed with a main (left bank) and an auxiliary connecting rod (right bank), known as a compound piston mechanism. A detailed description of the procedure for decomposing the forces of the compound piston mechanism can be found in reference [2,3]. By applying this procedure, the total excitation moment curve as a function of the crankshaft rotation angle for the first cylinder section was obtained, and it is shown in Figure 4. Assuming that the working cycles in each left and each right cylinder are identical, the excitation moments in the other cylinder sections are

identical to those in the first section but phase-shifted by the firing angle between the specific section and the first section.

The analysis of torsional oscillations of the crankshaft with excitation as shown in Figure 4 is extremely complex because the total excitation moment is not a simple harmonic function of the crankshaft rotation angle. Therefore, to simplify the calculation, the total excitation moment is expanded into a Fourier trigonometric series. By expanding the total excitation moment into a Fourier series, the excitation moment is obtained as the sum of simple harmonic functions, which significantly simplifies the calculation [6]. In the calculation, each harmonic of the excitation moment must be analyzed individually, and after such an analysis, the cumulative effect of all harmonics may occur. The expansion of a function defined at discrete points, such as the excitation moment function, into a Fourier series is described in references [2,3]. In Figure 5, the amplitude of each harmonic of the Fourier series for the defined excitation moment can be seen.

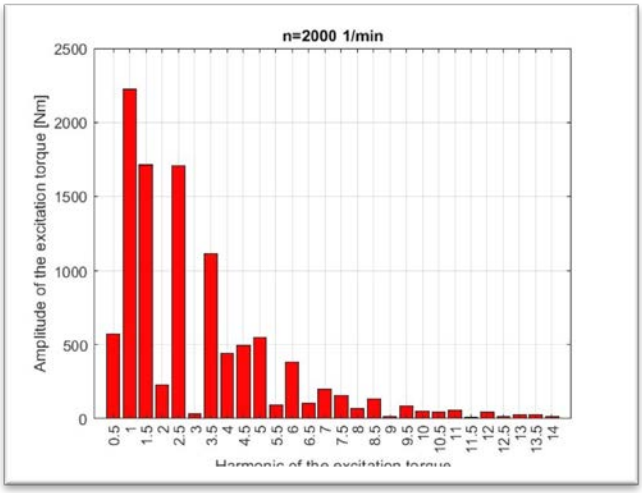

Figure 5 Amplitudes of all harmonics of the total excitation moment

2 NATURAL FREQUENCIES OF OSCILLATION

The natural frequencies of oscillation of the equivalent torsional oscillatory system of an internal combustion engine are determined under the assumption that the oscillations are free and undamped, meaning that the effects of damping and excitation moments on the oscillation process are neglected. This assumption has proven to be entirely justified in systems where there is no significantly large source of damping [7].

For oscillatory systems with more than two degrees of freedom, as is the case here, it is quite complicated to analytically determine the natural frequencies of oscillation. Therefore, in such systems, the natural frequencies of oscillation are typically determined numerically, with Holzer numerical method being the most commonly used. A detailed description of the application of Holzer numerical method is provided in references [2,3].

By applying Holzer method to the equivalent torsional oscillatory system from this study, the following values were obtained for the first three natural frequencies: 337.67 Hz – first natural frequency, 1541.6 Hz – second natural frequency, 3145.91 Hz – third natural frequency. Holzer method can also be used to determine the other natural frequencies (in

this particular case, there are eight in total), but they are not of interest for analysis as they have high values, and the system will never be in resonance at their oscillation modes. The relative amplitudes for the first three modes of oscillation are shown in Figures 6, 7, and 8.

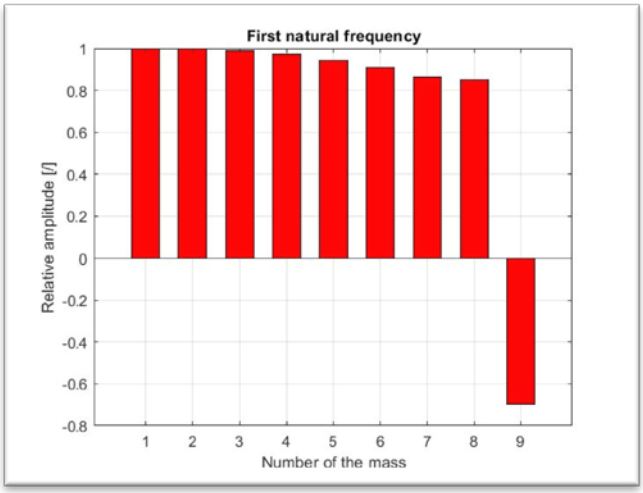

Figure 6 Relative amplitudes for the first mode of oscillation

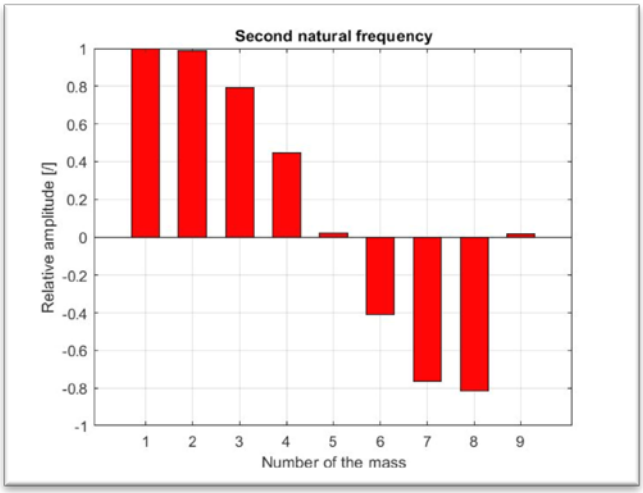

Figure 7 Relative amplitudes for the second mode of oscillation

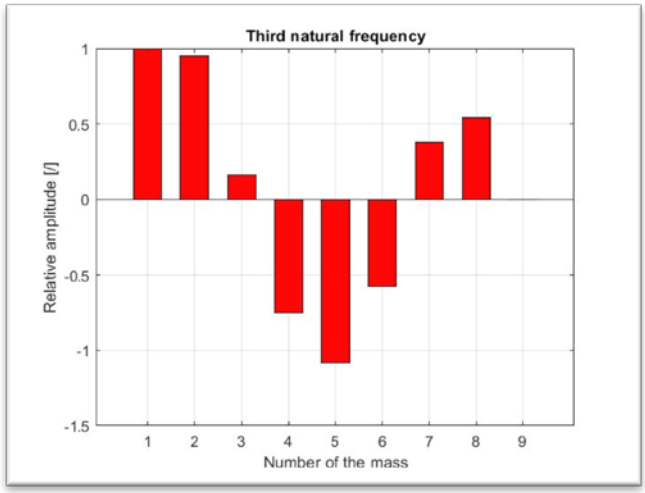

Figure 8 Relative amplitudes for the third mode of oscillation

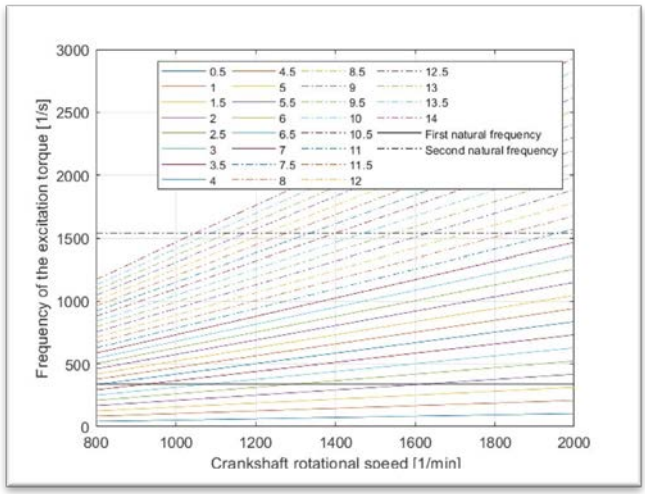

Figure 9 Campbell diagram

Once the natural frequencies of oscillation are known, it is easy to determine the critical rotational speeds (the rotational speeds at which one of the excitation harmonics is resonant). A graphical representation of the critical rotational speeds is provided in the so-called Campbell diagram, which is shown in Figure 9.

3 AMPLITUDES AND ADDITIONAL STRESSES DUE TO TORSIONAL OSCILLATIONS

The amplitudes of all masses in the equivalent torsional oscillatory system are determined by solving a system of differential equations, which is obtained by applying LaGrange equations of the second order for each concentrated mass of the system [4]. The resulting system of differential equations needs to be solved for each harmonic of the excitation moment, at every rotational speed within the operational range. The procedure for solving such a system of differential equations can be found in references [2,3]. By applying such a

mathematical model, the amplitudes of each mass and the stresses in each section as a function of engine speed were obtained, as shown in Figures 10 and 11.

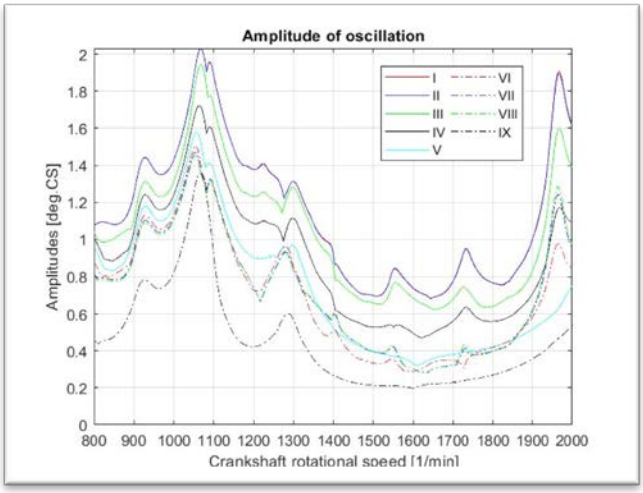

Figure 10 Amplitudes of all masses as a function of engine speed

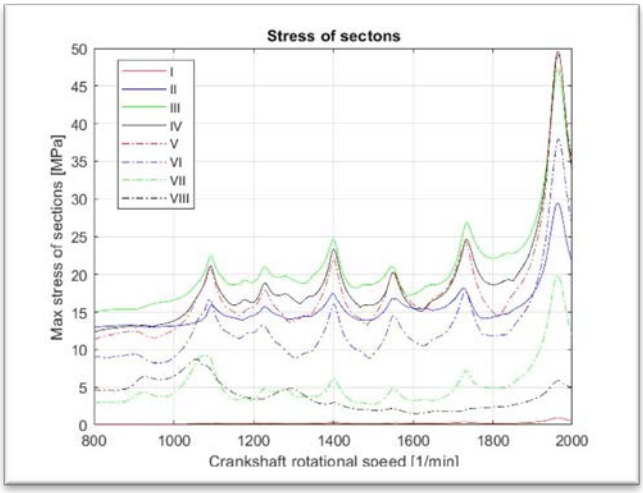

Figure 11 Stresses in sections as a function of engine speed

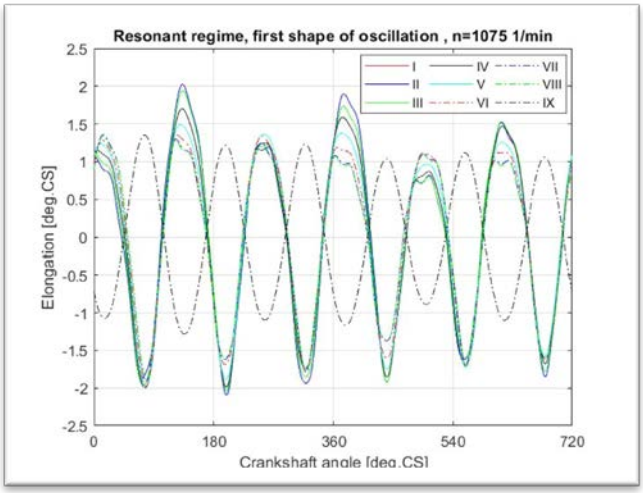

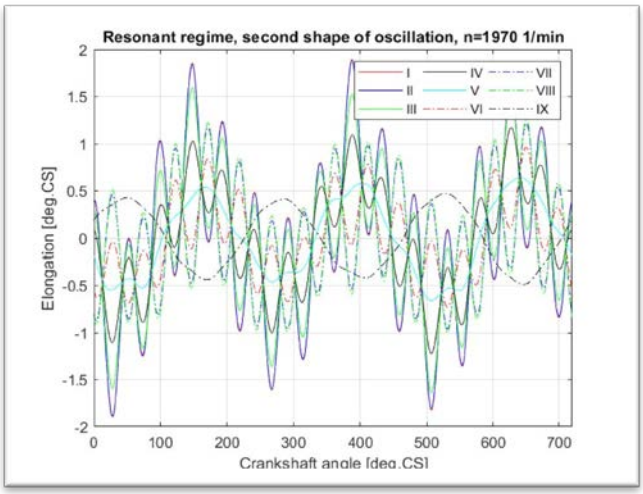

Figure 12 Oscillation flow at 1075 rpm *Figure 13 Oscillation flow at 1970 rpm*

Figures 12 and 13 show the oscillation flows of each concentrated mass at the rotational speed where the oscillation amplitude, or additional stress, has a maximum value. The maximum oscillation amplitude occurs in the first concentrated mass (conical gear for driving auxiliary devices) of the equivalent system at 1075 rpm. Figure 12 clearly shows that at this speed, the crankshaft oscillates according to the first mode of oscillation.

From Figure 13, it is not possible to reliably determine the mode of oscillation of the crankshaft at 1970 rpm, even though the excitation harmonic of order 7 ½ is resonant at this speed in the second mode of oscillation. This can be explained by the fact that at a slightly higher speed of over 2000 rpm, the 1 ½ harmonic is resonant in the first mode of oscillation, which influences the oscillation pattern at 1970 rpm. Since the 1 ½ and 7 ½ harmonics are not resonant in the same mode of oscillation, the mode of oscillation at 1970 rpm due to all the excitation harmonics is not clearly defined.

In the “V-46-6” engine, almost every resonant regime in the first mode of oscillation is accompanied by an excitation harmonic that is resonant in the second mode of oscillation at

nearly the same speed (see Campbell diagram). As a result, the oscillation amplitudes due to the effect of all the excitation harmonics are significantly higher than the amplitudes obtained only from the resonant harmonic at the given critical speed. Figures 14 and 15 show the amplitudes of the concentrated masses due solely to the effect of the 3rd harmonic and the 7 ½ harmonic, respectively.

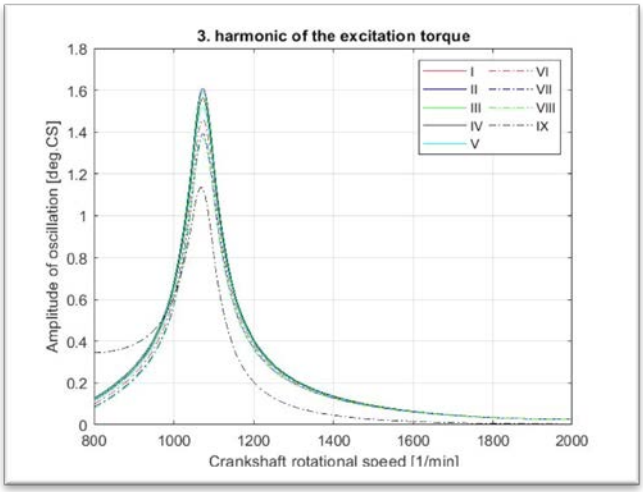

Figure 14 Amplitudes of all system masses as a function of speed due to effect of the 3rd excitation harmonic

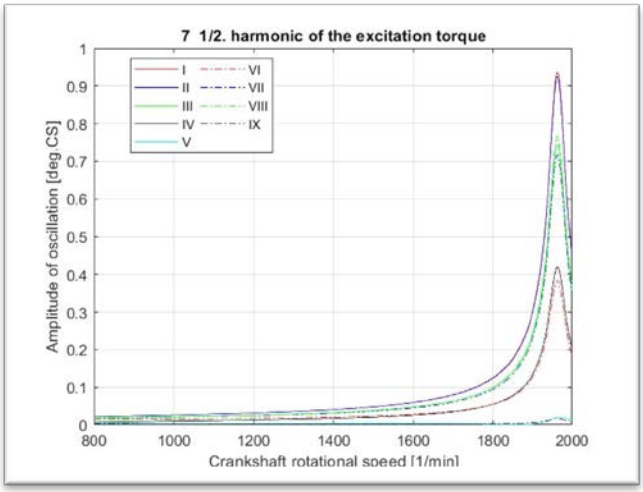

Figure 15 Amplitudes of all system masses as a function of speed due to the effect of the 7 ½ excitation harmonic

By comparing the amplitude values obtained solely from the resonant harmonics with those obtained from the effect of all the excitation harmonics, it can be stated that the assertion about the necessity of analyzing torsional oscillations due to all excitation harmonics, in order to obtain a more realistic picture of additional stresses, presented in references [1, 2] is fully justified. For example, the oscillation amplitude of the first mass, due to the effect of all excitation harmonics, is nearly 100% higher at 1970 rpm than that obtained from analyzing only the resonant harmonic at the given speed.

Regarding the additional stresses, they are highest at 1970 rpm, where they exceed the permissible 40 MPa. Therefore, it is necessary to take certain measures to reduce them to acceptable levels. In addition to the high stresses, the exceptionally high oscillation amplitude of the first mass (the bevel gear for driving the engine's auxiliary devices) throughout the engine's operating range also poses a problem. This is a particular issue because the conical gear also drives the engine timing mechanism, which disrupts the working fluid exchange process, leading to power loss and reduced engine efficiency. Since the engine in question uses a conventional injection system (pump-pipe-nozzle), these large amplitudes also negatively affect the fuel injection process, as the high-pressure pump is driven by a crankshaft that is oscillating intensely. Due to all these reasons, it is necessary to reduce the level of torsional oscillations in the system, which will be achieved here by applying torsional vibration dampers.

4 TORSIONAL VIBRATION DAMPER

In this study, the simplest model of a torsional vibration damper will be used. This model consists of one concentrated mass representing the entire engine and another concentrated mass representing the inertial mass of the torsional vibration damper. These two concentrated masses are connected by a section with appropriate stiffness, where the internal damping of that section must be considered in the analysis of the torsional damper. The described model of the torsional vibration damper can be seen in Figure 16. In defining this model, the nine masses of the equivalent torsional oscillatory system were reduced to one. In this reduction process, it is necessary to respect the condition of the equality of kinetic and potential energy between the initial system (with nine masses) and the final system (one mass). Although at first glance, representing the entire torsional oscillatory system with only one concentrated mass seems like an extreme simplification, reference [11] shows that applying such a model yields satisfactory results.

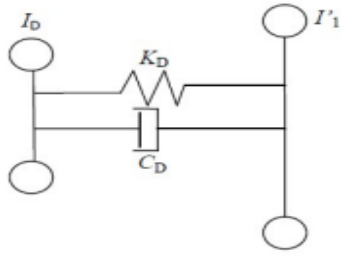

Figure 16 Simple model of a torsional vibration damper [11]

For the system shown in Figure 16, the following two differential equations can be written [11]:

$$\theta_1\ddot{\vartheta}_1 + c_1\vartheta_1 - c_2(\vartheta_2 - \vartheta_1) - b\left(\dot{\vartheta}_2 - \dot{\vartheta}_1\right) = M_1\cos(\Omega t), \quad (1)$$

$$\theta_2\ddot{\vartheta}_2 + c_2(\vartheta_2 - \vartheta_1) + b\left(\dot{\vartheta}_2 - \dot{\vartheta}_1\right) = 0, \quad (2)$$

where: θ_1 – moment of inertia of the engine [kgm²], θ_2 – moment of inertia of the damper mass [kgm²], c_2 – torsional stiffness of the section between the engine and the damper mass [Nm/rad], b – internal damping coefficient of the section [Nms/rad], ϑ_1 – angular displacement of the engine mass [°], M_1 – amplitude of the excitation moment [Nm], Ω – frequency of the excitation moment [1/s].

It should be noted here that the torsional stiffness c_1 is determined based on the condition that the natural frequency of oscillation of the mass representing the engine is equal to the excitation frequency of the resonant harmonic at the critical rotational speed.

The solutions to the system of differential equations (1) and (2) are assumed, according to the theory of linear differential equations, to be of the form:

$$\vartheta_i = X_i\, cos(\Omega t) + Y_i\, sin(\Omega t), \tag{3}$$

When the assumed solution (3) is substituted into equations (1) and (2), a system of four algebraic equations with four unknowns is obtained. This system, in which the unknowns are the oscillation amplitudes of both masses, can be solved using the determinant method. Solving this system yields the following relation for the dynamic amplification factor of the first mass (engine mass):

$$\eta_d = \frac{4\beta^2\psi_1^2+\left(\psi_1^2-\gamma^2\right)^2}{4\beta^2\psi_1^2\left(\psi_1^2-1+\mu\psi_1^2\right)^2+\left[\mu\psi_1^2\gamma^2-\left(\psi_1^2-1\right)\left(\psi_1^2-\gamma^2\right)\right]^2} = \frac{M\beta^2+N}{P\beta^2+Q}, \tag{4}$$

where: $\beta = b/2\theta_2\omega_{11}$ – dimensionless damping coefficient [/], ω_{11} – natural frequency of oscillation of the engine mass [1/s], $\mu = \theta_2/\theta_1$, $\gamma = \omega_{22}/\omega_{11}$, ω_{22} – natural frequency of oscillation of the damper mass [1/s].

For the dynamic amplification factor of the engine mass, expressed by relation (4), to be independent of the damping value, it is necessary for the determinant of the quantities M , N , P , and Q to be equal to zero, i.e., the condition MQ – PN = 0 must be satisfied. Based on this condition, the following biquadratic equation is obtained:

$$\psi_1^4 - 2\frac{1+(1+\mu)\gamma^2}{2+\mu}\psi_1^2 + \frac{2\gamma^2}{2+\mu} = 0, \tag{5}$$

Solving the biquadratic equation (5) yields two values of ψ_1^2 for which the dynamic amplification factor of the engine mass is independent of the internal damping of the section between the engine mass and the damper mass. If it is assumed that the damping is $\beta = \infty$, the two values of ψ_1^2 obtained by solving the biquadratic equation (5) give the following values for the dynamic amplification factor of the engine mass:

$$\eta_{d1}^{(1)} = \frac{1}{\left|1-(1+\mu)\frac{\Omega_1^2}{\omega_{11}}\right|}$$
$$,\eta_{d1}^{(2)} = \frac{1}{\left|1-(1+\mu)\frac{\Omega_2^2}{\omega_{11}}\right|}, \tag{6}$$

It has been shown in references [4,5] that the best value for the dynamic amplification factor of the engine mass is achieved when both dynamic factors in (6) have the same value. By equating them, the most favorable ratio of the natural frequencies of the damper mass and the engine mass can be determined, which should be used in the design of the torsional vibration damper. The most favorable ratio of natural frequencies is:

$$\gamma_{opt} = \frac{\omega_{22}}{\omega_{11}} = \frac{1}{1+\mu}, \tag{7}$$

When the optimal value of the ratio of the natural frequencies of the damper mass and the engine mass, determined by relation (7), is substituted into the expression for the dynamic amplification factor of the engine mass (4), and the first derivative of the resulting function with respect to the variable β^2 is set to zero, two values of the dimensionless damping

coefficient are obtained at which the dynamic amplification factor of the engine mass reaches its maximum value. These two values of the dimensionless damping coefficient are:

$$\beta_{(1)}^2 = \frac{\mu\left(3-\sqrt{\frac{\mu}{\mu+2}}\right)}{8(1+\mu)},$$
$$\beta_{(2)}^2 = \frac{\mu\left(3+\sqrt{\frac{\mu}{\mu+2}}\right)}{8(1+\mu)}, \quad (8)$$

It is recommended, as can be found in reference [4], that the value of the internal damping of the torsional vibration damper be taken as the average value from (8), so the optimal value of the dimensionless internal damping coefficient of the torsional damper is:

$$\beta_{opt}^2 = \frac{3\mu}{8(1+\mu)}, \quad (9)$$

By applying the torsional vibration damper for the crankshaft described here, it is possible to reduce the oscillation amplitudes only at a specific oscillation frequency (at one critical speed). This is because the entire equivalent torsional oscillatory system of the engine is represented by only one concentrated mass, so such a system has only one degree of freedom (one natural frequency). Therefore, the damper is designed to reduce the amplitude of oscillations as much as possible during resonant oscillation (one resonant regime due to one degree of freedom). Since the real torsional oscillatory system of an internal combustion engine is a system with multiple degrees of freedom, and thus has several natural frequencies of oscillation, the damping of torsional oscillations is usually chosen to be applied at the resonant regime where the oscillation amplitudes have the maximum value. It is expected that due to the extremely high damping in the damper itself, the amplitudes at other resonant regimes will also be lower than in the case when there is no torsional damper. If this is not the case, it is necessary to apply another model for calculating the torsional vibration damper for the crankshaft.

The moment of inertia of the concentrated mass representing the effect of the entire engine, respecting the principle of energy equality, is obtained as the sum of the moments of inertia of all masses in the equivalent torsional oscillatory system without the torsional vibration damper. The natural frequency of the system with one mass is equal to the frequency of the resonant harmonic at the speed where the oscillation amplitudes have the maximum value, in this case, the 3rd harmonic at 1075 rpm. With such a defined system, where the entire engine is represented by one concentrated mass, and by applying the described torsional damper model, Figures 17 and 18 show the effect of the damper on the dynamic amplification factor of the engine mass, as well as the damper mass.

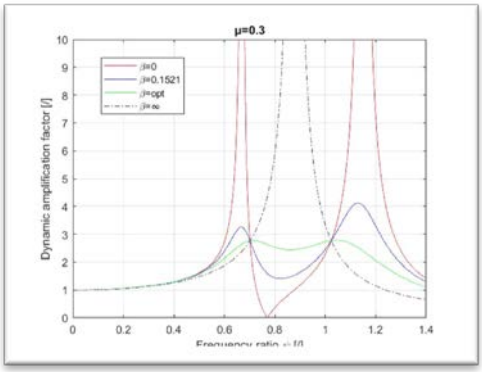

Figure 17 Dynamic amplification factor of the engine mass as a function of the frequency ratio for the given mass ratio

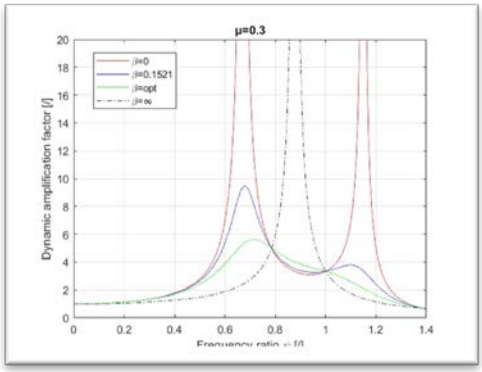

Figure 18 Dynamic amplification factor of the dumper mass as a function of the frequency ratio for the given mass ratio

From the above figures, it is clearly visible that there are two frequency ratios (the ratio of the excitation frequency to the natural frequency of the engine mass) at which the dynamic amplification factor is independent of damping. These are the two points on the diagrams where all the curves representing different values of the dimensionless damping coefficient intersect. It can also be observed that the dynamic amplification factor is smallest when the damping in the damper is optimal.

By applying the described model of the torsional vibration damper, diagrams like those shown in Figures 19, 20, and 21 can be generated for different values of the mass ratio, i.e., the moments of inertia of the damper and the engine. Based on these diagrams, certain conclusions can be drawn regarding the design of the torsional vibration damper. From the diagram in Figure 19, it is clear that as the moment of inertia of the damper mass increases, with the engine's moment of inertia considered constant, the dynamic amplification factor of the engine mass decreases, meaning the oscillation amplitudes will be smaller, provided the damping is at an optimal level. On the other hand, optimal damping increases with the increase in the moment of inertia of the damper mass (Figure 20), while the difference between the dynamic amplification factors of the damper mass and the engine mass decreases with the increase in the moment of inertia of the damper mass (Figure 21). Based on the above, it is concluded that to achieve the greatest possible reduction in oscillation amplitudes, it is necessary for the moment of inertia of the damper to be as large as possible. Additionally, the stresses on the damper's damping element will be lower as the moment of inertia of the damper mass increases, due to the smaller difference in the dynamic amplification factors of the two masses (Figure 21). However, the moment of inertia of the damper mass cannot be arbitrarily large. The increase in moment of inertia is achieved either by increasing the mass or the diameter of an element. In this specific case, increasing the mass of the damper's inertial mass would lead to additional bending stresses on the crankshaft, which is not problematic because the crankshaft endures much higher stresses during operation. On the other hand, increasing the diameter of the damper's inertial mass is limited by the available space in the engine compartment. Furthermore, a large moment of inertia of the damper mass requires higher optimal damping, which complicates and increases the cost of constructing the damping element itself. Due to all of the above, the design of the torsional vibration damper must be a compromise between opposing requirements.

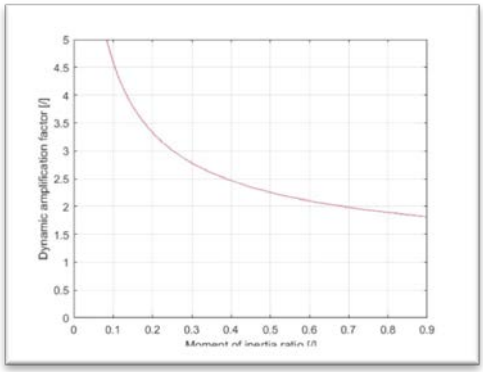

Figure 19 Dependence of the dynamic amplification factor of the engine mass on the ratio of moments of inertia

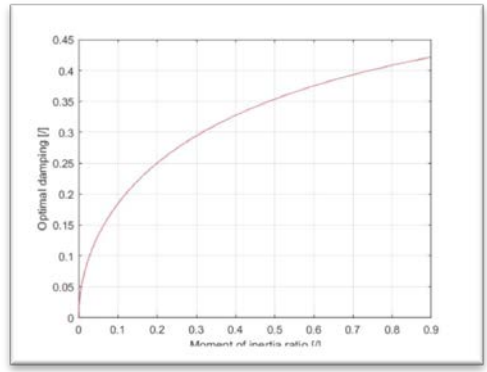

Figure 20 Dependence of optimal damping in the dumper on the ratio of moments of inertia

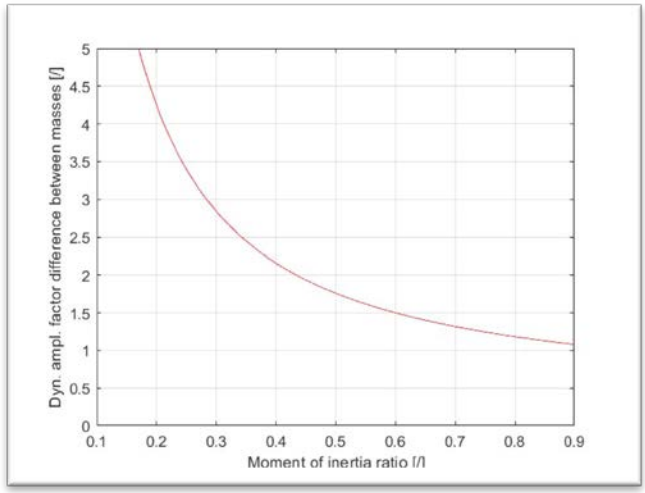

Figure 21 Difference in dynamic amplification factors between the engine mass and the damper mass as a function of the ratio of moments of inertia

For the engine that is the subject of this study, it was decided that the ratio of the moments of inertia of the damper mass and the engine would be 0.3. With this selected ratio of moments of inertia, the optimal damping coefficient of the damping element of the torsional damper was determined using formula (9). After defining the ratio of moments of inertia and the optimal damping coefficient, it is necessary to perform the calculation of torsional oscillations on the new equivalent torsional oscillatory system (with the damper), which now has one additional concentrated mass (the damper mass) and one additional section (the damper's damping element). The resulting amplitudes of all masses and stresses in all sections of such an equivalent torsional oscillatory system are shown in Figures 22 and 23.

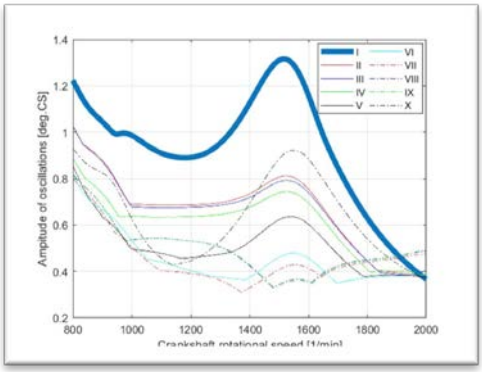

Figure 22 Oscillation amplitudes of the oscillatory system with the damper as a function of engine speed

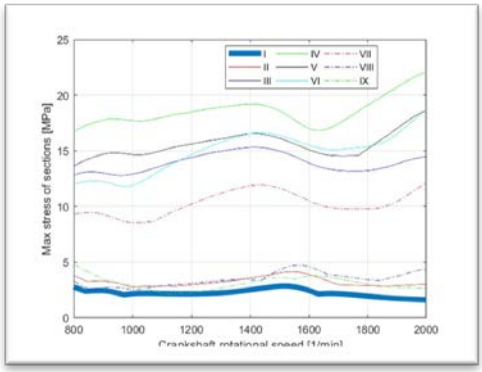

Figure 23 Stresses in sections of the oscillatory system with the dumper as a function of engine speed

5 CONCLUSION

Based on the conducted calculation of the torsional oscillations of the crankshaft of the "V-46-6" engine, which does not have a torsional vibration damper, it has been determined that the oscillation amplitudes are extremely large, even exceeding 2° in some regimes (Figure 10). Such high values of oscillation amplitudes inevitably lead to increased vibrations of the entire engine, and additionally, the supplementary stresses on the crankshaft due to torsional oscillations are above the permissible limit (Figure 11). Besides the purely mechanical problems resulting from the torsional oscillations of the crankshaft, they also cause certain issues that affect the engine's working cycle. Given that the amplitude of the mass representing the auxiliary drive is extremely large, it is likely that the process of timely opening and closing of the valves, i.e., the working fluid exchange process, is compromised. As a result, the engine's power is reduced, and its efficiency worsens. Additionally, due to the large oscillation amplitudes, the fuel injection process becomes deregulated because the high-pressure pump is driven by the crankshaft. This fact also leads to a decrease in power and a deterioration in efficiency. To mitigate all the aforementioned negative consequences of the intense torsional oscillations of the crankshaft as much as possible, it was decided to install a torsional vibration damper on the crankshaft.

The described model of the torsional vibration damper is the simplest model, assuming that the damping element has a linear characteristic, i.e., that its torsional stiffness and damping coefficient are constant values. This assumption is rather crude and does not correspond to the real oscillation process because both torsional stiffness and damping coefficient are variables that depend on the oscillation angle (in dampers with a rubber damping element, which are most commonly used).

The installation of the torsional vibration damper according to the described model successfully reduced both the amplitudes and the stresses on the crankshaft. However, due to the assumption of the torsional vibration damper as a linear element, the obtained results need to be experimentally verified. Despite this, the results presented here provide a good starting point for the design of a torsional vibration damper.

REFERENCES

[1] Suryanarayana, A.: "Engine Dynamics and Torsion Vibration Reduction", Master Thesis, Chalmers University of Technology, Gothenburg, Sweden, 2015

[2] Bulatovic Z.: „Parameter Identification of Equivalent Dynamic-Torsional System of Diesel Engine Crankshaft Based on Variable Engine Speed", Doctoral Dissertation, Faculty of Mechanical Engineering, Belgrade, 2015. (In Serbian)

[3] Nenadovic M.: „Analysis of Engine Crankshaft Torsional Oscillation", Master Thesis, Faculty of Mechanical Engineering, Belgrade, 2023. (In Serbian)

[4] Milasinovic A.: "Influence of Reciprocating Masses of Piston Mechanism on Crankshaft Torsional Oscillation", Master Thesis, Faculty of Mechanical Engineering, Banja Luka, 2001. (In Serbian)

[5] Bulatovic Z., Knezevic D.: „Current Engine Speed as Diagnostic and Control Parameter of Engine Operation", Research and Designing for the Economy 14/2006. (In Serbian)

[6] Raskovic D., Thoery of Oscillation, Construction Book, Belgrade, 1974. (In Serbian)

[7] Trifkovic D., Research of Torsional Oscillation in Transmission Power System from Marine Diesel Engine to Propeller, Master Thesis, Faculty of Mechanical Engineering, Belgrade, 2004. (In Serbian)

[8] Miljic N., Optimum Ignition Timing Control of SI Engine Using Artificial Neural Networks, Doctoral Dissertation, Faculty of Mechanical Engineering, Belgrade, 2012. (In Serbian)

[9] Popovic S., Research and Development Instantaneous Crankshaft Angular Speed Based Method for Engine Combustion Analysis, Doctoral Dissertation, Faculty of Mechanical Engineering, Belgrade, 2013. (In Serbian)

[10] Filipovic I., Internal Combustion Engines-Dynamics and Oscillations, Faculty of Mechanical Engineering, Sarajevo, 2007. (In Serbian)

[11] Lin Deng, Junfeng Zhang, Lijun Xiang, Design Torsional Vibration Dumper of Engine Based on Classical Optimal Approach, IOP Conference Series: Materials, Science and Engineering, 2018.

Intentionally blank

MOBILITY & VEHICLE MECHANICS

https://doi.org/10.24874/mvm.2025.51.03.04
UDC: 528.7:621.7

ANALYSIS OF PHOTOGRAMMETRY APPLICATION POSSIBILITIES FOR REVERSE ENGINEERING OF COMPONENTS IN THE AUTO INDUSTRY

Marko Delić[1], Vesna Mandić[2], Dragan Adamović[3], Dušan Arsić[4], Đorđe Ivković[5], Nada Ratković[6]*

Received in August 2024 *Accepted in October 2024*

RESEARCH ARTICLE

ABSTRACT: Reverse engineering is a technique that has recently been used in all areas of industry. The application of reverse engineering in the auto industry occupies a very important place. 3D scanners are often used to digitize parts with fine details or large sheet metal, and they can be very expensive. In this paper, the possibility of using photogrammetry for reverse engineering of components in the auto industry will be analyzed. Digitization of the automotive component will be done in two ways, using a mobile phone camera and free photogrammetry software and a suitable professional scanner. The accuracy of the cloud of points obtained and time required for digitization by both methods will be compared. At the end conclusion will be drawn whether it is currently possible to use photogrammetry in industrial conditions.

KEY WORDS: *3D scanning, photogrammetry, reverse engineering, point cloud*

[1]*Marko Delić, Faculty of Engineering, University of Kragujevac, Sestre Janjić 6, Kragujevac, Serbia, marko.delic@kg.ac.rs, https://orcid.org/0009-0004-0172-3216, (*Corresponding author)*
[2] *Vesna Mandić, Faculty of Engineering, University of Kragujevac, Sestre Janjić 6, Kragujevac, Serbia, mandic@kg.ac.rs, https://orcid.org/0000-0003-1624-3536*
[3] *Dragan Adamović, Faculty of Engineering, University of Kragujevac, Sestre Janjić 6, Kragujevac, Serbia, https://orcid.org/0000-0003-3459-3011*
[4] *Dušan Arsić, Faculty of Engineering, University of Kragujevac, Sestre Janjić 6, Kragujevac, Serbia, dusan.arsic@fink.rs, https://orcid.org/0000-0003-0326-0898*
[5] *Đorđe Ivković, Faculty of Engineering, University of Kragujevac, Sestre Janjić 6, Kragujevac, Serbia, djordje.ivkovic@fink.rs, https://orcid.org/0000-0002-5747-7876*
[6] *Nada Ratković, Faculty of Engineering, University of Kragujevac, Sestre Janjić 6, Kragujevac, Serbia, nratkovic@kg.ac.rs, https://orcid.org/0000-0003-1446-8678*

ANALIZA MOGUĆNOSTI PRIMENE FOTOGRAMETRIJE ZA RENVERZNI INŽENJERING KOMPONENTI U AUTOMOBILSKOJ INDUSTRIJI

REZIME: Reverzni inženjering je tehnika koja se u poslednje vreme koristi u svim oblastima industrije. Primena reverznog inženjeringa u automobilskoj industriji zauzima veoma važno mesto. 3D skeneri se često koriste za digitalizaciju delova sa finim detaljima ili velikim limovima, i mogu biti veoma skupi. U ovom radu biće analizirana mogućnost korišćenja fotogrametrije za reverzni inženjering komponenti u automobilskoj industriji. Digitalizacija automobilske komponente će se vršiti na dva načina, korišćenjem kamere mobilnog telefona i besplatnog softvera za fotogrametiju i odgovarajućeg profesionalnog skenera. Uporediće se tačnost dobijenog oblaka tačaka i vreme potrebno za digitalizaciju obe metode. Na kraju će biti izveden zaključak da li je trenutno moguće koristiti fotogrametriju u industrijskim uslovima.

KLJUČNE REČI: *3D skeniranje, fotogrametrija, reverzni inženjering, oblak tačaka*

ANALYSIS OF PHOTOGRAMMETRY APPLICATION POSSIBILITIES FOR REVERSE ENGINEERING OF COMPONENTS IN THE AUTO INDUSTRY

Marko Delić, Vesna Mandić, Dragan Adamović, Dušan Arsić, Đorđe Ivković, Nada Ratković

INTRODUCTION

Photogrammetry is an optical method of 3D digitization. The name comes from the Latin words fotos (light), gramma (writing, recording) and meteo (measurement). The first application of photogrammetry is related to the middle of the 19th century when Aimé Laussedat made topographic maps based on images created from the ground. With the development of the technique, new methods of photogrammetry appeared, first of all analog and analytical and, in modern times, digital photogrammetry. The essence of photogrammetry is that the user receives a model of the object in one of the available formats based on photos of the object using photogrammetry software. Photogrammetry has found application in numerous fields: art, design, engineering. When two images of the same object taken at different angles are projected, a sense of depth is created, that is, the impression of a third dimension is created. The technical prerequisites for a successful photogrammetry process are the recording of high-quality photographs of the object. It is necessary to use a high-quality camera in order to obtain photos of high-quality resolution with depth of field. Objects with high reflectivity and objects without pronounced texture are not suitable for digitization by photogrammetry.

Paper [2] presents a case study where part of a car seat was digitized using photogrammetry and Photomodeler software. The cloud of points obtained by photogrammetry was compared with the CAD model and the largest measured difference of the cloud of points in relation to the model is about 2.2 mm, on the basis of which it was concluded that the photogrammetry method can satisfy the desired accuracy. A unique theoretical framework for the implementation of the photogrammetry process with physical and mathematical formulations is presented in the paper [5]. There are numerous examples of digitization of artistic statues and parts of larger dimensions [4]. Photogrammetry enables the measurement of extremely large structures such as radio telescopes [3]. Researchers are developing semi-automated systems to facilitate the use of photogrammetry for smaller parts [1]. The joint application of photogrammetry and additive manufacturing is shown in [6], a sculpture of an officer digitized by photogrammetry and then made by additive technology.

As presented, there are many examples of the application of photogrammetry, but it is primarily used for the digitization of artistic statues, objects or larger parts such as pieces of furniture. The goal of this paper is to analyze the perspective of the use of photogrammetry in the auto industry, that is, for the reverse engineering of auto components. In this paper, the analysis will be made through three sheet metal parts. The parts will be digitized in two ways, scanned with a 3D scanner Artec eva lite belonging to the middle price range and by photogrammetry using a mobile phone camera. The point cloud obtained by the 3D scanner will be taken as a reference and by overlaying it with the point cloud obtained by photogrammetry and deviation analysis, conclusions will be drawn.

1 DIGITALIZATION OF PARTS

The Artec eva lite scanner according to the manufacturer's specification has a precision of up to 0.1 mm and due to its proven precision this digitization result will be taken as a reference. Photogrammetry was done using a mobile phone camera and then post-processed with appropriate software. Three parts were selected: the crankcase after deep drawing with the rim, the finished crankcase and the wing of a vehicle. The layout of the parts is shown in Figure 1.

a) *b)* *c)*

Figure 1. Analyzed parts a) crankcase with rim b) crankcase c) the wing of a vehicle

1.1 Scanning parts with a 3D scanner

The parts were scanned and post-processed in Artec studio 13 software. They were exported from the software in stl format. The appearance of the point clouds is shown in Figure 2.

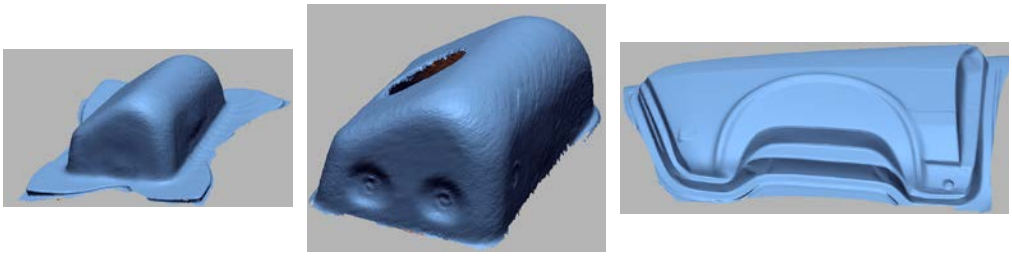

a) *b)* *c)*

Figure 2. Point clouds of parts scanned by a 3D scanner

1.2 Photogrammetry

Zephyr 3D software was used for photogrammetry. There are several versions of the software, and in this paper a trial version was used, which is available to students and researchers. According to the theory of photogrammetry, images were made from three levels. For the first two parts, 34 and 38 photos were taken, which is quite enough due to the size of the parts, while for the third part, 50 photos were taken, which is the limit for the free version of the software. All three parts are suitable for photogrammetry because they have a pronounced texture (measuring grids that already existed on the parts). If there was no texture on the parts, it would be necessary to apply certain shapes so that the software could more easily do the joining. In both cases, hand-drawn markers were used to make the process easier. Each part was photographed from three levels and care was taken to make the photos at approximately the same distances as to make each part visible in the three photos.

According to the theoretical basis of photogrammetry, that it is forbidden to crop, modify photos, all photos were imported into photogrammetry software, and after the initial checks, the initial calibration of the cameras was made.

The first result of photogrammetry is to obtain a certain number of points to determine if the reconstruction is well done. After that, the complete model is obtained, which includes the texture, as shown in Figure 3.

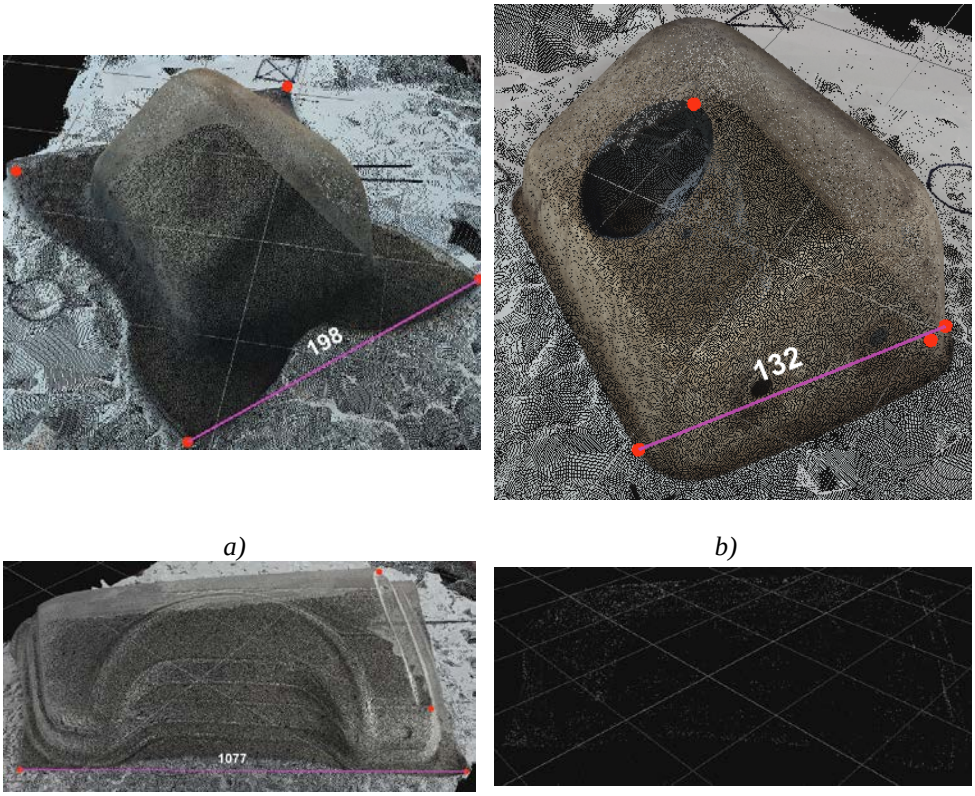

a) *b)*

c) *d)*

Figure 3. Obtained mesh of a) crankcase with rim b) finished crankcase c) the wing of a vehicle and d) point cloud of the vehicle wing

In Figure 3, where the results of photogrammetry are shown, certain control points can be seen. The result of photogrammetry is a cloud of points where the shape of the part is defined but the dimensions do not correspond to the actual dimensions. In order for the dimensions of the cloud of points obtained by photogrammetry to be accurate, it is necessary to calibrate the results. This is achieved by defining control points. It is necessary to find two points that are easy to mark on the mesh and that it is possible to measure the distance between those two points on the model that is the subject of digitization. The selection of these points and accurate measurement are a challenge because any measurement error leads to a difference in the results. After calibration, the point cloud is exported in stl format. Given that as a result of photogrammetry, the environment is also obtained, it is necessary to process the obtained stl in the software. Autodesk meshmixer, which is free and available to researchers, was used in this research.

2 ANALYSIS OF RESULTS

The analysis of the results of the photogrammetry process will actually be a comparison of two point clouds where the stl obtained by a 3D scanner will be selected as a reference. Overlapping two point clouds can be done in numerous software such as Geomagic control, Cloud control, Gom inspect, etc. Gom inspect software was used in this research. It is necessary to first overlap two models by defining one stl as cad body and the other as mesh. The layout of the superimposed stl files and deviations is given in Figure 4.

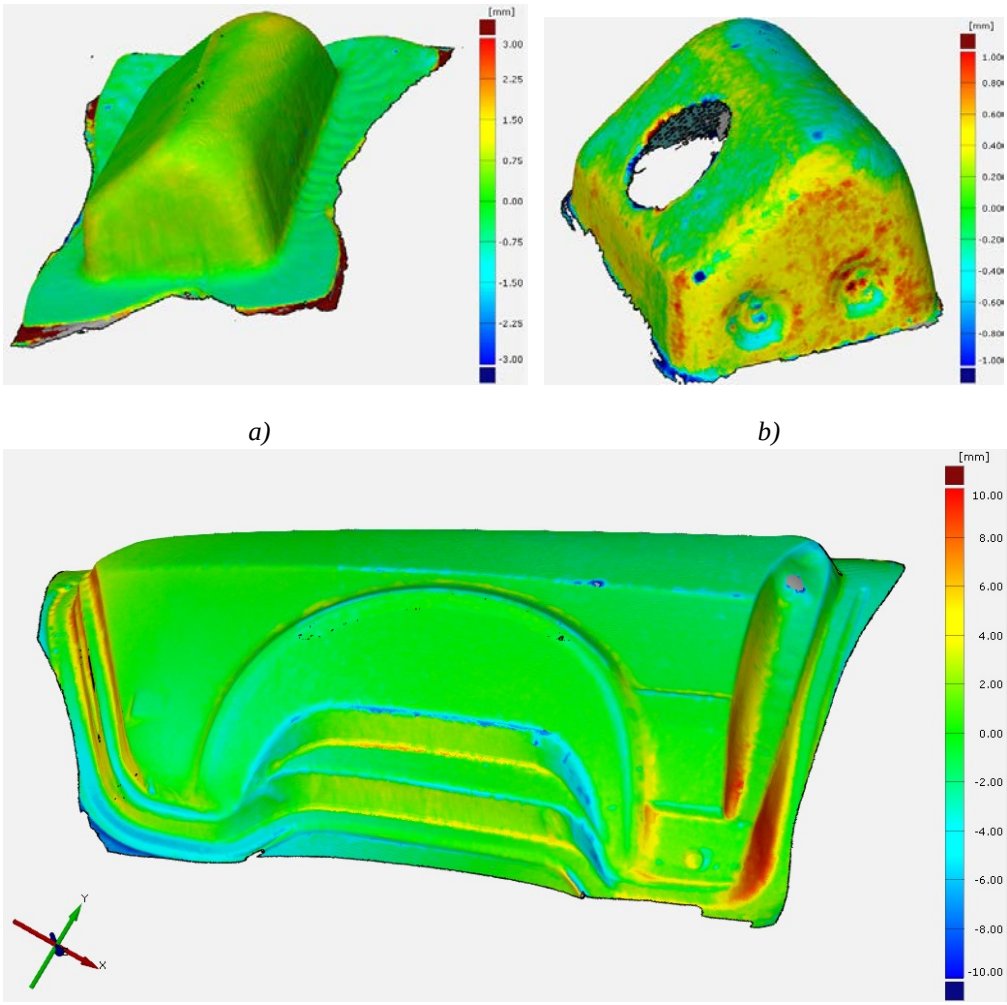

a) *b)*

c)

Figure 4. Deviation between obtained point clouds for a) the crankcase with rim b) the final crankcase and c) the vehicle wing

The deviations shown in Figure 4 are satisfactory. Deviations on the smaller parts shown in Figure 4 a and b are less than 1 mm. Deviations in the largest part are significantly larger and the highest value is around 8 mm, while in the rest of the part the deviation is less than 2 mm, on average around 1.8 mm. The explanation for such a large deviation is an error in

calibrating the accuracy of the cloud of points, that is, in measuring the physical model and matching that measurement with the control points.

3 CONCLUSIONS

The analysis of the results showed that the application of photogrammetry has a perspective for application in the auto industry. Given that the deviations are significant, the conclusion is that photogrammetry at this moment cannot be used to control the accuracy of parts, but that the point cloud or the resulting model can be a good basis for reverse engineering or the reconstruction of parts.

ACKNOWLEDGMENTS

The present work was funded by the Ministry of Science and Technological Development of the Republic of Serbia under the project TR34002.

REFERENCES

[1] Collins, T., Woolley, S. I., Gehlken, E., Ch'ng, E.: "Automated low-cost photogrammetric acquisition of 3D models from small form-factor artefacts", Electronics, Vol. 8, No. 12, 2019, 1441.

[2] Gerbino, S., Martorelli, M., Renno, F., Speranza, D.: "Cheap photogrammetry versus expensive reverse engineering techniques in 3d model acquisition and shape reconstruction", In DS 32: Proceedings of DESIGN 2004, the 8th International Design Conference, Dubrovnik, Croatia, 2004, 749-754.

[3] Kesteven, M.: "Photogrammetry for large structures", [Online] https://www.gb.nrao.edu/MetConf/talks/Wednesday/Kesteven.pdf, 2016.

[4] Prasetyo, Y., Yuwono, B. D., Barus, B. R.: "Comparative Analysis of Accuracy to the Establishment of Three Dimensional Models from Diponegoro Prince Statue Using Close Range Photogrammetry Method in Non Metric Camera and Unmanned Aerial Vehicle (UAV) Technology", In IOP Conference Series: Earth and Environmental Science, Vol. 313, No.1, 2019, 012038.

[5] Shan, J., Hu, Z., Tao, P., Wang, L., Zhang, S., Ji, S.: "Toward a unified theoretical framework for photogrammetry", Geo-spatial Information Science, Vol. 23, No. 1, 2020, 75-86.

[6] Zivanović, S., Tabaković, S., Randjelović, S.: "Rapid prototyping of art sculptural shapes according to the sample", Advanced Technologies and Materials, Vol. 44, No. 1, 2019, 27-32.

Intentionally blank

MOBILITY & VEHICLE MECHANICS

https://doi.org/10.24874/mvm.2025.51.03.05
UDC: 656.1.08:004.414.23

ROAD TRAFFIC ACCIDENTS PREDICTION USING MACHINE LEARNING METHODS

Vesna Ranković[1], Andrija Đonić[2], Tijana Geroski[3]*

Received in August 2024 *Accepted in October 2024*

RESEARCH ARTICLE

ABSTRACT: Road traffic accidents are identified as a significant societal issue based on extensive and comprehensive research in public health and traffic safety. Such incidents lead to significant negative outcomes, including human casualties, economic consequences, vehicle damage, and significant medical costs. Developing predictive models is crucial for identifying risk factors associated with accidents, thereby improving understanding of accident causes and enabling more effective prevention interventions. The occurrence of traffic accidents is influenced by a multitude of factors, including driver behavior, vehicle characteristics, weather conditions, road volume, road geometry, type of road, road conditions, speed limits, frequency of police controls, etc. In this paper, machine learning (ML) techniques are used to develop the traffic accident prediction model due to the non-linear relationship between input and output variables. The research investigates the influence of certain input variables on the number of traffic accidents, as their optimal choice significantly affects the prediction performance. The random forest, support vector machine, and neural networks are employed for data preprocessing and model development. Statistical indicators are used to evaluate the performance of the developed models. Based on the obtained performances, the developed ML models accurately predict the number of traffic accidents.

KEY WORDS: *road safety, road accident, prediction, machine learning, feature*

[1]*Vesna Ranković, Faculty of Engineering, University of Kragujevac, Sestre Janjić 6, Kragujevac, Serbia, vesnar@kg.ac.rs, https://orcid.org/0009-0004-0172-3216, (*Corresponding author)*
[2] *Andrija Đonić, Department of Informatics and Quantitative Methods, Faculty of Economics, University of Kragujevac, Liceja Knezevine Srbije 3, 34000 Kragujevac, Serbia, andrija.djonic@ef.kg.ac.rs, https://orcid.org/0000-0003-1624-3536*
[3] *Tijana Geroski, Faculty of Engineering, University of Kragujevac, Sestre Janjić 6, Kragujevac, Serbia, tijanas@kg.ac.rs https://orcid.org/0000-0003-3459-3011*

PREDVIĐANJE SAOBRAĆAJNIH NEZGODA KORIŠĆENJEM METODA MAŠINSKOG UČENJA

REZIME: Saobraćajne nezgode su identifikovane kao značajan društveni problem na osnovu opsežnih i sveobuhvatnih istraživanja u oblasti javnog zdravlja i bezbednosti saobraćaja. Takvi incidenti dovode do značajnih negativnih ishoda, uključujući ljudske žrtve, ekonomske posledice, oštećenja vozila i značajne medicinske troškove. Razvoj prediktivnih modela je ključan za identifikaciju faktora rizika povezanih sa nezgodama, čime se poboljšava razumevanje uzroka nezgoda i omogućavaju efikasnije preventivne intervencije. Na pojavu saobraćajnih nezgoda utiče mnoštvo faktora, uključujući ponašanje vozača, karakteristike vozila, vremenske uslove, obim puta, geometriju puta, vrstu puta, uslove na putu, ograničenja brzine, učestalost policijskih kontrola itd. U ovom radu, tehnike mašinskog učenja (MU) se koriste za razvoj modela predviđanja saobraćajnih nezgoda zbog nelinearnog odnosa između ulaznih i izlaznih varijabli. Istraživanje istražuje uticaj određenih ulaznih varijabli na broj saobraćajnih nezgoda, jer njihov optimalan izbor značajno utiče na performanse predviđanja. Za prethodnu obradu podataka i razvoj modela koriste se slučajna šuma, mašina vektora podrške i neuronske mreže. Statistički indikatori se koriste za procenu performansi razvijenih modela. Na osnovu dobijenih performansi, razvijeni MU modeli tačno predviđaju broj saobraćajnih nezgoda.

KLJUČNE REČI: *bezbednost u saobraćaju, saobraćajna nezgoda, predviđanje, mašinsko učenje, funkcija*

ROAD TRAFFIC ACCIDENTS PREDICTION USING MACHINE LEARNING METHODS

Vesna Ranković, Andrija Đonić , Tijana Geroski

INTRODUCTION

Road traffic accidents constitute a serious global issue with significant impacts on human lives and national economies. According to the World Health Organization's Global Road Safety Report 2023 [20], the number of road traffic deaths in 2021 of 1.19 million worldwide represents a 5 % decrease compared to the number of deaths recorded in 2010. Besides the loss of human lives, traffic accidents also impose significant economic consequences. In 2019, the total socio-economic costs of traffic accidents in the Republic of Serbia amounted to 8.8 % of the gross national product [12]. Countries around the world have revised their road safety policies and strategies while incorporating new technologies to mitigate road accidents and their consequences. These efforts are aimed at enhancing traffic safety and reducing the severity of accidents [6].

Data-driven road safety models are crucial for evaluating the effectiveness of applied safety measures and policies, enabling their continuous improvement in order to reduce the number of traffic accidents. In the literature, various techniques for predicting, classifying, and analyzing traffic accidents have been proposed [9]. The factors influencing the number of traffic accidents are numerous and complex. They include technical aspects of roads and vehicles, vehicle speed, traffic density, as well as human factors such as driver behavior, level of concentration and fatigue, and weather conditions [2].

Models based on classical statistical methods, such as the Poisson regression model and negative binomial regression model, have limitations in predicting the number of traffic accidents due to the complex non-linear relationships between input and output variables [11].

To overcome the limitations of traditional statistical methods, various machine learning and deep learning techniques have been applied to traffic safety analysis [5]. These techniques are suitable for modeling flexibility, ability to learn and generalize from data, and high predictive accuracy. Consequently, machine learning models are considered robust and accurate tools in traffic safety research. Artificial intelligence techniques enable the discovery of patterns and relationships in traffic data that were previously difficult to detect using conventional methods. Ali et al.[3] conducted a comprehensive review of machine learning-based models designed to predict different aspects of traffic accidents. The models encompass predicting crash occurrences, forecasting crash frequencies, and estimating the severity of injuries resulting from crashes. Analysis indicates that a significant amount of research has focused on machine learning-based models for predicting injury severity.Almamlook et al. [4] developed a model to binary classify the severity of traffic accidents using various machine learning methods, including AdaBoost, logistic regression, naive Bayes, and random forests.

Gorzelanczyk [10] employed neural network time series prediction using a multilayer perceptron to forecast the number of road accidents. Raja et al. [16] utilized different recurrent and feedforward neural network architectures for classifying severity levels in accidents (slight, serious, and fatal) and used the long short-term memory (LSTM) model for time series forecasting of the number of accidents. The dataset includes various attributes such as personal details, specifics of the accidents, environmental factors, vehicle

information, and road characteristics. Singh et al. [19] used a multilayer perceptron with four hidden layers for predicting road accident frequencies on highways. The sixteen input variables belonging to road geometry, traffic, and road environment were considered as potential inputs to the model. García de Soto [7] developed two neural networks with one hidden layer each to predict the number of accidents with light injuries, severe injuries and fatalities, on open roads and in tunnels. The models utilized continuous input variables such as annual average daily traffic, percentage of heavy traffic, average curve radius, mean positive slope, mean negative slope, longitudinal evenness rating, and surface adhesion rating, as well as categorical variables like posted speed limit and the number of lanes per direction.

This paper utilizes machine learning models to accurately predict the number of road accidents. The performance of feedforward neural networks, support vector machines, and random forest is compared, due to the fact that these models have been shown as the most appropriate in similar problems. The proposed models are applied to selected sections of IB order roads in the Republic of Serbia. Ten features are considered, and the feature importance values are calculated using the RF classifier.

1 METHODOLOGY

Feedforward neural network, support vector machine and random forest are supervised learning algorithms that require a labeled training dataset. The training dataset consists of *m* samples $\left\{\left(\boldsymbol{x}^{(k)}, y_k\right)\right\}_{k=1}^{m}$, where $\boldsymbol{x}^{(k)} \in \mathbb{R}^n$ represents the input variables of the *k*th element of the training data set and $y_k \in \mathbb{R}$ denotes the corresponding target output.

1.1 Feedforward neural network

In this paper, a multi-layer perceptron with one hidden layer was used. The output of the neural network with n inputs, one output, and one hidden layer with *Z* neurons is computed as follows:

$$y_{FNN} = \sum_{j=1}^{Z} \omega_{1,j(2)} f\left(\sum_{i=1}^{n} \omega_{j,i(1)} x_i + b_{j(1)}\right) + b_{1(2)} \tag{1}$$

where: y is the output of the neural network, $\omega_{1,j(2)}$ denotes is the weight from the jth hidden neuron to the output, f is the activation function in the hidden layer, $\omega_{j,i(1)}$ denotes he weight from the ith input to the jth hidden neuron, x_i is the ith input, $b_{j(1)}$ is the bias for the jth hidden neuron, $b_{1(2)}$ is the bias for the output neuron.

The performance of a neural network with a single hidden layer depends on the hyperparameters, which should be carefully chosen. Hyperparameters are the number of hidden neurons that determines the complexity and capacity of the layer, the type of the activation function of these neurons, the algorithm used for training as well as the parameters of the selected algorithm. Optimization strategies for the FNN involve the use of both conventional and metaheuristic approaches [13].

Support vector regression

Support Vector Regression (SVR) is a type of SVM used for regression tasks. Unlike traditional regression methods, SVR aims to find a function that approximates the data within a specified margin of tolerance (ε), while maximizing the margin between parallel hyperplanes [18].

$$y_{SVR} = \sum_{i=1}^{nSVR} \left(\alpha_i - \alpha_i^*\right) K\left(\boldsymbol{x}_i, \boldsymbol{x}\right) + b \tag{2}$$

where: $nSVR$ is the number of support vectors, α_i and α_i^* denote the Lagrange multipliers, $K\left(\boldsymbol{x}_i, \boldsymbol{x}\right)$ is the kernel function that measures the similarity between the support vector $\boldsymbol{x}_i$ and the new sample $\boldsymbol{x}$, b is the bias.

In Support Vector Regression (SVR), various types of kernel functions are employed to establish the relationship between input features and target variables. These include:

Linear kernel:

$$K\left(\boldsymbol{x}_i, \boldsymbol{x}\right) = \boldsymbol{x}_i^T \boldsymbol{x} \tag{3}$$

Polynomial kernel:,

$$K\left(\boldsymbol{x}_i, \boldsymbol{x}\right) = \left(\boldsymbol{x}_i^T \boldsymbol{x} + r\right)^d \tag{4}$$

Radial Basis Function (RBF) kernel:

$$K\left(\boldsymbol{x}_i, \boldsymbol{x}\right) = \exp\left(\frac{-\left\|\boldsymbol{x} - \boldsymbol{x}_i\right\|}{2\sigma^2}\right) \tag{5}$$

where: r , d and σ represent the parameter of the kernel function.

The choice of kernel function (linear, polynomial, RBF) and its parameters significantly influences the model's ability to capture non-linear relationships and its overall predictive performance. Additionally, fine-tuning the regularization parameter C and the tolerance parameter ε is essential for optimizing the trade-off between model accuracy and its generalization capabilities [1].

1.2 Random forest

Random Forest (RF) is a robust machine learning algorithm that utilizes multiple decision trees to predict outcomes. Each tree in the forest is trained on a random subset of the training data and features. This ensemble technique effectively reduces overfitting by averaging predictions across diverse trees, thereby enhancing accuracy and capturing complex relationships between input variables and the target output. In regression tasks, the Random Forest model computes its prediction by averaging the outputs of all individual trees in the forest.

The overall output of the random forest model for input $\boldsymbol{x}$ is computed by averaging the predictions from all trees:

$$y_{RF}\left(\boldsymbol{x}\right) = \frac{1}{N_t} \sum_{i=1}^{N_y} y_{RF_i}\left(\boldsymbol{x}\right) \tag{6}$$

where: N_t denotes the total number of trees in the random forest ensemble, $y_{RF_i}(\boldsymbol{x})$ represents the prediction of the ith tree for the input $\boldsymbol{x}$.

The RF model's hyperparameters include the number of candidate variables randomly selected for each split, the sample size determining how many observations are randomly sampled for each tree, whether the sampling is done with or without replacement, the minimum number of observations required in a terminal node, the minimum number of observations required to split a node, the total number of trees in the ensemble, and the criterion used for splitting nodes [15]. These parameters collectively influence the RF model's performance and its ability to generalize effectively to new data.

2 RESULTS AND DISCUSSION

The paper discusses part of the roads of the IB order in the Republic of Serbia. The set contains data on 113 sections of roads 22, 23, 33, 34 and 39, Figure 1. Data on section length, annual average daily traffic volume and the number of traffic accidents are extracted from the Public enterprise roads of Serbia [14] and Road traffic safety agency (Republic of Serbia) [17]. Data on terrain type, curvature, lane width are taken from [8].

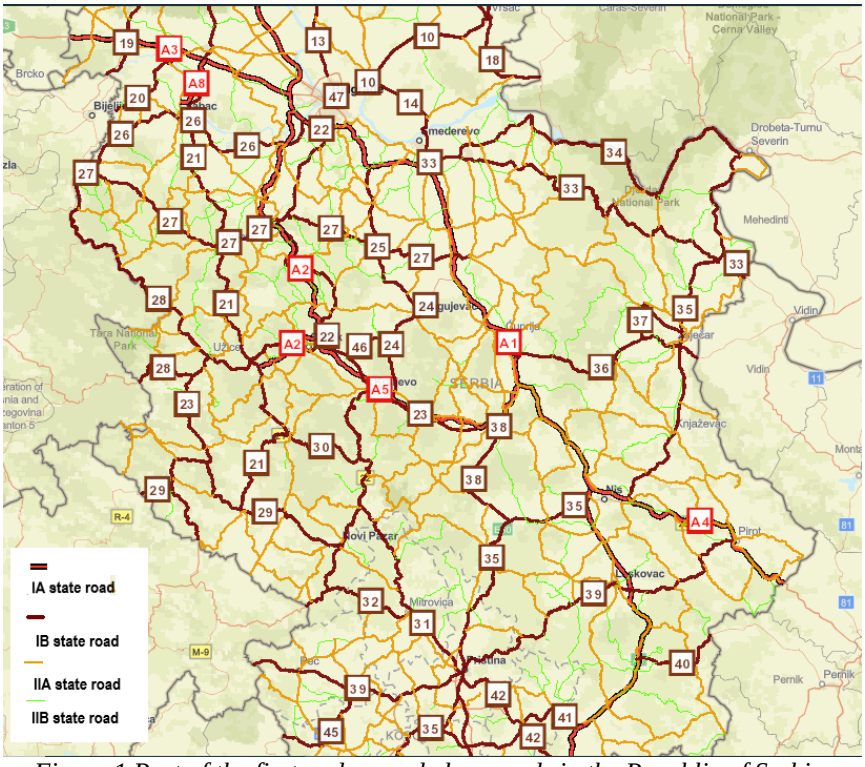

Figure 1 Part of the first and second class roads in the Republic of Serbia.

Section Length (km) - SL, the Annual average daily traffic volume - AADT (veh/day), and the number of traffic accidents are continuous variables, while Terrain type - TT (type 1-level, type 2-rolling, type 3-mountainous), Curvature (curve 1-minimal, curve 2-severe, curve 3-serpentine), and Lane width (5–6 m, >6 m) are categorical variables.The summary statistics of continuous variables are shown in Table 1.

Table 1 The summary statistics of continuous variables

	SL (m)	AADT (veh/day)	TA
Mean	8791.59	6464.72	9.97
SD	7799.58	4970.31	11.81
Min	200	244	0
Max	46900	25581	70
Var	6.08 x 107	2.47 x 107	139.44

As part of data preprocessing, the initial set is prepared and optimized for algorithm performance. Scaling of the numerical attributes (Section Length, Annual Average Daily Traffic Volume, and the number of traffic accidents) to a range of 0 to 1 is performed to achieve greater numerical stability, faster data processing, and increased model stability. Regarding categorical variables (Terrain Type, Curvature, and Lane Width), one-hot encoding is applied, which separates these variables into individual inputs based on their values. This results in obtaining 10 input attributes and one output. Outlier detection is also applied using the Isolation Forest method, which leads to noise reduction in the data and improved model performance. Six instances classified as outliers are detected and removed from the dataset, reducing the final set to 107 instances or rows in the table.

The prediction performances of the machine learning models are calculated using the correlation coefficient (r), the mean absolute error (MAE) and the root mean square error (RMSE):

$$\mathrm{r} = \frac{\sum_{k=1}^{N_s}\left(y_{pk}-\bar{y}_p\right)\left(y_k-\bar{y}\right)}{\sqrt{\sum_{k=1}^{N_s}\left(y_{pk}-\bar{y}_p\right)^2\sum_{k=1}^{N_s}\left(y_k-\bar{y}\right)^2}} \tag{7}$$

$$\mathrm{MAE} = \frac{1}{N_s}\sum_{k=1}^{N_s}\left|y_{pk}(k)-y_k\right| \tag{8}$$

$$\mathrm{RMSE} = \frac{1}{N_s}\sqrt{\sum_{k=1}^{N_s}\left(y_{pk}-y_k\right)^2} \tag{9}$$

where y_{pk} and y_k denote the model output and the measured value respectively; $\bar{y}_p$ and $\bar{y}$ denote their average respectively, and N_s represents the number of observations in the data set.

The forecasting models have been implemented in Python.

A neural network with ten inputs is configured with a single hidden layer where the number of neurons is varied. After evaluating the model's performance with unipolar and bipolar sigmoid activation functions in the hidden layer, the best results are achieved with 16 neurons using the Rectified Linear Unit (ReLU) activation function. The network is trained using the Adam (Adaptive Moment Estimation) optimizer with mean squared error as the loss function over 100 epochs, with a batch size of 8, to predict the number of traffic accidents.

The SVR model achieved the best performance with the RBF kernel ($\sigma = 0.1$), regularization parameter C set to 100, and tolerance parameter ε set to 0.01, determined through the grid search methodology

The parameters of the random forest model are configured as follows: the number of candidate variables randomly selected for each split **(**max_features**)** is set to 'auto'; the sample size determining how many observations are randomly sampled for each tree **(**max_samples**)** is set to None; whether the sampling is done with or without replacement **(**bootstrap**)**is set to True; the minimum number of observations required in a terminal node **(**min_samples_leaf**)** is set to 1 and the criterion used for splitting nodes **(**criterion**)** is set to 'mse'. Through the application of the grid search method, the total number of trees in the ensemble (n_estimators) and the minimum number of observations required to split a node (min_samples_split) were adjusted to 150 and 4, respectively.

Table 2 presents the performance of the trained models and the hyperparameters adjusted for model optimization. Metric results are separately shown for the training and test sets.

Table 2 Performance parameters of the models and hyperparameters

Model	Data set	R	RMSE	MAE	Hyperparameters
Random forest	Training	**0.94**	**4.25**	**2.53**	n_estimators = 150, min_samples_split = 4
	Test	**0.87**	**4.63**	3.62	
SVM	Training	0.82	7.18	4.01	kernel='rbf', $C = 100$, $\varepsilon = 0.01$, $\sigma = 0.1$
	Test	0.79	5.65	3.96	
Neural netork	Training	0.85	6.35	3.98	optimizer='adam', loss='mean_squared_error', epochs=100, batch_size=8, number of neurons in the hidden layer=16, activation function of the hidden neurons: ReLU
	Test	0.84	4.83	**3.52**	

Based on the results from Table 2, it can be concluded that the best predictions for traffic accident frequency were achieved using the Random Forest (RF) algorithm.

Given that the Random Forest model achieved the best results among the three trained in this study, it is taken as representative and used to show the impact of input attributes on the output.

In this paper, the built-in Gini importance method is used to evaluate feature importance, known for its simplicity and efficiency in assessing the contribution of each feature in the model. After training the model, the importance of the features is extracted using the feature_importances_ attribute, which is part of the trained Random Forest model. The importance of the features is sorted in a created DataFrame in descending order and then visualized in a horizontal bar chart shown in Figure 2.

Figure 2 illustrates that both section length and annual average daily traffic volume exert the greatest influence on the frequency of traffic accidents. Following these factors, terrain type emerges as a significant parameter, particularly type 2 (rolling) and type 3 (mountainous). Additionally, the curvature attributes, particularly curve 2 (severe), curve 3 (serpentine), and curve 1 (minimal), also contribute significantly to accident frequency. At the very end is the

Lane width attribute, with 5–6 m followed by >6 m, between which TT type 1-level is positioned.

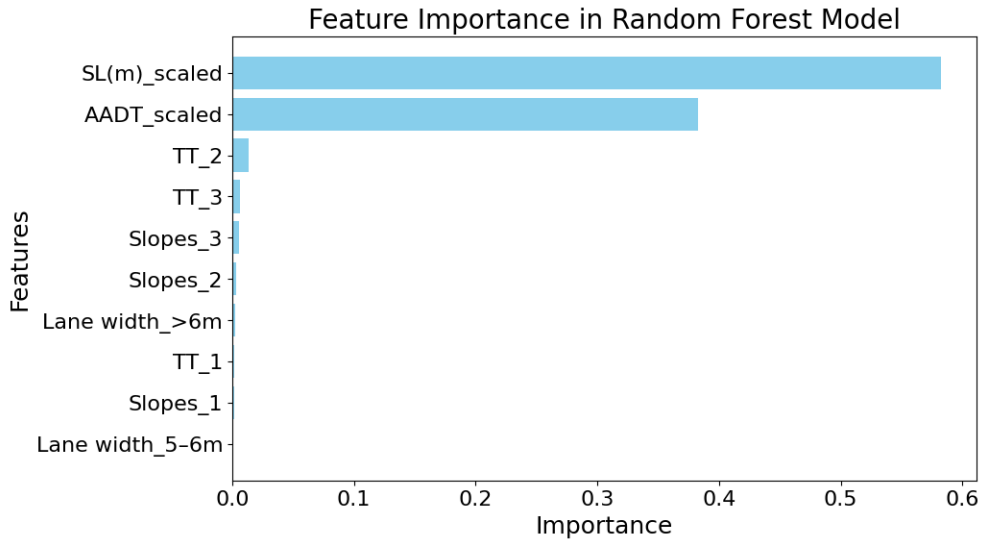

Figure 2 Feature importance in Random Forest Model

3 CONCLUSIONS

This study confirm the effectiveness of machine learning methods, especially support vector machines, neural networks and random forests, in predicting traffic accident occurrences. Evaluation of these models using established statistical metrics consistently demonstrates the superior predictive performance of random forest. For the training set, R, MAE, and RMSE are 0.94, 2.53, and 4.25 respectively, while for the test set, these values are 0.87, 3.62, and 4.63. Furthermore, the use of random forest for feature importance analysis provided detailed insight into the significant predictors affecting accident frequency.

These models are crucial for optimizing traffic management strategies by enabling precise prediction of risks and potential accidents on roads. Their application allows targeted allocation of safety resources, including more efficient deployment of police, emergency services, and other resources at locations where the likelihood of accidents is higher. Additionally, these models facilitate planning of preventive measures such as road improvements, additional signage, changes in traffic organization, or speed adjustments in specific road sections, all aimed at reducing accidents and enhancing the safety of all road users. Furthermore, they can significantly aid in the design and planning of future road infrastructure, ensuring safer and more effective road networks.

ACKNOWLEDGMENTS

This research was supported by the Ministry of Science, Technological Development and Innovation of the Republic of Serbia, contract number 451-03-65/2024-03/200107 (Faculty of Engineering, University of Kragujevac).

REFERENCES

[1] Açıkkar, M., Altunkol, Y.: "A novel hybrid PSO- and GS-based hyperparameter optimization algorithm for support vector regression", Neural Computing and Applications, Vol. 35, 2023, 19961–19977.

[2] Ahmed, S., Hossain, M.A., Ray, S.K., Bhuiyan, M.M.I., Sabuj, S.R.: "A study on road accident prediction and contributing factors using explainable machine learning models: analysis and performance", Transportation Research Interdisciplinary Perspectives, Vol.19, 2023, 100814.

[3] Ali, Y., Hussain, F., Haque, M.M.: "Advances, challenges, and future research needs in machine learning-based crash prediction models: A systematic review", Accident Analysis & Prevention, Vol. 194, 2024, 107378.

[4] AlMamlook, R.E., Kwayu, K.M., Alkasisbeh, M.R., Frefer, A.A.: "Comparison of Machine Learning Algorithms for Predicting Traffic Accident Severity", 2019 IEEE Jordan International Joint Conference on Electrical Engineering and Information Technology (JEEIT), Amman, Jordan, 2019, 272–276.

[5] Dong, C., Shao, C., Li, J., Xiong, Z.," An Improved Deep Learning Model for Traffic Crash Prediction", Journal of Advanced Transportation, Vol. 2018, Article ID 3869106, 2018, 13 pages.

[6] Fisa, R., Musukuma, M., Sampa, M., Musonda, P., Young, T.: "Effects of interventions for preventing road traffic crashes: an overview of systematic reviews", BMC Public Health, Vol. 22, 2022,1–18.

[7] García de Soto, B., Bumbacher, A., Deublein, M., Adey, B.T.: "Predicting road traffic accidents using artificial neural network models", Infrastructure Asset Management, Vol.5, No.4, 2018, 132–144.

[8] Gatarić D, Ruškić N, Aleksić B, Đurić T, Pezo L, Lončar B, Pezo M. "Predicting Road Traffic Accidents—Artificial Neural Network Approach. Algorithms", Vol 16. No. 5, 2023, 257.

[9] Gutierrez-Osorio, C., Pedraza, C.: "Modern data sources and techniques for analysis and forecast of road accidents: A review", Journal of Traffic and Transportation Engineering (English Edition), Vol. 7, No. 4, 2020, 432–446.

[10] Gorzelanczyk, P.: "Application of neural networks to forecast the number of road accidents in provinces in Poland", Heliyon, Vol. 9, No.1, 2023, e12767.

[11] Lord, D., Mannering, F.: "The statistical analysis of crash-frequency data: A review and assessment of methodological alternatives", Transportation Research Part A: Policy and Practice, Vol. 44, No. 5, 2010, Pages 291–305.

[12] Official Gazette: "Strategy for Traffic Safety of the Republic of Serbia for the Period 2023-2030 with the Action Plan for the Period 2023-2025" Official Gazette No. 84/2023, Belgrade. (In Serbian)

[13] Ojha, V.K., Abraham, A., Snášel, V.: "Metaheuristic design of feedforward neural networks: A review of two decades of research", Engineering Applications of Artificial Intelligence, Vol. 60, 2017, 97–116.

[14] P.E. Roads of Serbia. Traffic Counting. Available online: https://www.putevi-srbije.rs/index.php/en/traffic-counting (accessed on 20 June 2024).

[15] Probst, P, Wright, M.N, Boulesteix, A-L.: "Hyperparameters and tuning strategies for random forest", WIREs Data Mining and Knowledge Discovery, Vol. 9, No. 3, 2019, e1301.

[16] Raja, K., Kaliyaperumal, K., Velmurugan, L., Thanappan, S.: "Forecasting road traffic accident using deep artificial neural network approach in case of Oromia Special Zone", Soft Computing, Vol. 27, 2023, 16179–16199.

[17] Road Traffic Safety Agency of the Republic of Serbia. Integrated Database of Traffic Safety Features. 2022. Available online: http://195.222.99.60/ibbsPublic/ (accessed on 20 June 2024).

[18] Sánchez, A.V.D.: " Advanced support vector machines and kernel methods", Neurocomputing, Vol. 55, No. 1–2, 2003, 5–20.

[19] Singh, G., Pal, M., Yadav, Y., Singla T.: "Deep neural network-based predictive modeling of road accidents", Neural Computing and Applications, Vol. 32, 2020, 12417–12426.

[20] World Health Organization: "Global status report on road safety 2023", 2023.

MVM – International Journal for Vehicle Mechanics, Engines and Transportation Systems

NOTIFICATION TO AUTHORS

The Journal MVM publishes original papers which have not been previously published in other journals. This is responsibility of the author. The authors agree that the copyright for their article is transferred to the publisher when the article is accepted for publication.

The language of the Journal is English.

Journal ***Mobility & Vehicles Mechanics*** is at the SSCI list.

All submitted manuscripts will be reviewed. Entire correspondence will be performed with the first-named author.

Authors will be notified of acceptance of their manuscripts, if their manuscripts are adopted.

INSTRUCTIONS TO AUTHORS AS REGARDS THE TECHNICAL ARRANGEMENTS OF MANUSCRIPTS:

Abstract is a separate Word document, "*First author family name_ABSTRACT.doc*". Native authors should write the abstract in both languages (Serbian and English). The abstracts of foreign authors will be translated in Serbian.

This document should include the following: 1) author's name, affiliation and title, the first named author's address and e-mail – for correspondence, 2) working title of the paper, 3) abstract containing no more then 100 words, 4) abstract containing no more than 5 key words.

The manuscript is the separate file, „*First author family name_Paper.doc*" which includes appendices and figures involved within the text. At the end of the paper, a reference list and eventual acknowledgements should be given. References to published literature should be quoted in the text brackets and grouped together at the end of the paper in numerical order.

Paper size: Max 16 pages of B5 format, excluding abstract
Text processor: Microsoft Word
Margins: left/right: mirror margin, inside: 2.5 cm, outside: 2 cm, top: 2.5 cm, bottom: 2 cm
Font: Times New Roman, 10 pt
Paper title: Uppercase, bold, 11 pt
Chapter title: Uppercase, bold, 10 pt
Subchapter title: Lowercase, bold, 10 pt
Table and chart width: max 125 mm
Figure and table title: Figure _ (Table _): Times New Roman, italic 10 pt

Manuscript submission: application should be sent to the following e-mail:

mvm@kg.ac.rs ; lukicj@kg.ac.rs
or posted to address of the Journal:
University of Kragujevac – Faculty of Engineering
International Journal M V M
Sestre Janjić 6, 34000 Kragujevac, Serbia

The Journal editorial board will send to the first-named author a copy of the Journal offprint.

MVM – International Journal for Vehicle Mechanics, Engines and Transportation Systems

OBAVEŠTENJE AUTORIMA

Časopis MVM objavljuje orginalne radove koji nisu prethodno objavljivani u drugim časopisima, što je odgovornost autora. Za rad koji je prihvaćen za štampu, prava umnožavanja pripadaju izdavaču.

Časopis se izdaje na engleskom jeziku.

Časopis ***Mobility & Vehicles Mechanics*** se nalazi na SSCI listi.

Svi prispeli radovi se recenziraju. Sva komunikacija se obavlja sa prvim autorom.

UPUTSTVO AUTORIMA ZA TEHNIČKU PRIPREMU RADOVA

Rezime je poseban Word dokument, "*First author family name_ABSTRACT.doc*". Za domaće autore je dvojezičan (srpski i engleski). Inostranim autorima rezime se prevodi na srpski jezik. Ovaj dokument treba da sadrži: 1) ime autora, zanimanje i zvanje, adresu prvog autora preko koje se obavlja sva potrebna korespondencija; 2) naslov rada; 3) kratak sažetak, do 100 reči, 4) do 5 ključnih reči.

Rad je poseban fajl, „*First author family name_Paper.doc*" koji sadrži priloge i slike uključene u tekst. Na kraju rada nalazi se spisak literature i eventualno zahvalnost. Numeraciju korišćenih referenci treba navesti u srednjim zagradama i grupisati ih na kraju rada po rastućem redosledu.

Dužina rada: Najviše 16 stranica B5 formata, ne uključujući rezime
Tekst procesor: Microsoft Word
Margine: levo/desno: mirror margine; unurašnja: 2.5 cm; spoljna: 2 cm, gore: 2.5 cm, dole: 2 cm
Font: Times New Roman, 10 pt
Naslov rada: Velika slova, bold, 11 pt
Naslov poglavlja: Velika slova, bold, 10 pt
Naslov potpoglavlja: Mala slova, bold, 10 pt
Širina tabela,dijagrama: max 125 mm
Nazivi slika, tabela: Figure __ (Table _): Times New Roman, italic 10 pt

Dostavljanje rada elektronski na E-mail: **mvm@kg.ac.rs ; lukicj@kg.ac.rs**

ili poštom na adresu Časopisa
Redakcija časopisa M V M
Fakultet inženjerskih nauka
Sestre Janjić 6, 34000 Kragujevac, Srbija

Po objavljivanju rada, Redakcija časopisa šalje prvom autoru jedan primerak časopisa.

MVM *Editorial Board*
University of Kragujevac
Faculty of Engineering
Sestre Janjić 6, 34000 Kragujevac, Serbia
Tel.: +381/34/335990; Fax: + 381/34/333192
www.mvm.fink.rs